

UNIVERSITY OF OKLAHOMA  
GRADUATE COLLEGE

BREAKING THE PRACTICAL PERFORMANCE BARRIERS OF  
POLARIMETRIC PHASED ARRAY WEATHER RADARS

A DISSERTATION  
SUBMITTED TO THE GRADUATE FACULTY  
in partial fulfillment of the requirements for the  
Degree of  
DOCTOR OF PHILOSOPHY

By  
CESAR M. SALAZAR AQUINO  
Norman, Oklahoma  
2022

BREAKING THE PRACTICAL PERFORMANCE BARRIERS OF  
POLARIMETRIC PHASED ARRAY WEATHER RADARS

A DISSERTATION APPROVED FOR THE  
SCHOOL OF ELECTRICAL AND COMPUTER ENGINEERING

BY THE COMMITTEE CONSISTING OF

Dr. Robert D. Palmer, Co-Chair

Dr. Boonleng Cheong, Co-chair

Dr. Nikola Petrov

Dr. Mark Yeary

Dr. Tian-You Yu

Dr. David Schwartzman



*Dedicated to my lovely wife, Ana Rodriguez, my beloved family, Elva Valenzuela,  
Carla Aquino, and Manuel Salazar, and in memory of Cesar Aquino*

## **Acknowledgments**

First and foremost, I want to express my gratitude to god. He has set this path for me, and I thank him for every day he gave me. It is through his hand that I have achieved this goal.

I express my most sincere gratitude to my advisers and mentors, Dr. Robert D. Palmer and Dr. Boonleng Cheong. Their academic support has been invaluable to me. Thanks to them, the signal processing techniques, discussed in this document, have positively impacted the weather radar community. Their expertise in weather radar and signal processing has been foundational during my career, and I have learned how to be a good researcher from each meeting we shared. They have lit my research curiosity and guided me to achieve every goal we have set. I am incredibly thankful to them, and I hope I can count on them in my future research path. You have been a positive inspiration for me, and I hope you can keep inspiring future generations of students and researchers.

Moreover, their support for me has extended beyond the academic scope. The Ph.D. has been a bumpy road, with difficulties, challenges, and frustrations, but gladly I have had great advisers who helped and guided me in every step of the road. They were always willing to help me when I asked them about anything, professional or personal. Finally, I want to thank them for the time invested in reviewing this dissertation and for all suggestions made.

I want to extend my gratitude to Dr. David Schwartzman. From the moment he

joined our research group, his positive energy and academic advice have positively impacted me and my research. Thanks for the encouragement, guidance, and technical suggestions. Your contributions have strengthened the techniques proposed in this dissertation, and we are happy to have you on our team. I wish you the best in your academic path as a professor. Keep inspiring future generations.

Thanks to my graduate committee Dr. Mark Yeary, Dr. Tian-You Yu, Dr. David Schwartzman, and Dr. Nikola Petrov. Thanks for your time and help in this process. Thanks for your willingness and support in all the meetings we have had. Thanks for your encouragement, continuous feedback on this work, and contributions to it.

Thanks to the Advanced Radar Research Center, represented by all faculty and staff that works there. You are by far the best place to work. I learned a lot from the professors and their expertise, and I enjoyed the conversations we shared during my time there. Thanks to the staff and engineers for always being willing to help everyone. Every one of you is what makes the Advanced Radar Research Center what it is today, and thanks to you, it will get better every day.

Thanks to my friends and colleagues working at the Advanced Radar Research Center, especially Jorge Luis Alva Alarcon, Nim Ccoillo Ramos, Hyeri Kim, Yoon Kim, Nawaf Almuqati, Precious Jatau, Reece Reinke, Tony Segales, Min-Duan Tzeng, Rosalind Agasti, Sergio Rodriguez, Mariel Avalos, Felipe Moncada, Alexis Oblitas, and Majood Haddad. Thanks for the uncountable coffee cups we share, the endless talks, the going-outs, and the game sessions. It has been such a fantastic experience to share time with you guys. Keep doing your best, and keep that friendly spirit.

This section would not be complete without expressing my gratitude to my lovely wife, Ana Catherine Rodriguez Salazar. You are my heart and soul. Everything I have accomplished is thanks to you and your endless support, time, and patience. Thanks for your encouragement and for smiling at me whenever things look wrong. Thanks

for celebrating all my achievements as yours and for not stopping believing. More importantly, thanks for being my wife. Thanks to my family, especially my role models, Elva Valenzuela, Carla Aquino, and Manuel Salazar. Thanks for being there at every moment. Thanks for lending me your ears when I needed someone to listen to me. Thanks for being there in my success and my failing. Thanks for your patience. And more importantly, thanks for raising me to be the man I am now.

Funding was provided by NOAA/Office of Oceanic and Atmospheric Research under NOAA-University of Oklahoma Cooperative Agreement #NA21OAR4320204, U.S. Department of Commerce, and by the NOAA National Severe Storms Laboratory through Cooperative Agreement #NA15OAR4320115.

## Table of Contents

<b>Acknowledgments</b>	<b>v</b>
<b>Table of Contents</b>	<b>x</b>
<b>List of Figures</b>	<b>xx</b>
<b>Abstract</b>	<b>xxi</b>
<b>1 Introduction</b>	<b>1</b>
1.1 Background . . . . .	1
1.2 Previous Work and Motivation . . . . .	8
1.3 Contributions . . . . .	14
1.4 Outline . . . . .	15
<b>2 Weather Radar Signal Processing Fundamentals</b>	<b>18</b>
2.1 Radar Range Equation . . . . .	19
2.1.1 Radar Range Equation - Point Targets . . . . .	19
2.1.2 Radar Range Equation - Volume Scattering . . . . .	22
2.1.3 Radar Sensitivity . . . . .	25
2.2 Pulse Compression . . . . .	25
2.3 Phased Array Radar Fundamentals . . . . .	29
2.3.1 Array Analysis . . . . .	29
2.3.2 Array Geometry . . . . .	32
2.3.3 Phased Array Radar Scanning . . . . .	34



2.3.4	Grating Lobes and other Phased Array Radar Related Downsides	39
2.3.5	Cross-Polar Component and Contamination . . . . .	45
2.4	Summary and the Need for Technical Solutions . . . . .	50
<b>3</b>	<b>Progressive Pulse Compression</b>	<b>51</b>
3.1	Methodology . . . . .	51
3.1.1	Algorithm Description . . . . .	51
3.1.2	Leak-Through Elimination and Partial Decoding . . . . .	53
3.1.3	Calibration . . . . .	57
3.2	Advantages and Limitations of PPC . . . . .	58
3.2.1	Sensitivity Analysis . . . . .	58
3.2.2	Limitations of PPC . . . . .	61
3.3	Results . . . . .	66
3.3.1	Simulation Results . . . . .	67
3.3.2	Experimental Results . . . . .	69
3.4	Summary . . . . .	73
<b>4</b>	<b>Cross-Polar Canceler Technique</b>	<b>75</b>
4.1	Methodology . . . . .	75
4.1.1	Number and Location of Canceler Elements . . . . .	79
4.1.2	Calculation of the Scaling Factors . . . . .	85
4.2	Advantages and Limitations of XPC . . . . .	87
4.2.1	XPC Performance with Respect to the Steering Angle . . . . .	87
4.2.2	Limitations of XPC . . . . .	88
4.3	Results . . . . .	92
4.3.1	Approach 1 Results . . . . .	98
4.3.2	Approach 2 Results . . . . .	101
4.4	Summary . . . . .	104

<b>5</b>	<b>Further Challenges and Proposed Solutions for the PPC and XPC Techniques</b>	<b>106</b>
5.1	Mismatched Filter to Improve PPC - From PPC to PPC+ . . . . .	106
5.1.1	Methodology . . . . .	111
5.1.2	Sensitivity Analysis . . . . .	114
5.1.3	Advantages and Limitations of PPC+ . . . . .	116
5.1.4	Results . . . . .	121
5.2	Improvement on the XPC Technique Based on a Calibration Strategy . .	125
5.2.1	Methodology . . . . .	125
5.2.2	Results . . . . .	127
5.3	Summary . . . . .	133
<b>6</b>	<b>Epilogue</b>	<b>135</b>
6.1	Discussion and Conclusions . . . . .	135
6.2	Future Work . . . . .	140
	<b>References</b>	<b>143</b>
	<b>Appendix A Acronyms</b>	<b>157</b>

## List of Figures

1.1	NEXRAD network coverage in the Contiguous United States. . . . .	2
1.2	NEXRAD network coverage in Alaska, the insular areas of the United States, Korea, and Japan. . . . .	3
1.3	Frequency function of the TFM waveform, designed by Cheong et al. (top), and expected baseband IQ samples (middle). Ambiguity function of the long pulse, called W1, ambiguity function of the fill pulse, W2, cross-correlation of the long pulse and fill pulse, X (bottom). Extracted from Cheong <i>et al.</i> [44] . . . . .	9
1.4	Radar sensitivity plot. When TFM is applied, there is observable an abrupt change in sensitivity for TFM (blue line) between the blind and visible range of PX-1000 (approximately 10 dB). Lower sensitivity values are better. Figure sourced from Cheong <i>et al.</i> [44]. . . . .	10
1.5	The abrupt change in sensitivity observed in a plan position indicator (PPI) plot processed with TFM and collected on 2012-06-03 at 08:20 UTC. The black dashed lines enclose the blind range. Figure sourced from Cheong <i>et al.</i> [44]. . . . .	11
1.6	Array modified to reduce cross-polar contamination. The main elements are colored black (AF1) and the repurposed elements red (AF2). Repurposed elements transmit an amplitude-inverted waveform (multiplied by -1), in the perpendicular polarization. Figure sourced from Sánchez-Barberty <i>et al.</i> [51]. . . . .	13

2.1	The principle of pulse compression, from [1].(a) Envelope of the transmitted waveform, (b) Frequency of the transmitted waveform vs. time, (c) LFM waveform, and (d) theoretical output of pulse compression. . . . .	28
2.2	Visual representation of steering in a linear array. Array pointing broad-side (black arrow) but electronically steered $\theta_0$ degrees off the broad-side (blue arrow). . . . .	35
2.3	Diffraction effect observed on a 3x3 MPA. In the left plot, there is presented a schematic of the array. In the right plot, there are presented each of the $f_i(\theta, \phi)$ , illustrating the edge effects. Extracted from [80]. . . . .	44
3.1	Flow chart of the PPC technique. Key differences from the PPC include using a window function to zero out the leak-through from the transmission, partial decoding, and a new calibration factor to estimate the reflectivity inside the blind range. . . . .	52
3.2	The principle of partial decoding. The target inside the blind range becomes obscured by strong leak-through when processed using the conventional method. When the PPC is applied, the target can be correctly estimated, as shown on the right. . . . .	54
3.3	Illustration of the uncontaminated tail portion of a target inside the blind range. The tail portion is used for partial decoding in the PPC. $R_b$ is the blind range. The received signal of a target located at $R_t$ spans the range $R \in [R_t, R_t + R_p]$ . Additionally, $R_p = R_b$ . . . . .	55
3.4	Depiction of the zeroing-out process. Received samples are replaced with zeros if they are within the transmit cycle. A taper, which is a gradual transition from zero to one is applied for reducing sidelobes of the pulse compression. . . . .	55

3.5	Radar sensitivity of different systems. PPC provides a smooth transition in sensitivity between the blind and visible ranges. In addition, PPC provides better sensitivity values inside the blind range compared to the time-frequency multiplexed waveform technique and has comparable sensitivity values to radar systems using higher power transmitters.	60
3.6	Waveform used for PPC experiments. A non-linear frequency modulated waveform has been selected, designed and optimized for the PX-1000 [6, 38]. Only the long pulse is used since the PPC technique requires no fill pulse.	61
3.7	Similar to Figure 3.6 but for the designed linear frequency modulated waveform.	62
3.8	Various waveform behaviors of the PPC technique. The waveform ambiguity function at various ranges are shown in the top panel, where the loss of range resolution from closer targets is apparent. In addition, there is a range shift of the peaks. The middle and bottom panels show the shift of the peak and reduction of range resolution, respectively, as a function of range.	63
3.9	Similar to Figure 3.8 but from a 2.2-MHz LFM waveform.	64
3.10	Similar to the top panel of Figure 3.8 but with a larger range of y-axis, which represents gain. Besides the main lobe, the range sidelobe levels also vary depending on the target range.	65
3.11	Similar to Figure 3.10 but using a 2.2-MHz LFM waveform.	66
3.12	Simulation setup and results, transmitting the OFM waveform. In the middle plot are presented the simulation results from the LPC. Similar results are shown on the lower plot but from the PPC. The simulation demonstrates that when processed using the LPC, the targets inside the blind range are obscured by the leak-through. In contrast, the targets are visible when using the PPC.	67

3.13	Similar to Figure 3.12 but for the designed LFM waveform. . . . .	68
3.14	Products processed using TFM: a) SNR, c) $Z$ , e) $v_r$ . Products processed using PPC: b) SNR, d) $Z$ , f) $v_r$ . In these plots it is shown that radar sensitivity is higher inside the blind range on PPC and that the discontinuity in sensitivity has been eliminated. . . . .	70
3.15	Products processed using TFM: g) $Z_{DR}$ , i) $\Phi_{DP}$ , k) $\rho_{HV}$ . Products processed using PPC: h) $Z_{DR}$ , j) $\Phi_{DP}$ , l) $\rho_{HV}$ . The spatial continuity is carried through the polarimetric variables as well. . . . .	71
3.16	Estimated radar sensitivity using the TFM (top) and PPC (bottom) techniques from the dataset collected on September 14, 2014, 22:33:13 UTC. They are obtained by finding the minimum detectable reflectivity factor values from a collection of radials. . . . .	73
4.1	Illustration of the XPC concept in a $2 \times 2$ array transmitting in $H$ and $V$ polarizations. The copolar patterns are shown as red and blue solid lines. The cross-polar pattern of each element is illustrated as red and blue dashed lines. One canceler element is necessary to mitigate cross-polar contamination on that particular array. In the perpendicular polarization, the canceler element transmits an amplitude and phase scaled version of the original waveform (the complex scaling factors are defined as $a$ and $b$ ). The canceler waveform is transmitted opposite the cross-polar pattern (cyan and magenta solid lines). In addition, the canceler element produces some cross-polarization in the intended polarization(dashed cyan and magenta lines). . . . .	76
4.2	Angular mismatch effect of a simulated $8 \times 8$ array populated with crossed-dipole elements. The array is steered $-38^\circ$ in azimuth and $18^\circ$ in elevation. Nevertheless, the $H$ pattern points $-40^\circ$ in azimuth and $18^\circ$ in elevation, and $V$ $-38^\circ$ in azimuth and $18^\circ$ in elevation. This change in the beam position is termed angular mismatch. . . . .	89

4.3	Similar to Figure 4.2 but the array is steered to a different position (12° in azimuth and 8° in elevation). The angular mismatch effect is unnoticeable for an angular resolution of 2° in azimuth and elevation. . . . .	90
4.4	XPC was applied on a simulated 8×8 array populated with crossed-dipole elements. The array is steered -38° in azimuth and 18° in elevation. Seven elements have been repurposed as canceler elements. The scaling factors on those elements are $a = 0.92 + j0.40$ and $b = 0.67 - j0.29$ . The cross-polar isolation is improved from 14.24 dB in $H$ and 11.41 dB in $V$ to 48.42 dB in $H$ and 31.49 dB in $V$ . . . . .	91
4.5	XPC was applied on a simulated 8×8 array populated with crossed-dipole elements. The array is steered 12° in azimuth and 8° in elevation. One element have been repurposed as canceler elements. The scaling factors on this element are $a = 0.92 + j0.06$ and $b = 0.98 + j0.01$ . The cross-polar isolation is improved from 30.37 dB in $H$ and 30.3 dB in $V$ to 320 dB in $H$ and $V$ . . . . .	91
4.6	Evaluation of XPC under approach 1. The Array is pointing broadside. One element is repurposed as a canceler. The scaling factors on this element are $a = 0.01 + j0$ and $b = 0.01 - j0$ . The cross-polar isolation is improved from 50.1 dB in $H$ and 50.11 dB in $V$ to 50.83 dB in $H$ and 50.84 dB $V$ . . . . .	94
4.7	Evaluation of XPC under approach 2. The Array is pointing broadside. One element is repurposed as a canceler. The scaling factors on this element are $a = 0.11 + j0.01$ and $b = 0.09 - j0.01$ . The cross-polar isolation is improved from 50.1 dB in $H$ and 50.11 dB in $V$ to 75.88 dB in $H$ and $V$ . . . . .	95

4.8	Similar to Figure 4.6, but for the array steered $-20^\circ$ in azimuth and $4^\circ$ in elevation. One element is used as canceler. The scaling factors on this element are $a = 0.75 + j11$ and $b = 0.78 - j0.12$ . The cross-polar isolation is improved from 31.57 dB in $H$ and 31.36 dB in $V$ to 48.52 dB in $H$ and 48.31 dB in $V$ . . . . .	96
4.9	Similar to Figure 4.7, but for the array steered $-20^\circ$ in azimuth and $4^\circ$ in elevation. One element is used as canceler. The scaling factors on this element are $a = 0.90 + j0.14$ and $b = 0.75 - j0.12$ . The cross-polar isolation is improved from 31.57 dB in $H$ and 31.36 dB in $V$ to 57.53 dB in $H$ and 57.25 dB in $V$ . . . . .	96
4.10	Similar to Figure 4.8, but plotting the array pattern purity. The array pattern purity increases from 97.46% in $H$ and 97.4% in $V$ to 99.65% in $H$ and 99.7% in $V$ . . . . .	97
4.11	Similar to Figure 4.9, but plotting the array pattern purity. The array pattern purity increases from 97.46% in $H$ and 97.4% in $V$ to 99.94% in $H$ and 99.91% in $V$ . . . . .	98
4.12	The calculated number of canceler elements and scaling factor on each steering position (approach 1). The number of elements (top) varies between 1 and 10. The magnitude of the scaling factor (middle) oscillates between zero and one. Finally, the phase of the scaling factor (bottom) is approximately zero radians except for the angles where the angular mismatch is noticeable in the patterns. . . . .	99



4.13	XPC performance from approach 1, based on the cross-polar isolation. The top two panels correspond to the original cross-polar isolation (in dB). In the middle panels, the improved cross-polar isolation, after implementing XPC, is presented (in dB). Finally, in the bottom two panels, the extra cross-polar isolation from XPC compared to the original one, is presented (in dB). The figure is divided into two columns. The left column corresponds to the results for the $H$ polarization and the right for the $V$ polarization. . . . .	100
4.14	Similar to Figure 4.13, but for the array pattern purity (in %). . . . .	100
4.15	Loss in the copolar gain, as a function of steering angle, when XPC is implemented. The left panel corresponds to the loss in $H$ and the right to the one in $V$ . It is approximately proportional to the number of canceler elements. . . . .	101
4.16	Similar to Figure 4.12, but calculated under the approach 2. . . . .	102
4.17	Similar to Figure 4.13, but evaluated under the approach 2. . . . .	103
4.18	Similar to Figure 4.14, but evaluated under the approach 2. . . . .	103
4.19	Loss in the copolar gain, as a function of steering angle, when XPC is implemented (approach 2). The left panel corresponds to the loss in $H$ and the right to the one in $V$ . It is approximately proportional to the number of canceler elements. . . . .	104
5.1	PPI plots of different radar variables processed using PPC: a) $Z$ (top plot), b) $Z_{DR}$ , c) $\phi_{DP}$ , and d) $\rho_{HV}$ , from a snow event observed in the metropolitan area of Oklahoma City on February 03, 2022, 01:57:28 UTC at an elevation angle of $4^\circ$ . . . . .	107
5.2	RHI plots of different radar variables processed using PPC: $Z$ (top plot), SNR (middle plot), and LDR (bottom plot), from a storm event observed with the ATSR mode on May 23, 2022, 16:33:42 UTC. . . . .	108

5.3	QVP of $Z$ (left plot), $Z_{DR}$ (center plot), and $\rho_{HV}$ (right plot) generated from a PPI gathered from a snow event in the metropolitan area of Oklahoma City on February 03, 2022, 02:37:39 UTC ( $12^\circ$ in elevation).	109
5.4	PPI plots of different products processed using PPC: a) $Z$ (top plot), b) $Z_{DR}$ , c) $\phi_{DP}$ , and d) $\rho_{HV}$ , from a convective storm event observed on March 18, 2022, 00:33:44 UTC at an elevation angle of $2^\circ$ . . . . .	110
5.5	Depiction of the window used to generate the mismatched filter, at the range $R_t$ km ( $t_t$ $\mu$ s). . . . .	113
5.6	sensitivity profiles for different blind mitigation techniques implemented on PX-1000. Similar to Figure 3.5, the hypothetical sensitivity profile of the OFM waveform is included in the plot (black dashed line). Using a mismatched filter reduces the sensitivity of PPC+ compared to PPC inside the transmission range. Nonetheless, using PPC+ still provides significantly better sensitivity than TFM. . . . .	116
5.7	Ambiguity function using PPC+ and based on the OFM waveform at different range gates. Comparing the results from PPC+ to the ones from PPC (see Figure 3.10), it can be seen that the main lobe peak migration is lower in PPC+, and the shoulder effect is less prominent. The shoulder reduction is more pronounced at closer ranges. . . . .	117
5.8	Ambiguity functions for two range gates located 1 and 8 km from the radar (blue and red lines), using PPC (dashed lines) and PPC+ (solid lines). A noticeable reduction in the shoulder effect is observed in the PPC+ ambiguity functions. . . . .	118
5.9	Similar to Figure 5.8, but zoomed in to observe the main lobe peak locations. . . . .	119
5.10	The top and bottom panels show the range resolution and main lobe peak offset as a range function. Results from PPC+ are compared with similar ones processed using PPC (extracted from Figure 3.8) . . . . .	120

5.11	Simulation results when transmitting the OFM waveform. The top plot illustrates the ideal location and power of the simulated targets. In the middle panel, the simulation results from the PPC are presented. Similar results are shown on the lower plot but from the PPC+. The simulation demonstrates that when processed using PPC+, the shoulder contamination is significantly reduced compared to PPC. . . . .	122
5.12	Products processed using PPC: a) $Z$ , c) $Z_{DR}$ , e) $\Phi_{DP}$ , g) $\rho_{HV}$ . Products processed using PPC+: a) $Z$ , c) $Z_{DR}$ , e) $\Phi_{DP}$ , g) $\rho_{HV}$ . In the PPC+ plots, it is shown that the shoulder effect, observed in the PPC plots (before 5 km), has been greatly reduced. . . . .	123
5.13	Flowchart corresponding to the improved XPC technique. . . . .	126
5.14	Evaluation of the improved XPC. The Array is steered $-38^\circ$ in azimuth and $18^\circ$ in elevation. Eleven elements are repurposed as cancelers. The scaling factors on these element are $a = 0.41 + j52$ and $b = 0.19 - j0.27$ . The cross-polar isolation is improved from 14.13 dB in $H$ and 10.91 dB in $V$ , to 45.32 dB in $H$ and 43.44 dB $V$ . . . . .	128
5.15	XPC and improved XPC results compared when the array is steered $-38^\circ$ in azimuth and $18^\circ$ in elevation. The improved XPC provides an extra 11.17 dB in isolation in $V$ and 0.51 dB in $H$ . However, the loss in the copolar gain on the improved XPC is higher (0.97 dB in $H$ and 0.59 dB in $V$ ). . . . .	129
5.16	The calculated number of canceler elements and scaling factor on each steering position (approach 2), using the improved XPC technique. The number of elements (top) varies between 1 and 13. The magnitude of the scaling factor (middle) oscillates between zero and one. Finally, the phase of the scaling factor (bottom) is approximately zero radians except for the angles where calibration was necessary. . . . .	129

5.17	Improved XPC performance. The top two panels correspond to the original cross-polar isolation (in dB). In the middle panels, the improved cross-polar isolation is presented (in dB). Finally, in the bottom two panels, the extra cross-polar isolation (compared to the original one) is presented (in dB). The figure is divided into two columns. The left column corresponds to the results for the $H$ polarization and the right for the $V$ polarization. . . . .	130
5.18	Similar to Figure 5.17, but for the array pattern purity, derived in Section 4.3 (in %). . . . .	131
5.19	XPC (left panels) and improved XPC (right panels) performance based on the cross-polar isolation. The top two panels correspond to the original cross-polar isolation (in dB). In the middle panels, the improved cross-polar isolation, after implementing either XPC or its improved version, is presented (in dB). Finally, in the bottom two panels, it is presented the extra cross-polar isolation (in dB) from either XPC or its improved version (compared to the original one). . . . .	132
5.20	Loss in the copolar gain, as a function of steering angle, for the improved XPC. The left panel corresponds to the loss in $H$ and the right to the one in $V$ . It is approximately proportional to the number of canceler elements. . . . .	132

## **Abstract**

Phased array radars (PAR) are being proposed as an alternative to replacing the Next Generation Weather Radar (NEXRAD) network, which has been in service for more than 30 years, reaching the end of its life cycle. The PAR can improve the temporal resolution of weather coverage compared to reflector antennas (currently implemented on NEXRAD). Temporal resolution is crucial for severe weather detection and surveillance, especially rapid-evolving phenomena such as tornadoes and hail storms. An all-digital PAR design is presently being explored based on their performance and flexibility improvement. Nevertheless, even all-digital PARs are not free from limitations. This work proposes two signal processing solutions to mitigate two significant limitations observed in those radar systems, i.e., blind range resulted from pulse compression technique and cross-polar contamination inherent in the patch antenna implementation, which is currently the only viable solution to an all-digital PAR system. The mitigation techniques to these two limitations are called Progressive Pulse Compression and Cross-Polar Canceler, respectively.

The Progressive Pulse Compression (PPC) technique is proposed to mitigate the blind range problem observed in radars using a frequency modulated waveform and pulse compression. The blind range is caused by the strong leak-through coupled into the receive chain during the transmission cycle. The PPC technique is based on partial decoding. It uses a portion of the uncontaminated received signal in conjunction with pulse compression to estimate the target characteristics from the incomplete signal. The

technique does not require using a fill pulse or any hardware modifications. The PPC technique can be divided into three steps. First is to apply a smooth taper to discard all the contaminated samples in the received signal that corresponds to the transmission cycle. The second step is to perform pulse compression using the so called matched filter. Finally, the third step is to calculate and apply a calibration factor to compensate for the progressively changing return signal (affected by the tapering) to recover the proper reflectivity values. This technique is implemented on the PX-1000 radar. In the near future, PPC will be implemented on the Horus phased array radar system. The PX-1000 and Horus radar systems have been designed by the Advanced Radar Research Center (ARRC) at the University of Oklahoma (OU).

Nevertheless, PPC has some limitations caused by the different frequency content between the modified (tapered) return signal and the matched filter used for compression. This difference causes a shift in the mainlobe peak and an asymmetrical increase in the sidelobe levels producing a “shoulder” effect. This work proposes improving PPC by compressing the modified return signal with amplitude-modulated versions (range dependent) of the original matched filter. The improved PPC is termed PPC+ and is planned as a software update from PPC. The PPC+ has been tested using data from the PX-1000 and will be presented in this dissertation.

The Cross-Polar Canceler (XPC) technique is proposed to mitigate the cross-polar contamination observed on phased array radars. The cross-polar contamination is especially problematic when steering the beam away from the broadside. It is defined as a leakage from the intended polarization observed in the perpendicular one. In the XPC technique, the elements on the array are divided into two groups: main elements and canceler elements. The main elements transmit without any modification. However, the canceler elements transmit a modulated version of the inverse (i.e., the mathematical negative) of the original waveform in the perpendicular polarization. After integration,

the field radiated by the canceler elements cancels the cross-polar contamination produced by the main ones. The XPC technique involves calculating the correct number of canceler elements, their location in the array, and the complex scaling factor that better mitigates the cross-polar contamination. This technique has been designed for polarimetric radars transmitting in simultaneous transmission and simultaneous reception of  $H/V$  polarization (STSR). The XPC technique will be implemented on the Horus radar system, currently under development.

For polarimetric radars, the difference in the element patterns on each polarization produces an angular mismatch between the peaks on the  $H$  and  $V$  array patterns. This angular mismatch affects the maximum performance achievable with the XPC. Calibration is included as part of XPC to mitigate this effect. Iterative calibration is necessary in the XPC technique. Additionally, calibration is performed before and after XPC is implemented on an operational PAR system. This enhanced version of XPC (including calibration) is termed improved XPC. Like the XPC, the improved XPC is intended to be implemented on the Horus radar system.

# Chapter 1

## Introduction

### 1.1 Background

Since the beginning of the 20<sup>th</sup> century, radar technology has proven to be an essential advancement in technology for the improvement of life in general. The first use of radar was for military applications, and was then extended to civilian applications (e.g., weather surveillance [1, 2]). Originally, radars were only able to detect targets and measure their ranges. Hence, the name radio detection and ranging (Radar). During World War II, coherent pulsed-Doppler radars were developed, which allowed the measurement of target velocity. This new capability was again extended to weather applications, which allowed modern weather radars to measure the radial component of the velocity vector of storms [2].

The use of radar in modern society is now ubiquitous, from weather surveillance to automobiles, airplanes, and other consumer products. Specifically for weather surveillance, the National Weather Service (NWS) operates and maintains a network of 160 high-resolution S-band Doppler radars, named Weather Surveillance Radar - 88 Doppler (WSR-88D). This network has been available since 1988 and is called the Next Generation weather radar (NEXRAD) [3, 4].

NEXRAD is a powerful tool for weather surveillance. It is used for storm and



severe weather detection. Therefore, it positively impacts the economy and life [5]. The NEXRAD network coverage is illustrated in Figures 1.1 and 1.2.

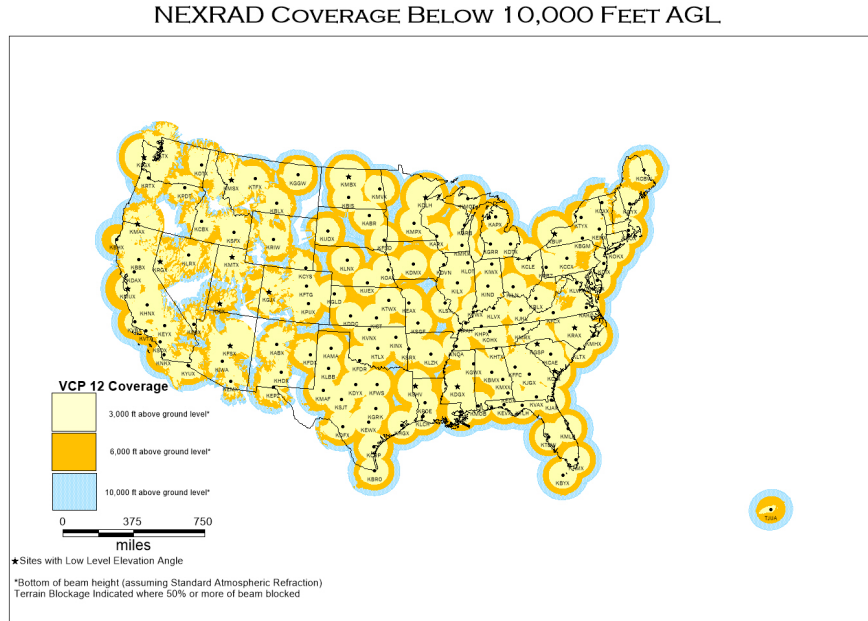


Figure 1.1: NEXRAD network coverage in the Contiguous United States, from the National Oceanic and Atmospheric Administration (NOAA) <sup>1</sup>.

WSR-88D has a reflector antenna mounted on a rotating pedestal [5]. The WSR-88D's transmitter is a master oscillator power amplifier [5], which uses a klystron-based amplifier, producing a peak power of 750 kW <sup>2</sup>. One limitation of this amplifier technology is the warm-up time that is required for the radar to be fully operational. Also, they are relatively expensive and large in size, affecting the overall maintenance cost and complexity of the system [6].

The original NEXRAD network was single-polarization, but was upgraded to dual-

<sup>1</sup>The previous images were sourced from the NOAA's website: <http://www.roc.noaa.gov/WSR88D/Maps.aspx>

<sup>2</sup>Source: NWS-NOAA, <https://training.weather.gov/wtdt/courses/rac/documentation/rac20-introduction.pdf>

polarization in 2012. That is, it is now capable of transmitting and receiving two orthogonal polarizations, i.e., horizontal ( $H$ ) and vertical ( $V$ ) [4, 7].

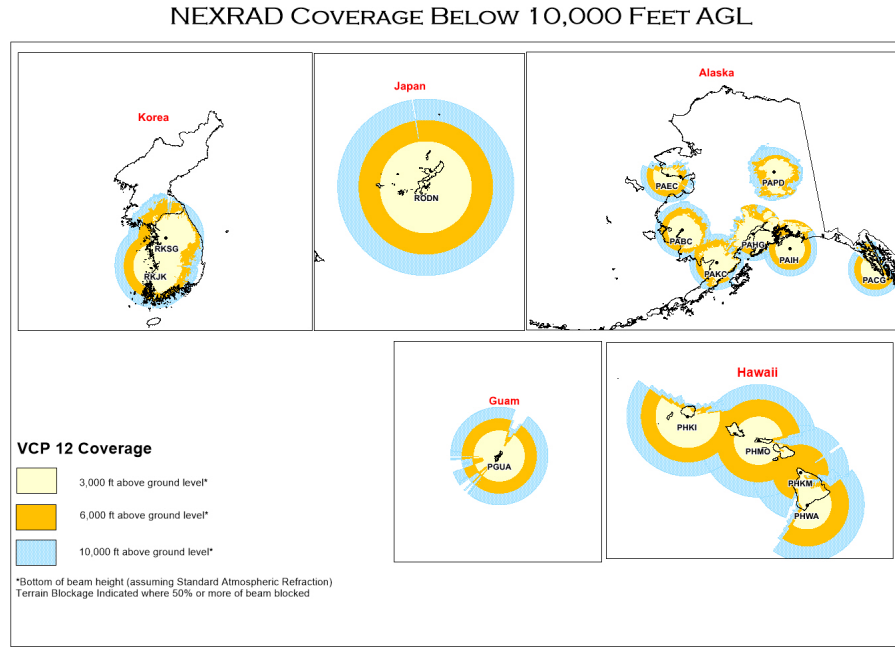


Figure 1.2: NEXRAD network coverage in Alaska, the insular areas of the United States, Korea, and Japan, from the National Oceanic and Atmospheric Administration (NOAA) <sup>3</sup>.

Today, polarimetric capabilities are essential in weather radar applications. Aside from the reflectivity ( $Z$ ), spectrum width ( $\sigma_v$ ) and the Doppler velocity ( $v_r$ ) of the targets, dual-polarization radars allow polarimetric variables to be measured. Some of these include differential reflectivity ( $Z_{DR}$ ), differential phase ( $\Phi_{DP}$ ), and cross-correlation coefficient ( $\rho_{HV}$ ). In addition to other applications, the use of polarimetric variables can help to understand the composition of a target storm. For example, a cell with high  $\rho_{HV}$  value (close to 1.0) indicates a homogeneous type of hydrometeors, i.e.,

<sup>3</sup>The previous images were sourced from the NOAA's website: <http://www.roc.noaa.gov/WSR88D/Maps.aspx>

pure rain or pure snow [2]. Another example, a high value of  $Z_{DR}$  indicates the presence of large drops (compressed in the vertical axis when falling) [8]. Lastly, another specific example, large values of  $Z_{DR}$  (positive and negative) and a low  $\rho_{HV}$  value can be representative of the presence of insects or birds [9].

WSR-88D has a number of volume coverage patterns (VCPs) for weather and atmosphere surveillance [5]. Three VCP examples are:

- Clear air, where it sweeps five elevation angles from  $0.5^\circ$  to  $4.5^\circ$  in roughly ten minutes <sup>4</sup>.
- Precipitation, where it sweeps, nine elevation angles, from  $0.5^\circ$  to  $19.5^\circ$  in six minutes <sup>5</sup>.
- Severe weather, where it sweeps, fourteen elevation angles, from  $0.5^\circ$  to  $19.5^\circ$  in five minutes.

Within a VCP, the radar completes an azimuthal scan ( $360^\circ$  rotation in azimuth) at a specific elevation angle, and then shifts to the next elevation. This process is repeated until all prescribed elevation angles are covered. Some VCPs contain two or three elevations that are scanned with two pulse repetition times (PRT). That is one complete scan is collected using a PRT, then a second can is collected at the same elevation using a different PRT. Such collection allows the use of a so-called velocity unfolding algorithm to improve the maximum observable Doppler velocity while simultaneously reducing the artifact of range folding [5, 10–13]. WSR-88D can theoretically scan faster. Its maximum rotational rate is  $30^\circ\text{s}^{-1}$  <sup>6</sup>. However, no VCP has been designed for such speeds [5].

---

<sup>4</sup>Source: NWS-NOAA, <https://www.weather.gov/iwx/wsr.88d>

<sup>5</sup>Source: NWS-NOAA, <https://www.weather.gov/iwx/wsr.88d>

<sup>6</sup>Source: NOAA's National Weather Service - Radar Operation center, <https://www.roc.noaa.gov/WSR88D/Engineering/NEXRADTechInfo.aspx>

The scan time of a radar is important for severe weather detection and surveillance. For example, the lifecycles of typical tornadoes are 2-4 minutes on average [14]. Unfortunately, the WSR-88D, under the severe weather mode, produces a limited number of temporal snapshots during such events. Nevertheless, better temporal coverage for the lower elevations is possible with alternative scanning methods [15, 16]. Phased array radars (PAR) have the potential to improve temporal resolution of weather coverage for such events [17–27].

A PAR antenna transmits and receives using an array of radiating elements. The antenna array is referred to as a phased array antenna. Each element in the array transmits a phase-shifted version of the same waveform, which causes constructive interference in the desired direction to form a beam. Based on this design, a PAR can electronically steer the electromagnetic beam to different positions rapidly (see Section 2.3.3). In addition, PAR systems are capable of producing various beam shapes, e.g., pencil beams, spoiled beams, fan beams, or even optimized beam patterns, designed specifically for the application [4, 27–31]. PAR also has the potential to reduce mechanical movement of the system and thus, increasing its lifetime and reducing operational costs.

As mentioned before, the Klystron transmitter of WSR-88D is operationally costly. There are various transmitter technologies that can help reduce the operational costs. One example is solid-state transmitters, which have high reliability, with a high mean time between failures, lower maintenance costs, and are smaller in size [6, 32]. Therefore, a solid-state PAR holds promise to be an alternative for a future weather radar network. Recently, all-digital PAR are being explored as the natural evolution for solid-state PAR with the potential for significant performance improvement and flexibility [26, 33, 34].

This notwithstanding, in the current state, all-digital PARs have some drawbacks that need to be addressed. Solid-state transmitters have low peak transmit power, on the

orders of only hundreds of watts [6]. The low peak power reduces the sensitivity of the radar (see Section 2.1.3), which is why pulse compression is almost always used with such transmitters (see Section 2.2). With pulse compression, the range resolution is directly proportional to the *effective* bandwidth of the waveform [1, 2, 35–39]. The long pulses used with pulse compression does cause an issue with so-called “blind range” since it is normally not possible to receive echoes while the pulse is being transmitted. On solid-state radar systems, blind range is a well-documented problem in the literature [38, 40–45]. In general, the blind range is a portion of the received data that is obscured due to the transmit leakage (i.e., the coupled transmit waveform to the receiver). The obscured portion, blind range  $R_b$ , can be several kilometers long, and it is directly proportional to the pulse width, as described by Equation (1.1) from Salazar *et al.* [39].

$$R_b = \frac{c\tau}{2}, \quad (1.1)$$

where  $c$  is the speed of light ( $\text{m s}^{-1}$ ) and  $\tau$  is the pulse width (s).

The pulse length, in meters  $R_p$  is also is directly proportional to the pulse width, and equal in length to  $R_b$  (see Equation (1.2)).

$$R_p = R_b = \frac{c\tau}{2} \quad (1.2)$$

As mentioned, when the radar is transmitting, it is usually not possible to receive useful data. There are exceptions in which the transmitted signal is intentionally sampled (through a separate channel) to measure peak power and instantaneous phase at the peak point, so-called “burst pulse.” Transmitter and receiver chains in radars are usually separated and isolated within the hardware using a switch or a circulator. However, hardware devices do not provide perfect isolation, and a high-power copy of the transmitted waveform can leak (couple) into the receiver, causing what is termed a leak-

through. This leak-through causes the blind range as the leak-through overpowers the received signals from the atmosphere. Thus, the radar is overwhelmed by the leaked energy, effectively saturating the receiver. Therefore, weather signals inside this region are obscured. As explained before, the blind range is a problem for solid-state radars because it can span tens of kilometers, limiting the quantity of useful data that the radar can provide [39]. If a PAR uses a solid-state transmitter and transmits long pulses, it will inhere the blind region problem.

Various solutions have been suggested to recover the data in the blind range. As proposed by Bharadwaj and Chandrasekar [43], one such option is by using multiple frequency bands and pulse lengths in which the pulses are transmitted successively. Another method uses a second pulse (fill pulse) that is time-frequency multiplexed with the long pulse, documented in Cheong *et al.* [44]. Finally, the use of multiple pulses separated in frequency and time has also been suggested, presented by George *et al.* [42].

Although the blind range issue can be mitigated, there are still a few limitations that must be addressed. One issue is the variable copolar bias and cross-polar contamination as a function of steering direction [46]. The copolar bias and the cross-polar contamination are intrinsic to all phased array and reflector antennas but they are almost negligible at broadside. The cross-polar contamination is defined as the leakage from the intended polarization (transmit and receive) into the other polarization [47]. A detailed definition will be provided in Section 2.3.5. The cross-polar contamination distorts the measurements in the intended polarization channel and thus, is undesirable. The copolar biases can be measured and removed digitally in post-processing [48]. However, the cross-polar contamination is more challenging to eliminate. It is also more severe in the simultaneous transmission simultaneous reception of  $H/V$  polarization (STSR) mode [49].

Due to their modular and flexible nature, all-digital PAR systems can be configured to reduce cross-polar contamination. Several implementations have been proposed in the literature, e.g., Díaz *et al.* [50] proposed a hardware solution based on an anti-symmetrical unit cell antenna design, with balance probe feeds for the  $H$  and  $V$  excitation. Others have proposed software solutions to mitigate the cross-polar contamination. For example, a set of transmit waveforms can be used to cancel contaminating signals [51–54].

## 1.2 Previous Work and Motivation

To mitigate the blind range challenge, several methods have been proposed using a fill pulse in addition to the long pulse for pulse compression [42–44]. The fill pulse is typically short, on the orders of a few microseconds, and at a different frequency. The new multiplexed pulse can include more than one fill pulse to meet the sensitivity requirements of the system. The time-frequency multiplexed waveform (TFM) method, for example, multiplexes two pulses, one long pulse, and a fill pulse [44]. On the other hand, George *et al.* [42], and Bharadwaj and Chandrasekar [43] proposed a method to multiplex multiple fill pulses to obtain a sensitivity curve with less abrupt discontinuities. Each fill pulse focuses on a different section of the blind range.

The receive signals are divided into sections where each is processed (match filtered) using the transmit waveform that is intended for that range. That is, the range of which the blind range echoes can be recovered. The differences in frequency between each multiplexed pulse is what allows the waveforms to be separated. Figure 1.3, shows a few properties about the TFM waveform proposed by Cheong *et al.* [44]. The top plot shows the frequency content of the waveform, the middle plot shows the time samples of the waveform, and the bottom plot shows the compressed waveform outside and in-

side the blind range, represented by the ambiguity function between the long and fill pulses.

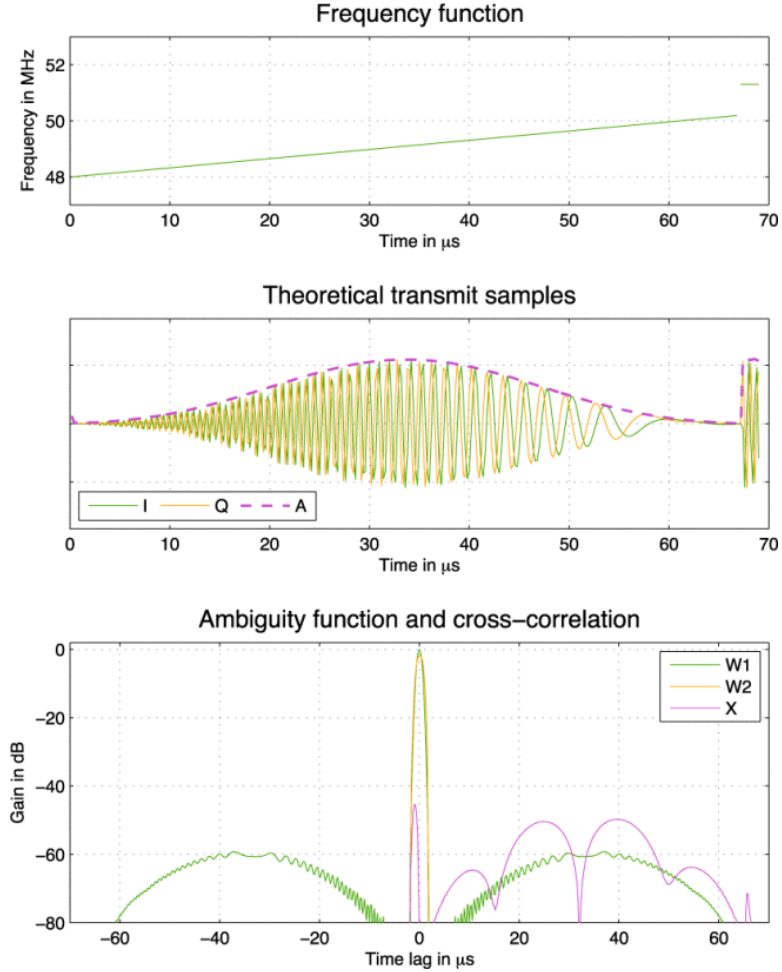


Figure 1.3: Frequency function of the TFM waveform, designed by Cheong *et al.* (top), and expected baseband IQ samples (middle). Ambiguity function of the long pulse, called W1, ambiguity function of the fill pulse, W2, cross-correlation of the long pulse and fill pulse, X (bottom). Extracted from Cheong *et al.* [44]

Nevertheless, the use of a fill pulse has some drawbacks. One of them is the additional bandwidth required to accommodate the fill pulse, assuming it uses a shifted frequency. Moreover, the fill pulses are shorter, resulting in lower average power and an abrupt change in radar sensitivity between the blind and visible ranges. This abrupt change in sensitivity can be observed in Figures 1.4 and 1.5 extracted from Cheong *et*



al. [44].

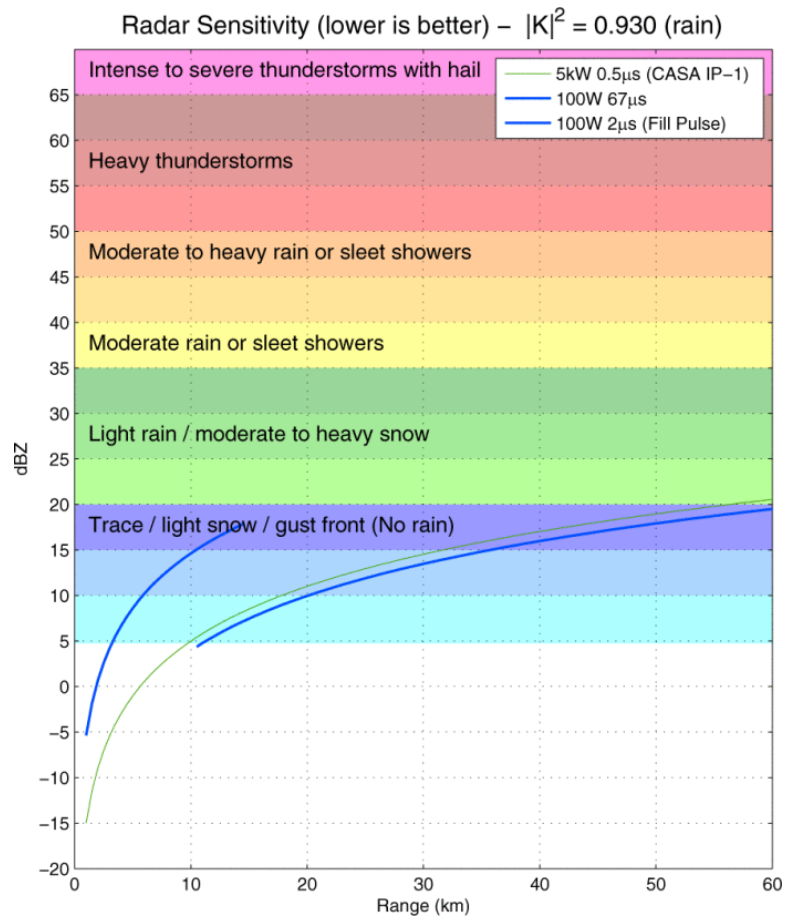


Figure 1.4: Radar sensitivity plot. When TFM is applied, there is observable an abrupt change in sensitivity for TFM (blue line) between the blind and visible range of PX-1000 (approximately 10 dB). Lower sensitivity values are better. Figure sourced from Cheong *et al.* [44].

Figure 1.4 shows the radar sensitivity of PX-1000 (a solid-state polarimetric X-band weather radar) when using the TFM. At the transition range, one can see the abrupt change in sensitivity to be approximately 10 dB. The sensitivity inside the blind range is sufficient to detect precipitation but not for drizzles.

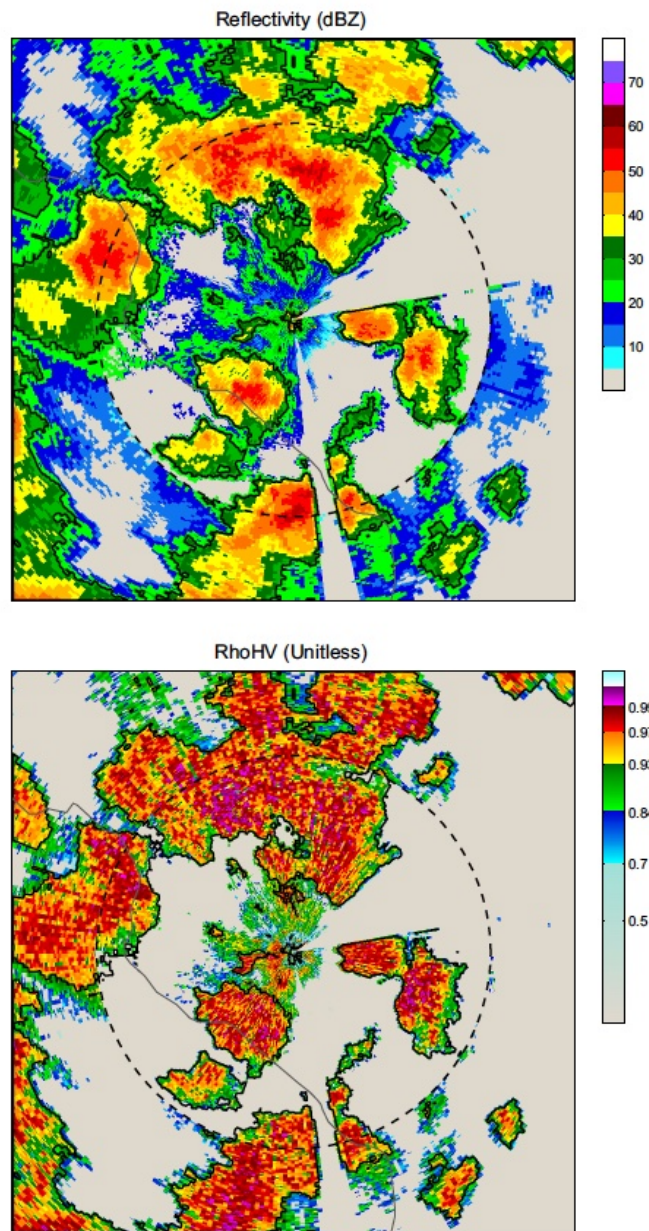


Figure 1.5: The abrupt change in sensitivity observed in a plan position indicator (PPI) plot processed with TFM and collected on 2012-06-03 at 08:20 UTC. The black dashed lines enclose the blind range. Figure sourced from Cheong *et al.* [44].

A new pulse compression technique is proposed in this dissertation based on partial decoding (see Chapter 3). This technique does not use fill pulses in contrast to the

previous solutions [42–44]. Therefore, no extra bandwidth is required, and there is no abrupt change in sensitivity between the blind and visible ranges. The proposed technique would make solid-state radar viable for meteorological applications.

Similar solutions (based on partial decoding) have been explored in the literature [55, 56]. However, they do not consider the leak-through contamination. Also, they do not propose solutions for the gain bias caused by partial decoding inside the blind range (see Chapter 3). In contrast, the technique proposed in this dissertation addresses these two important issues.

Concerning the cross-polar contamination, Díaz *et al.* [50] proposed a hardware solution for the multi-function phased array radar (MPAR) initiative. This solution was focused on a system with microstrip patch antennas (MPA). Therefore, hardware modifications are required to implement a similar solution in other systems. Signal processing solutions, in contrast, are software-based and can be easily implemented on various systems.

Several authors have proposed signal processing solutions for the cross-polar contamination problem. Sánchez-Barbetta *et al.* [51] repurposed a group of antennas (elements) in an array to transmit an amplitude-inverted waveform (multiplied by -1), in the perpendicular polarization. After spatial integration, the resulting cross-polar component in the steering angle (the location where the beam is pointing) will be lower. Figure 1.6, extracted from [51], illustrates the array with the main elements in black (AF1) and the repurposed elements in red (AF2).

The number of the necessary repurposed element is estimated as a function of the antenna cross-polar isolation and is usually not a round number. Thus, it needs to be rounded to the nearest integer. However, this rounding process limits the performance of the technique [49].

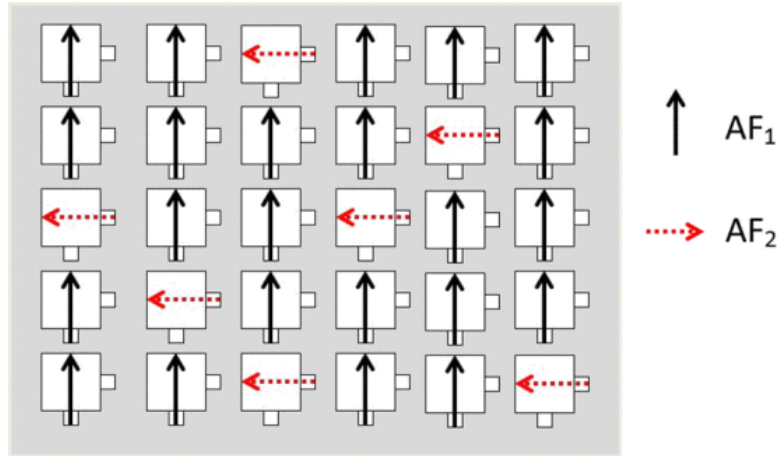


Figure 1.6: Array modified to reduce cross-polar contamination. The main elements are colored black (AF1) and the repurposed elements red (AF2). Repurposed elements transmit an amplitude-inverted waveform (multiplied by -1), in the perpendicular polarization. Figure sourced from Sánchez-Barberty *et al.* [51].

Yeary *et al.* [52] proposed a similar solution but defines the repurposed (auxiliary) elements as phase-adjusted elements. Different from Sánchez-Barberty *et al.* [51], Yeary *et al.* [52] pre-set the number of auxiliary elements. Then, the change in phase of those elements is calculated accordingly to the required cross-polar isolation value.

The implementations previously discussed significantly reduce cross-polar contamination. Nevertheless, neither of the two techniques expands the derivation to STSR mode. Two authors have proposed similar techniques for STSR [53, 54]. A commonality between the aforementioned techniques is the sparse location of the repurposed elements. In the author's opinion, the number of repurposed elements, their transmitting parameters, and their location impact the performance of the techniques.

This dissertation proposes a new technique capable of improving the cross-polar isolation for STSR mode. It optimizes the number of repurposed elements and their scaling factor to improve cross-polar isolation on the principal planes and throughout the scanning region.

In the author's opinion, the two techniques proposed are crucial for the success of

all-digital PAR as an important alternative for future weather radar networks.

### 1.3 Contributions

This dissertation proposes techniques to resolve two crucial inherent problems of solid-state PAR, the blind range and the cross-polar contamination. The proposed techniques improve on the limitations of the literature solutions discussed before. Also, the two techniques are implemented at a software level and are compatible with various systems using the same technology. The main contributions of this work are:

- A comprehensive analysis of the fundamentals of weather radar. It includes a literature review on the radar range equation, sensitivity, pulse compression, phased array antenna pattern calculation, cross-polar contamination, and other fundamental topics. This will be a good reference for future research on weather radar signal processing for all-digital PAR.
- A novel technique to mitigate the blind range without using extra fill pulses has been investigated. The Progressive Pulse Compression (PPC) technique provides better sensitivity inside the blind range. In addition, it eliminates the discontinuity in the sensitivity values between the blind and visible range. This technique does not require the use of fill pulses, or extra frequencies. In conclusion, less bandwidth is necessary. Bandwidth is an expensive resource, and reducing the bandwidth usage positively affects the system's projected costs. Alternatively, the extra bandwidth can be used for improving the performance of the long pulse.
- A signal processing technique capable of improving the cross-polar isolation of an all-digital PAR system has been studied. The Cross-Polar Canceler (XPC) technique is designed for dual-polarization systems and can be scaled to differ-

ent all-digital PAR systems and different array geometries. This technique can reduce cross-polar contamination at the broadside, on the principal planes, and in the entire scanning region. It is capable to calculate and implement the best solution to minimize the cross-polar contamination at each scanning location.

- Two innovative techniques that do not require hardware modifications to be implemented are proposed for future PAR systems. These techniques focus on all-digital PAR systems but can be implemented on various solid-state PAR systems. One of the proposed techniques, PPC, is already implemented as part of the signal processing for the PX-1000 radar system, which is built and operated by The Advanced Radar Research Center (ARRC) at The University of Oklahoma (OU) [44]. Live data from the PX-1000 can be obtained online <sup>7</sup>, and historical data can be obtained upon request.

## 1.4 Outline

In this dissertation, Chapter 2 covers the fundamentals of weather radar signal processing. It will provide the reader with a detailed definition of the pulse compression methodology, a review of the radar range equation, and the derivation of radar sensitivity. Also, it will cover the fundamentals of PAR and derive the calculations of the array factor, array pattern, and array steering. Additionally, this chapter will present a comprehensive discussion of cross-polar contamination of a PAR system.

Chapter 3 presents the PPC, a novel technique to mitigate the blind range challenge on radars that use pulse compression. This technique first eliminates the leak-through that causes the blind range and replaces it with zeroes; this does not eliminate the entirety of the echoes from obscured targets inside the blind range but only a portion of

---

<sup>7</sup>Source: ARRC - OU, <https://radarhub.arrc.ou.edu>

them. Since the uncompressed pulse is so long, even when the leak-through covers a part of it, a tail portion extends outside this blind range, and the return is uncontaminated. This tail portion is used to estimate the target signals within the blind range. Of course, because of the partial return, a proper calibration must be applied. PPC can be divided into three steps. The first step is to discard all the received signals during the transmit cycle and apply a smooth taper for the continuous transition from zero to one. The second step is to perform the pulse compression using a matched filter. Combining these two steps is equivalent to performing pulse compression using a progressively changing template to partially extract the uncontaminated received signal for compression. The third step is compensating for the progressively changing template so proper reflectivity values can be recovered. In Chapter 3, the methodology of PPC will be described in detail, including the derivation of the equations and simulation and experimental results based on data gathered from the PX-1000 radar.

Chapter 4 presents the XPC technique - a novel technique to improve cross-polar isolation for polarimetric PAR used for meteorological observations. It is based on “canceler” antenna elements transmitting a scaled version of the original waveform in the polarization where the cross-polar contamination is observed but with the opposite phase. The technique involves calculating the correct number of canceler elements, their location in the array, and a scaling factor for the amplitude and phase of the selected canceler elements to allow maximum cross-polar isolation. It is intended for dual-polarization, all digital, phased array radar systems. It can also be applied to sub-array architectures if amplitude and phase control is possible at the sub-array level. In Chapter 4, the methodology of XPC will be described in detail, and the equations to calculate all variables will be derived. Simulation results will be presented. Real results are pending since this technique is yet to be implemented as part of the Horus project currently in development by the ARRC at OU.

Chapter 5 revisits PPC and XPC by exploring the challenges related to these techniques and proposed solutions. PPC is implemented in the PX-1000 and has been used to collect data for over a year. In a group of these collected datasets, high sidelobes surrounding targets inside the blind range are observed. The high sidelobes create the illusion of a wider target in range, an “elongating” or “shoulder” effect. This issue has been compromising the overall quality of PPC. This dissertation proposes an improvement for PPC, capable of mitigating this issue. It is based on an amplitude modulation strategy that independently modifies the shape and taper of the compression filter at each range gate, mismatched filter, to reduce the sidelobe levels. In the first half of Chapter 5, the methodology behind this strategy and simulation results will be presented and discussed. The second half of Chapter 5 will focus on XPC. XPC’s polarimetric performance is critical for all-digital PAR, especially for weather applications. A new calibration strategy is proposed as part of the XPC technique to fulfill the weather performance requirements. The second part of Chapter 5 will describe the calibration strategy. Additionally, simulation results will be presented and discussed.

Chapter 6 summarizes all findings, contributions, and challenges from the techniques proposed in the previous chapters. It provides recommendations for the readers and the scientific community interested in these techniques. Finally, it suggests some future research paths that should be explored.



## Chapter 2

### Weather Radar Signal Processing Fundamentals

In Chapter 1, radar systems in general have been described. The most recognizable component of a radar system is the antenna, capable of transmitting and receiving an electromagnetic wave. Nonetheless, the radar system has more components that allow transmission and reception of radio waves and the processing of the received data. In addition to the hardware components of a radar, signal processing techniques [57, 58] are an essential part of the radar chain.

The tasks based on signal processing include calculating the received power of a radar system, the waveform modulation design, and the sensitivity calculation for a radar. On pulse-Doppler radar systems, radar signal processing is used to calculate the range and velocity of the target (point target or volume scattering) and the polarimetric variables. On radars using solid-state transmitters, radar signal processing is used for the matched filter implementation and pulse compression. On phased array radars, they are used for digital beamforming and use of various scan strategies. In addition, radar signal processing is important for the post-processing of radar data, such as noise reduction, ground clutter filtering, and mitigation of range and velocity ambiguities.[1, 2, 12, 59–64].

This chapter discusses different concepts related to radar signal processing. The first concept reviewed in this chapter is the radar range equation.

## 2.1 Radar Range Equation

The radar range equation is a fundamental equation in radar engineering. This important equation relates the received power to the characteristics of the transmitted radar signal, the observed range, and the parameters of the radar system itself. It includes the target's characteristics, attenuation caused by the environment, and other factors for evaluating the performance of the radar system [1, 2, 64]. The derivation of the radar range equation is presented in this section for both the point target and from volume scattering (“weather”) cases [1, 2, 64].

### 2.1.1 Radar Range Equation - Point Targets

For the radar range equation derivation, it is necessary to understand the complete path traveled by an electromagnetic wave from the moment the system transmits it to the moment it is received back at the system. In transmission, the radar generates an electromagnetic wave with a specific peak power ( $P_t$ ), in Watts, emitted by the antenna. This power is radiated isotropically, covering an imaginary sphere centered at the transmit antenna. Assuming the power is not attenuated by the medium, the power density ( $S_t(R)$ ), in  $\text{W m}^{-2}$ , at a range  $R$  from the radar, in meters, is equal to the  $P_t$  divided by the surface area of a sphere of radius  $R$ , in meters, see Equation (2.1)

$$S_t(R) = \frac{P_t}{4\pi R^2}. \quad (2.1)$$

In order to increase the directivity of a radar, a radar antenna does not transmit isotropically. Radar systems use directive antennas or digital beamforming (in phased array systems) to direct  $P_t$  to a specific location. Then, for a radar antenna, the power density radiated to a particular location is much larger than the power density, at the

same place, from a omnidirectional antenna. The ratio of these two power densities is called antenna gain ( $G$ ), unitless.  $G$  is defined in Equation (2.2).

$$G = \frac{\text{Maximum power density from directive antenna}}{\text{Isotropic Power density with same } P_t} \quad (2.2)$$

Therefore, the power density, in  $\text{W m}^{-2}$ , at a range,  $R$  from the radar is presented in Equation (2.3).

$$S_t(R) = \frac{P_t G}{4\pi R^2} \quad (2.3)$$

For the next part of the derivation, it is assumed that the transmitted signal illuminates a target  $R_1$  meters from the antenna. A portion of the energy radiating the target is absorbed, and the rest is scattered. The backscattered power is a function of the target's radar cross section ( $\sigma$ ) in  $\text{m}^2$ .  $\sigma$  has units of area, but it is not the physical area of the target.  $\sigma$  is proportional to the ratio of the power reflected over the power incident to the target. The backscattered power is radiated isotropically. Thus, for a receiver antenna located at a range  $R_2$  from the target, the power density backscattered to the receiver ( $S_b(R_1, R_2)$ ) is defined in Equation (2.4).

$$S_b(R_1, R_2) = \frac{P_t G}{4\pi R_1^2} \left( \frac{\sigma}{4\pi R_2^2} \right) \quad (2.4)$$

On receive, the power received by the antenna ( $P_r$ ), in Watts, is a function of its effective area ( $A_e$ ), in  $\text{m}^2$ , and the backscattered power density. The  $A_e$  can be defined as the multiplication of the physical area of the antenna ( $A$ ), in  $\text{m}^2$ , by the antenna aperture efficiency, unitless.  $P_r$  is expanded in Equation (2.5).

$$P_r = \frac{P_t G}{4\pi R_1^2} \left( \frac{\sigma}{4\pi R_2^2} \right) (A_e), \quad (2.5)$$

where  $A_e$  can be expressed as a function of  $G$  (see Equation (2.6)). For this derivation, it is assumed the same antenna is used for transmission and reception (“monostatic”).

$$A_e = \frac{G\lambda^2}{4\pi}, \quad (2.6)$$

where  $\lambda$  is the wavelength of the radar in meters.  $\lambda = c/f$ , where  $c$  is the speed of light  $c \approx 3 * 10^8 \text{ m s}^{-1}$  and  $f$  is the operating frequency of the radar, in Hz.

A simple form of the radar range equation for a point target is derived after replacing Equation (2.6) on (2.5) (see Equation (2.7)). Equation (2.7) is derived for a monostatic radar, so  $R = R_1 = R_2$ .

$$P_r = \frac{P_t G^2 \sigma \lambda^2}{(4\pi)^3 R^4} \quad (2.7)$$

Equation (2.7) is derived for a lossless medium. In the case of losses or attenuation (one-way  $l$ ) and assuming a monostatic radar, a new version of the radar equation results as in Equation (2.8).

$$P_r = \frac{P_t G^2 \lambda^2 \sigma}{(4\pi)^3 R^4 l^2} \quad (2.8)$$

Thus far,  $G$  has been considered a constant. However, the antenna gain is a function of the angular location  $(\theta, \phi)$ . The angular location is expressed in spherical coordinates. The antenna gain as a function of  $(\theta, \phi)$  is defined as the multiplication of  $G$  with the normalized power gain pattern ( $f_p^2(\theta, \phi)$ ), unitless.  $f_p^2(\theta, \phi)$ , which will be revisited in Section 2.3.

Equation (2.8) is now reformulated to include  $f_p^2(\theta, \phi)$  (see Equation (2.8)). The resulting Equation (2.8) is considered the complete radar range equation of point targets.

$$P_r = \frac{P_t G^2 f_p^4(\theta, \phi) \lambda^2 \sigma}{(4\pi)^3 R^4 l^2} \quad (2.9)$$

### 2.1.2 Radar Range Equation - Volume Scattering

In this section, the radar range equation will be extended from point targets to the case of volume scattering or “weather” (e.g., weather radar equation). Different from point targets, the mean power received from a weather signal ( $P_w$ ), located  $R$  meters away from the radar, is the integral of the received power from each hydrometeor enclosed within a specific volume (see Equation (2.10)) [2, 6, 65].

$$P_w = \int_{r_v} \int_{\theta} \int_{\phi} \int_D \frac{P_t G^2 f_p^4(\theta, \phi) \lambda^2 \sigma}{(4\pi)^3 R^4 l^2} dD R^2 dr \sin(\theta) d\theta d\phi, \quad (2.10)$$

where the first three integrals are related to the dimensions of the scattering volume and the fourth is the diameter ( $D$ ) of the hydrometeors (in meters).

Not all scatters have the same contribution to the echo power. The power contribution is a range-dependent weighting function, called the range-weighting function ( $|W(r)|$ ), that is included in the calculation of the return power.

$$P_w = \int_{r_v} \int_{\theta} \int_{\phi} |W(r)| \left( \int_D \sigma dD \right) \frac{P_t G^2 \lambda^2}{(4\pi)^3 R^2 l^2} f_p^4(\theta, \phi) dr \sin(\theta) d\theta d\phi \quad (2.11)$$

For the weather radar equation,  $\sigma$  is defined as the radar cross section per unit volume, where  $\sigma$  is expressed as the multiplication of the radar cross-section of each hydrometeor with diameter  $D$  ( $\sigma_d(D)$ ) multiplied by the particle size distribution at

that diameter ( $N(D)$ ). This changes Equation (2.11) to the following expression:

$$P_w = \int_{r_v} \int_{\theta} \int_{\phi} |W(r)| \left( \int_D \sigma_d(D) N(D) dD \right) \frac{P_t G^2 \lambda^2}{(4\pi)^3 R^2 l^2} f_p^4(\theta, \phi) dr \sin(\theta) d\theta d\phi. \quad (2.12)$$

Assuming that all hydrometeors observed within the scattering volume are spherical droplets in the Rayleigh regime,  $D$  is much smaller than the wavelength ( $\lambda \gg D$ ), then  $\sigma_d$  can be expressed as follows [2, 66]:

$$\sigma_d(D) = \frac{\pi^5}{\lambda^4} |K_w|^2 D^6, \quad (2.13)$$

where  $K_w$  is the complex dielectric factor, unitless.  $K_w$  changes depending on the presence of water or ice.  $|K_w|^2$  of ice is  $\approx 0.18$ ,  $|K_w|^2$  of water is  $\approx 0.92$ . Thus, Equation (2.14) is obtained by replacing Equation (2.13) in the integration in the  $D$  domain from Equation (2.12).

$$\int_D \sigma_d(D) N(D) dD = \frac{\pi^5}{\lambda^4} |K_w|^2 \int_D D^6 N(D) dD \quad (2.14)$$

Doviak and Zrnic [2] define that the integral  $\int_D D^6 N(D) dD$  as equal to the radar reflectivity factor ( $Z$ ) in  $\text{mm}^6/\text{m}^3$ .  $Z$  is often expressed in dB normalized to  $1 \text{ mm}^6/\text{m}^3$  as  $10 \log_{10} Z$ , in dBZ.  $Z$  values are related to the density, size, and even phase of water droplets per unit of volume [2]. If Equation (2.14) is rewritten in terms of  $Z$  and combined with Equation (2.12), the following results.

$$P_w = \int_{r_v} \int_{\theta} \int_{\phi} |W(r)| \left( \frac{\pi^5}{\lambda^4} |K_w|^2 Z \right) \frac{P_t G^2 \lambda^2}{(4\pi)^3 R^2 l^2} f_p^4(\theta, \phi) dr \sin(\theta) d\theta d\phi \quad (2.15)$$

By extracting assumed constants, Equation (2.15) can be simplified to

$$P_w \approx \frac{\pi^2 P_t G^2 |K_w|^2 Z}{2^6 R^2 l^2 \lambda^2} \int_{r_v} |W(r)| dr \int_{\theta} \int_{\phi} f_p^4(\theta, \phi) \sin(\theta) d\theta d\phi, \quad (2.16)$$

where the solution to  $\int_{r_v} |W(r)| dr$  is provided below [2, 67]. It should be noted that this solution includes calibration corrections.

$$\int_{r_v} |W(r)| dr = \frac{c\tau g_s}{2l_r}, \quad (2.17)$$

where  $\tau$  is the pulse width, in meters,  $g_s$  is the system power gain, unitless, and  $l_r$  is a loss factor due to the finite bandwidth of the receiver.

Doviak and Zrnice [2] derived an approximate solution to the integral  $\int_{\theta} \int_{\phi} f_p^4(\theta, \phi) \sin(\theta) d\theta d\phi$ , assuming the antenna radiation pattern is Gaussian-like and circularly symmetric.

$$\int_{\theta} \int_{\phi} f_p^4(\theta, \phi) \sin(\theta) d\theta d\phi = \frac{\pi\theta_1^2}{8\ln(2)}, \quad (2.18)$$

where  $\theta_1$  is the 3-dB width of the one-way pattern, in radians. Combining these results,

$$P_w = \frac{\pi^2 P_t G^2 |K_w|^2 Z}{2^6 r^2 l^2 \lambda^2} \frac{c\tau g_s}{2l_r} \frac{\pi\theta_1^2}{8\ln(2)}. \quad (2.19)$$

The final result is known as the weather radar range equation, and is provided below.

$$P_w = \frac{\pi^3 P_t G^2 g_s \theta_1^2 c\tau |K_w|^2 Z}{2^{10} \ln(2) R^2 l^2 l_r \lambda^2} \quad (2.20)$$

### 2.1.3 Radar Sensitivity

Radar sensitivity ( $Z_{\min}$ ) is the minimum radar reflectivity factor at a given range  $R$  that can be detected (usually defined as 0 dB SNR). The lower the value of  $Z_{\min}$ , the better the radar sensitivity. To mathematically explain the radar sensitivity, the  $Z$  Equation (2.21) is derived from Equation (2.20).

$$Z = \frac{P_w 2^{10} \ln(2) R^2 l^2 l_r \lambda^2}{\pi^3 P_t G^2 g_s \theta_1^2 c \tau |K_w|^2} \quad (2.21)$$

For the calculation of  $Z_{\min}$ , it is assumed that  $P_w$  is equal to the power from the noise floor ( $P_n$ ) in watts (0 dB SNR), which is different depending on the radar system. The radar sensitivity equation is presented in Equation (2.22).

$$Z_{\min} = \frac{P_n 2^{10} \ln(2) R^2 l^2 l_r \lambda^2}{\pi^3 P_t G^2 g_s \theta_1^2 c \tau |K_w|^2} \quad (2.22)$$

$Z_{\min}$  is inversely proportional to  $\tau$ , so the larger  $\tau$  gets, the lower  $Z_{\min}$  becomes, increasing the sensitivity of the radar. In addition,  $Z_{\min}$  is directly proportional to  $R$  so  $Z_{\min}$  values increase with larger range.

## 2.2 Pulse Compression

Range resolution ( $\Delta R$ ), in meters, is an essential specification on weather radars. The range resolution is calculated as a function of the Bandwidth of the transmitted pulse ( $B$ ) in Hz (see Equation (2.23)).

$$\Delta R = \frac{c}{2B} \quad (2.23)$$

Nevertheless, for single-tone, non-modulated pulses, the range resolution is instead



proportional to the pulse width ( $\tau$ ) (see Equation (2.24) [64]). Therefore, it is generally necessary to use a short pulse to obtain good range resolution.

$$\Delta R = \frac{c\tau}{2} \quad (2.24)$$

On pulsed radars, for the radar sensitivity calculations,  $P_t$  in Equation (2.22) may be replaced by the average power ( $P_{av}$ ).

$$Z_{\min} = \frac{P_n 2^{10} \ln(2) R^2 l^2 l_r \lambda^2}{\pi^3 P_{av} T_s G^2 g_s \theta_1^2 c |K_w|^2}, \quad (2.25)$$

with

$$P_{av} = P_t \frac{\tau}{T_s}, \quad (2.26)$$

where  $T_s$  is the PRT, and  $\tau/T_s$  is defined as the duty cycle ( $d$ ).

In Equation (2.26), it is observed that  $P_{av}$  is directly proportional to the duty cycle. The duty cycle is not a significant limitation to fulfill the sensitivity requirements on systems with high  $P_t$ , hundreds of kW. In contrast, the duty cycle is a limitation on systems where  $P_t$  is low, as is the case with solid-state radars. There are two possible solutions to increase  $P_{av}$  on solid-state systems. One is to reduce  $T_s$ , inversely proportional to  $P_{av}$ . Unfortunately, reducing  $T_s$  reduces the maximum observable range increasing the potential for multi-trip echoes (the maximum observable range is directly proportional to  $T_s$ ) [64]. The second solution is to increase  $\tau$ , but this would adversely affect the range resolution of the system (proportional to  $\tau$ ) if measures are not taken to mitigate this negative impact.

Pulse compression (PC) is just such a mitigation strategy capable of solving the previously described limitation. Conventional PC techniques use a frequency or phase modulated pulse that is “compressed” using a matched filter. By doing so, the connec-

tion of range resolution and pulse length is eliminated. In contrast, the range resolution is actually inversely proportional to  $B$ . PC allows a system to transmit a waveform with a  $\tau$  large enough to provide a  $P_{av}$  capable of fulfilling the radar sensitivity requirement but modulated with a  $B$  large enough that the range resolution is still comparable to a short pulse.

Figure 2.1 is presented as a good visualization tool to understand PC for the case of a Linear frequency modulated (LFM) waveform. Figure 2.1 was extracted from Skolnik [1] and modified for visualization purposes.

From Figure 2.1d, the amplitude of the compressed pulse is equal to  $\sqrt{BT}$ , where  $B \approx \tau_c^{-1}$ , and  $\tau_c$  is the compressed pulse width, in meters.  $BT$  is called the compression ratio, defined as the ratio of power from the long pulse (before pulse compression) over the power from an uncompressed short pulse with  $\tau = \tau_c$ .

With improvements in range resolution, PC does cause so-called “range sidelobes,” which are smaller secondary lobes leaked on both sides of the compressed main lobe [1, 64, 68]. The power difference between the main lobe peak and the first sidelobe peak is called the sidelobe level. The range sidelobe level of a system is important for weather applications. A standard solution to reduce these sidelobes is to multiply the designed waveform by a window in time (“pulse taper”), or frequency domain [6, 38, 68, 69]. The sidelobe issue will be revisited in Chapters 3 and 5.

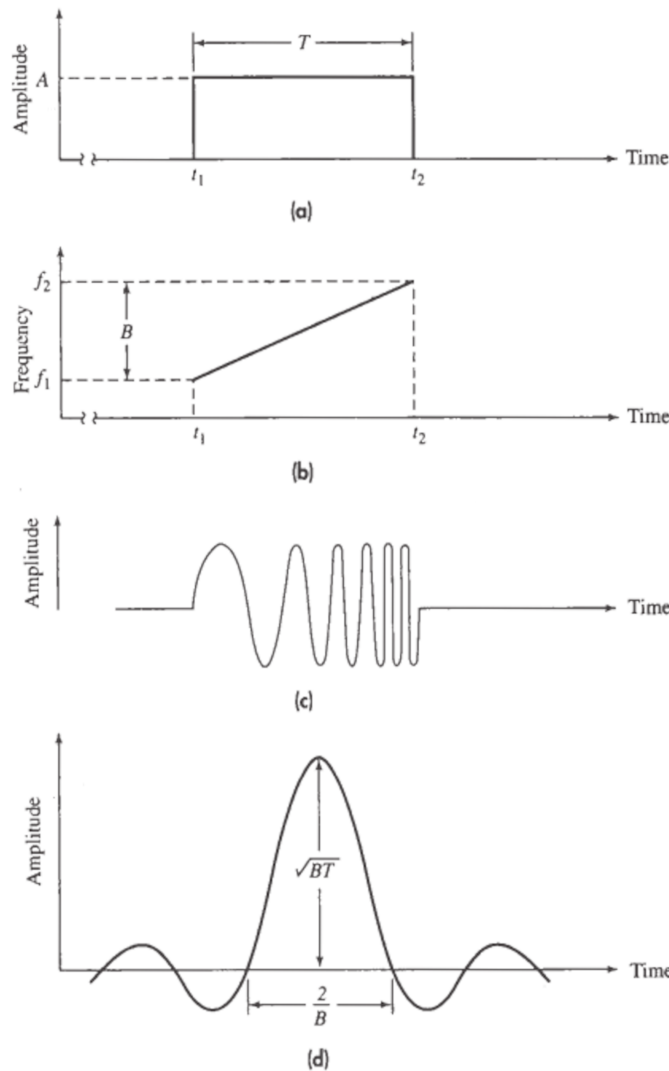


Figure 2.1: The principle of pulse compression, from [1].(a) Envelope of the transmitted waveform, (b) Frequency of the transmitted waveform vs. time, (c) LFM waveform, and (d) theoretical output of pulse compression.

Yet another limitation of PC is the fact that the use of a long pulse creates a “blind range,” as explained in Section 1.1. A proper technique to mitigate the blind range is critical for radar systems based on pulse compression. This topic will be addressed in Chapters 3 and 5).

In summary, to have the best performance on PC, the design of the long waveform

is crucial. It is necessary to consider the  $\tau$ , the  $B$  of the modulation, the technique for frequency or phase modulation, and the waveform tapering.

## 2.3 Phased Array Radar Fundamentals

As defined in Section 1.1, phased array radar systems are based on phased array antennas. Phased array antennas can improve the temporal resolution of a system compared to reflector antennas (through electronic steering). Other advantages of phased array antennas include the reduced mechanical complexity of the radar, maintenance costs, and the improvement in the rotational inertia and pointing precision [70].

A phased array antenna is a collection of elements (antennas) capable of transmitting and receiving electromagnetic waves (see Section 1.1). Digital beamforming is a pivotal characteristic of phased array antennas, and it is functional even when a subgroup of elements is inoperative. Still, the performance decreases directly proportional to the number of inoperable elements. The effect is referred to as graceful degradation, and it significantly increases the lifetime and reliability of a phased array radar [70]. This section will discuss the fundamentals of phased array radars, including the design parameters and implications, the phased array radar scanning, and the equations involved. It will also explore the problems and downsides of this technology.

### 2.3.1 Array Analysis

To properly analyze a phased array radar and to derive the array pattern, the definition of radiating field regions must be revisited [71, 72]. In space, three radiating field regions are defined as a function of their distances from the radiating source. The nearest region from the radiation source is called the reactive near-field region. In the reactive near-field region, the relation between the electric ( $E$ ) and magnetic ( $H$ ) fields is difficult to

predict, and the power calculations are complex. The following region is the radiating near-field region. There,  $E$  and  $H$  are more predictable. In that region, the field's angular distribution and direction of the power flow change depending on the distance from the source. The farthest region from the radiating source is called the far-field. In the far-field region,  $E$  and  $H$  are perpendicular to each other and the distance vector. The power is also flowing in the direction of the distance vector.

The antenna measurements and the array pattern calculation are generally performed in the far-field region. The far-field region starts approximately at a distance  $R_{\text{ff}}$  from a phased array antenna.  $R_{\text{ff}}$  is defined in Equation (2.27).

$$R_{\text{ff}} = \frac{2L^2}{\lambda}, \quad (2.27)$$

where  $L$  is the largest dimension of a phased array antenna in meters.

For a phased array antenna, the field generated from the  $i^{\text{th}}$  element, observed at a distance  $R_i$  in meters (far-field), is defined in Equation (2.28) [28, 71].

$$E_i(r, \theta, \phi) = \frac{f_i(\theta, \phi) \exp(-jkR_i)}{R_i}, \quad (2.28)$$

where  $f_i(\theta, \phi)$  is the element pattern.  $f_i(\theta, \phi)$  is a vector that models the field depending on the angular direction and depends on the element used, i.e., monopoles, dipoles, patch antennas.  $k$  is called the free-space wavenumber, defined as  $k = 2\pi/\lambda$ .  $R_i$  is defined as

$$R_i \approx R_a - \mathbf{r}_i \hat{r}, \quad (2.29)$$

where  $R_a$  is the direction from a location set as the origin to  $R_i$ ,  $\mathbf{r}_i$  is the position vector of the  $i$  radiating element respect to the defined origin, and  $\hat{r}$  is the unit vector pointing to a location.

Replacing  $R_i$  in Equation (2.28) results in the following

$$E_i(r, \theta, \phi) = \frac{f_i(\theta, \phi) \exp(-jk(R_a - \mathbf{r}_i \hat{r}))}{R_a - \mathbf{r}_i \hat{r}}. \quad (2.30)$$

In the far-field,  $R_a \gg \mathbf{r}_i \hat{r}$ , then  $R_a + \mathbf{r}_i \hat{r} \approx R_a$ . However, the previous assumption is not applicable in phase  $\exp(-jk(R_a - \mathbf{r}_i \hat{r}))$ . Then, Equation (2.30) is simplified in Equation (2.31).

$$E_i(r, \theta, \phi) = \frac{f_i(\theta, \phi) \exp(-jk(R_a - \mathbf{r}_i \hat{r}))}{R_a} \quad (2.31)$$

Each element in a phased array antenna is weighted by a factor  $a_i$ .  $a_i$  modifies Equation (2.31) (see (2.32))

$$E_i(r, \theta, \phi) = a_i \frac{f_i(\theta, \phi) \exp(-jkR_a)}{R_a} \exp(jk\mathbf{r}_i \hat{r}). \quad (2.32)$$

When a phased array radar transmits, each element field integrates with the others in space. The integrated field is called the array pattern. An approximation of the array pattern is presented in Equation (2.34).

$$E(r, \theta, \phi) = \sum_i a_i \frac{f_i(\theta, \phi) \exp(-jkR_a)}{R_a} \exp(jk\mathbf{r}_i \hat{r}) \quad (2.33)$$

$$E(r, \theta, \phi) = \frac{\exp(-jkR_a)}{R_a} \sum_i a_i f_i(\theta, \phi) \exp(jk\mathbf{r}_i \hat{r}) \quad (2.34)$$

Assuming the same element technology is used throughout the array, Equation (2.34) is changed to (2.35).

$$E(r, \theta, \phi) = f(\theta, \phi) \frac{\exp(-jkR_a)}{R_a} \sum_i a_i \exp(jk\mathbf{r}_i \hat{r}) \quad (2.35)$$

The calculation of the array factor, is extracted from Equation (2.35) (see Equation (2.36)).

$$F(\theta, \phi) = \sum_i a_i \exp(jk\mathbf{r}_i \hat{r}) \quad (2.36)$$

Equation (2.35) corresponds to the complete form of the array pattern. It is assumed that the wave transmitted from an element is only affected by the weight  $a_i$  for that element. But, the  $a_i$  term includes the weight from the  $i^{\text{th}}$  element and the field reflected from all elements. When the  $i^{\text{th}}$  element transmits a wave, part of it is absorbed by different elements in the array, or even by the same element, and then retransmitted by those elements. This is called mutual coupling and is included in the calculation.

Mutual coupling is estimated from the scattering-parameters or S-parameters incident to the element  $i$  and generated by the element  $k$  ( $S_{ik}$ ), multiplied by the weighting factor of the element  $k$ . Thus, accounting for the mutual coupling effect, the weighting factor in (2.35) will be rewritten as the expression in (2.37) [28].

$$a_i = a_i + \sum_k S_{ik} a_k \quad (2.37)$$

The array pattern derived in Equation (2.35) corresponds to the antenna pointing broadside. Electronically steering the beam will modify this equation (see Section 2.3.3).

### 2.3.2 Array Geometry

The performance of a phased array radar depends on the phased array antenna dimensions and the distribution of its elements. In other words, the larger the antenna, the narrower the 3-dB beamwidth ( $\theta_3$ ) at broadside (see Equation (2.38)) [28].

$$\theta_{3(\text{broadside})} = \frac{0.886B_b\lambda}{L_q}, \quad (2.38)$$

where  $B_b$  is termed the beam broadening factor, unitless.  $B_b$  is a factor of the illumination function of the antenna, related to the amplitude scaling of the elements within ( $|a_i|$ ).  $L_q$  is the physical size of the antenna, in meters, in the axis  $q$  of the antenna (generally related to the number of elements in that axis).

Assuming a large number of elements in the axis  $q$ ,  $L_q$  can be approximated as  $Md_q$ , where  $M$  is the total number of elements in the axis  $q$  and  $d_q$  is the distance between elements in the axis  $q$ .

The elements of a phased array antenna can be distributed as one or two-dimensional arrays. One-dimensional arrays are called linear arrays. The linear arrays have  $N$  elements on one axis and one element on the other. From (2.38),  $\theta_3$  is inversely proportional to  $L_q$ . The axis with one element produces a wide  $\theta_3$  and the perpendicular axis a good  $\theta_3$ . Thus, a linear array produces an array pattern with a fan-like beam. Obviously, it is only possible to steer the beam of a linear array along the dimension with more than one element.

A two-dimensional array is called a planar array where the elements are distributed in rows and columns, and both the number of rows and columns are higher than one. It is expected that  $\theta_3$  in both dimensions is narrow for planar arrays, producing a pencil beam shape of the array pattern, assuming the same number of elements in both dimensions. In the case of a planar array, it is possible to steer the array in both dimensions.

From (2.38),  $B_b$  is directly proportional to  $\theta_3$  and related to  $|a_i|$ .  $|a_i|$ , unitless, is the illumination of the element  $i$ , normalized to unity. The modulation of the  $B_b$  in an array is analogous to the concept of tapering in a waveform. Therefore, progressively reducing the illumination of the elements as they get closer to the borders positively



affects the sidelobe levels on the array pattern. For planar arrays, the modulation of the  $B_b$  can be performed independently on each dimension.

Modulating the  $B_b$  negatively impacts the gain of the antenna.  $|a_i|$  bounds the amount of energy transmitted by the  $i^{\text{th}}$  element. In addition, reducing the sidelobe level on each “tapered” dimension widens the main lobe, increasing  $\theta_3$ , as expressed on (2.38).

### 2.3.3 Phased Array Radar Scanning

In Section 2.3.1, the author derived the antenna array pattern equation of a phased array antenna pointing broadside. Still, one advantage of phased array radars is the ability to be electronically steered in space. In this section, Equation (2.35) is expanded. The new equations correspond to the array pattern of a linear or planar array steered in any direction within the scanning region [28]. The equation of a linear array is derived first.

The electronic beam steering of a phased array radar is achieved by phase shifting each element on the array. Geometry is key in calculating the phase shifting factor. An illustration of the steering concept is presented in Figure 2.2.

A linear array with  $N$  elements is presented in Figure 2.2. Originally, the array beam points broadside, assuming no modifications are made (black arrow). However, the radar can steer its beam  $\theta_0$  degrees off the broadside (blue arrow). Assuming no physical movement is involved, the beam steering could be performed by transmitting a time-delayed version of a waveform at each element. The time delay factor is different from element to element. In space, the time-delayed waveforms would constructively interfere with each other, changing the beam direction proportional to the time delay between elements.

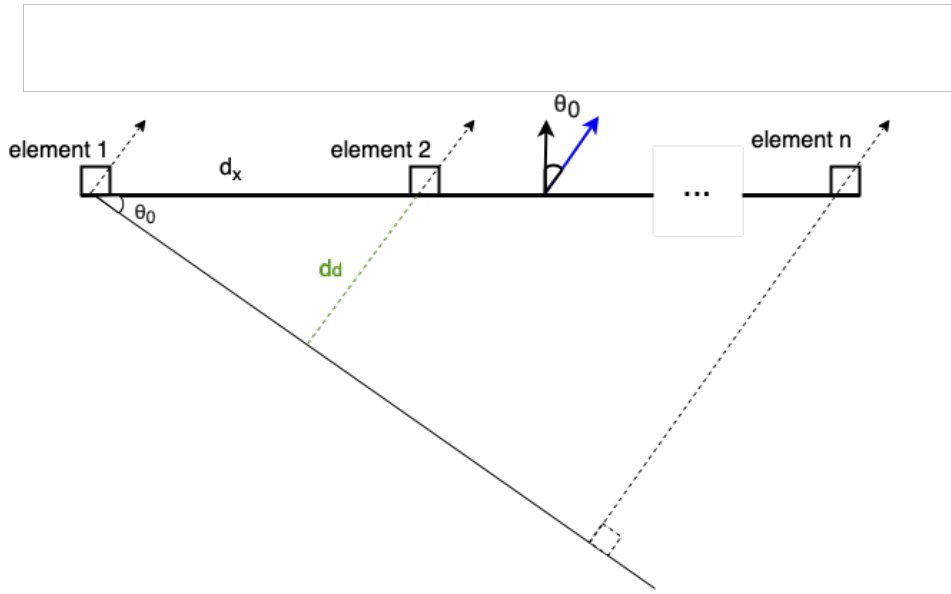


Figure 2.2: Visual representation of steering in a linear array. Array pointing broadside (black arrow) but electronically steered  $\theta_0$  degrees off the broadside (blue arrow).

For a positive value of  $\theta_0$ , the first element to transmit must be element  $n$ . On the contrary, for a negative value of  $\theta_0$ , the first element to transmit is element 1. Assuming element 1 is transmitting last (at time  $t$ ), element 2 would transmit  $d_d/c$  seconds before element 1. In general the time when element  $i$  would transmit ( $t_i$ ) is calculated in terms of the distance between elements  $d_x$ , in meters, and the steering angle  $\theta_0$  (see Equation (2.39)).

$$t_i = t - (i - 1) \frac{d_x \sin(\theta_0)}{c} \quad (2.39)$$

There are phased array radars using time-delayed pulses, termed true time-delay beamsteering. However, the implementation of time-delay beamsteering is impractical. Another solution for beam steering is to phase-shift the pulses to simulate such time delay, a commonly applied solution. Nevertheless, beam steering using a phase shifter has some drawbacks compared to true-time delay beamsteering. E.g., the shift in the

steering location corresponding to a frequency shift (“beam squint”) and the gain loss it causes. The beam squint and gain loss increase as the beam is steered away from the broadside and for narrow beams. Thus, for a system with larger bandwidth, narrow beams, or extended scanning regions, it is more appropriate to use true time-delay steering [73, 74].

For systems using phase shifters, the phase shift is different for each element. The phase shift of element  $i$  ( $PS_i$ ) is calculated based on Equation (2.39).

$$PS_i = \exp \left( j2\pi f \left( -(i-1) \frac{d_x \sin(\theta_0)}{c} \right) \right) \quad (2.40)$$

$$PS_i = \exp \left( \frac{-j2\pi(i-1)d_x \sin(\theta_0)}{\lambda} \right) \quad (2.41)$$

$$PS_i = \exp(-jk(i-1)d_x \sin(\theta_0)) \quad (2.42)$$

The phase shift affects all elements and is expressed as the phase of  $a_i$ . The reformulated  $a_i$  including the phase shift is presented in Equation (2.43).

$$a_i = |a_i| \exp(-jk(i-1)d_x \sin(\theta_0)) \quad (2.43)$$

The phase shift changes the equation of the antenna array pattern (see Equation (2.44)). The new antenna pattern equation is presented on Equation (2.44).

$$E(r, \theta, \phi) = f(\theta, \phi) \frac{\exp(-jkR_a)}{R_a} \sum_i |a_i| \exp(jk\mathbf{r}_i \hat{r}) \exp(-jk(i-1)d_x \sin(\theta_0)) \quad (2.44)$$

For a linear array, the distance  $\mathbf{r}_i \hat{r}$  is equivalent to  $(i-1)d_x \sin(\theta) \cos(\phi)$ . Thus,

The array pattern equation, of a linear array, when steering to  $\theta_0$  is presented in (2.45).

$$E(r, \theta, \phi) = f(\theta, \phi) \frac{\exp(-jkR_a)}{R_a} \sum_i |a_i| \exp(jk(i-1)d_x(\sin(\theta)\cos(\phi) - \sin(\theta_0))) \quad (2.45)$$

Different from linear arrays, planar arrays can be steered in two dimensions. The steering angle is defined as  $(\theta_0, \phi_0)$ .

Assuming a planar array located on the XY plane, with  $M$  column and  $N$  rows of element ( $M * N$  elements), the element in origin (not phase-shifted) is the element in the first row first column. Assuming the distance between columns of elements is constant and is defined as  $d_x$ , and the distance between rows of elements is  $d_y$ . The time delay of an element in the  $m^{\text{th}}$  column and  $n^{\text{th}}$  row ( $TD_{mn}$ ) is described in Equation (2.46) [28].

$$TD_{mn} = -(m-1) \frac{d_x \sin(\theta_0) \cos(\phi_0)}{c} \hat{x} - (n-1) \frac{d_y \sin(\theta_0) \sin(\phi_0)}{c} \hat{y} \quad (2.46)$$

Derived from the previous equation, the phase shift of the element  $m,n$  ( $PS_{mn}$ ) is presented in (2.47).

$$PS_{mn} = \exp \left( j2\pi f \left( -(m-1) \frac{d_x \sin(\theta_0) \cos(\phi_0)}{c} \hat{x} - (n-1) \frac{d_y \sin(\theta_0) \sin(\phi_0)}{c} \hat{y} \right) \right) \quad (2.47)$$

$$PS_{mn} = \exp(-jk((m-1)d_x \sin(\theta_0) \cos(\phi_0) \hat{x} + (n-1)d_y \sin(\theta_0) \sin(\phi_0) \hat{y})) \quad (2.48)$$

Therefore, the new scaling factor  $a_{m,n}$  changes and it presented in (2.49).

$$a_{m,n} = |a_{m,n}| \exp(-jk((m-1)d_x \sin(\theta_0) \cos(\phi_0) \hat{x} + (n-1)d_y \sin(\theta_0) \sin(\phi_0) \hat{y})) \quad (2.49)$$

The array pattern equation, of a planar array, when steering to  $(\theta_0, \phi_0)$  is presented in (2.50).

$$E(r, \theta, \phi) = f(\theta, \phi) \frac{\exp(-jkR_a)}{R_a} \sum_m \sum_n |a_{m,n}| \exp(jk\mathbf{r}_{m,n} \hat{r}) \exp(-jk((m-1)d_x \sin(\theta_0) \cos(\phi_0) \hat{x} + (n-1)d_y \sin(\theta_0) \sin(\phi_0) \hat{y})), \quad (2.50)$$

where  $\mathbf{r}_{m,n}$  is the position vector of the  $m,n$  radiating element respect to the defined origin. The  $\mathbf{r}_{m,n} \hat{r}$  expression can be approximated to the one in (2.51):

$$\mathbf{r}_{m,n} \hat{r} = \sin(\theta) \cos(\phi) \hat{x} + \sin(\theta) \sin(\phi) \hat{y}. \quad (2.51)$$

Replacing Equation (2.51) in (2.50), produces in the complete form of the array pattern of a planar array steered in the direction  $(\theta_0, \phi_0)$ , presented in Equation (2.52) [28].

$$\begin{aligned}
E(r, \theta, \phi) = f(\theta, \phi) \frac{\exp(-jkR_a)}{R_a} \sum_m \sum_n |a_{m,n}| \\
\exp(jk((m-1)d_x(\sin(\theta)\cos(\phi) - \sin(\theta_0)\cos(\phi_0)) \\
+ (n-1)d_y(\sin(\theta)\sin(\phi) - \sin(\theta_0)\sin(\phi_0)))) \quad (2.52)
\end{aligned}$$

The array pattern equations presented in Equations (2.52) and (2.45) are related to two variables described in the radar range equation, those are the antenna gain and  $f_p^2(\theta, \phi)$ .

There are drawbacks to digitally steering an array compared to steering a dish mechanically. For example, the presence of grating lobes, which appear as secondary beams contaminating the scan (see Section 2.3.4). In addition, the main beam becomes wider as the beam is steered off-broadside. Consequently, a phased array radar is generally steered within a delimited scanning region. For example, in this dissertation, the scanning region is limited from  $-45^\circ$  to  $45^\circ$  in azimuth and from  $0^\circ$  to  $20^\circ$  in elevation.

### **2.3.4 Grating Lobes and other Phased Array Radar Related Downsides**

Ideally, the array pattern equation produces a single peak at the steering angle. However, under certain circumstances related to the spacing between the elements, secondary peaks might appear at periodical distances from the main peak. These secondary peaks are called grating lobes [28, 75–77]. Grating lobes are adverse to the performance of the PARs. When grating lobes exist, the transmitted power is distributed between the main lobe and the grating lobes, impacting the gain of the system. Additionally, the grating lobes are falsely detected as additional targets in incorrect locations. Finally

grating lobes produce extra noise [28, 71, 77]. For a linear array, The angular location of a grating lobe  $\theta_p$ , as a function of the steering angle  $\theta_0$  is described in (2.53) (extracted from [28, 77]).

$$\sin(\theta_p) = \sin(\theta_0) + \frac{p\lambda}{d_x}, \quad (2.53)$$

where  $p$  is an integer ( $\pm 1, \pm 2, \pm 3, \dots$ ). The location and number of grating lobes is a function of  $d_x$ , generally expressed in  $\lambda$ s. E.g., if  $d_x = \lambda$ ,

$$\sin(\theta_p) = \sin(\theta_0) + \frac{p\lambda}{\lambda} \quad (2.54)$$

and

$$\sin(\theta_p) = \sin(\theta_0) + p. \quad (2.55)$$

From Equation (2.55), since  $|\sin(\theta_0)|$  and  $|\sin(\theta_p)|$  are  $\leq 1$ ,  $p = \pm 1$  fulfills the condition  $\sin(\theta_0) + p = \sin(\theta_p)$ , same for  $p = \pm 2$ . Nonetheless, higher values of  $p$  would not fulfill that requirement. Then, for a scanning sector from  $-\pi/2$  to  $\pi/2$ , one main lobe and two grating lobes can be found pointing at any combination of angles  $-\pi/2, 0$  and  $\pi/2$ . Thus, for  $d_x = \lambda$ , there are grating lobes every  $\pi/2$  degrees in the  $\theta$  direction.

The larger the distance  $d_x$ , the more grating lobes will appear, and the closer they will be to the main beam and one another. On the contrary, the shorter  $d_x$  is, the fewer grating lobes will be, and the farther away will be to the main beam and one another.

If  $d_x = \lambda/2$ ,

$$\sin(\theta_p) = \sin(\theta_0) + 2p. \quad (2.56)$$

From (2.55), since  $|\sin(\theta_0)|$  and  $|\sin(\theta_p)|$  are  $\leq 1$ ,  $p = \pm 1$  does fulfill the condition  $\sin(\theta_0) + p = \sin(\theta_p)$  if either  $\theta_0 = -\pi/2$  (the grating lobe will be at  $\theta_p = \pi/2$ ), or if

$\theta_0 = \pi/2$ , (grating lobe will be located at  $\theta_p = -\pi/2$ ). Therefore, a scanning sector from  $-\pi/2$  to  $\pi/2$  will only have a grating lobe if the beam is steered to the most extreme position. A practical conclusion is that, if  $d_x \leq \lambda/2$ , there are no grating lobes.

The location of the grating lobes on planar arrays is calculated similarly to the ones on a linear array. Nevertheless, on planar arrays, the steering and pointing angles are in both  $(\theta)$  and  $(\phi)$  directions. The angular location of the grating lobes for a planar array is presented in (2.57) (extracted from [28]).

$$\begin{aligned}\sin(\theta_{pq}) \cos(\phi_{pq}) &= \sin(\theta_0) \cos(\phi_0) + \frac{p\lambda}{d_x} \\ \sin(\theta_{pq}) \sin(\phi_{pq}) &= \sin(\theta_0) \sin(\phi_0) + \frac{q\lambda}{d_y},\end{aligned}\tag{2.57}$$

where  $p$  and  $q$  are integers  $(0, \pm 1, \pm 2, \pm 3, \dots)$  and the angular location of the grating lobes  $(\theta_{pq}, \phi_{pq})$  is expressed as a function of the steering angle, the distance between elements in both directions of the array and the wavelength.  $d_x$  and  $d_y$  are commonly expressed as a function of  $\lambda$ .

For linear arrays, it has been proven that, if  $d_x = \lambda/2$ , there are no grating lobes in the scanning region from  $-\pi/2$  to  $\pi/2$ . The same will be tested for a planar array when  $d_x = d_y = \lambda/2$  (see Equation (2.58)).

$$\begin{aligned}\sin(\theta_{pq}) \cos(\phi_{pq}) &= \sin(\theta_0) \cos(\phi_0) + 2p \\ \sin(\theta_{pq}) \sin(\phi_{pq}) &= \sin(\theta_0) \sin(\phi_0) + 2q\end{aligned}\tag{2.58}$$



Assuming the steering angle is (0,0), then

$$\begin{aligned}\sin(\theta_{pq}) \cos(\phi_{pq}) &= \sin(0) \cos(0) + 2p \\ \sin(\theta_{pq}) \sin(\phi_{pq}) &= \sin(0) \sin(0) + 2q\end{aligned}\tag{2.59}$$

$$\begin{aligned}\sin(\theta_{pq}) \cos(\phi_{pq}) &= 2p \\ \sin(\theta_{pq}) \sin(\phi_{pq}) &= 2q.\end{aligned}\tag{2.60}$$

$|\sin(\theta_{pq})| \leq 1$ ,  $|\sin(\phi_{pq})| \leq 1$  and  $|\cos(\phi_{pq})| \leq 1$ , using the multiplicative property of absolute values,  $|\sin(\theta_{pq}) \cos(\phi_{pq})| \leq 1$  and  $|\sin(\theta_{pq}) \sin(\phi_{pq})| \leq 1$ . Therefore,  $p = 0$  is the only solution to the equations, and the grating lobe peak is in the same location as the main peak (there are no grating lobes).

On the contrary, for  $d_x = d_y = \lambda/2$ , if the steering angle is  $(\pi/2, \pi/2)$ , the beam is pointing perpendicular to the YZ plane, and

$$\begin{aligned}\sin(\theta_{pq}) \cos(\phi_{pq}) &= \sin(\pi/2) \cos(\pi/2) + 2p \\ \sin(\theta_{pq}) \sin(\phi_{pq}) &= \sin(\pi/2) \sin(\pi/2) + 2q\end{aligned}\tag{2.61}$$

$$\begin{aligned}\sin(\theta_{pq}) \cos(\phi_{pq}) &= 2p \\ \sin(\theta_{pq}) \sin(\phi_{pq}) &= 1 + 2q.\end{aligned}\tag{2.62}$$

For the first equation in (2.62), if  $p = q = 0$ , there are grating lobes at the angles  $(\theta_{pq}, \phi_{pq})$  that satisfy  $\sin(\theta_{pq}) \cos(\phi_{pq}) = 0$  and  $\sin(\theta_{pq}) \sin(\phi_{pq}) = 1$ . The one angle satisfying the condition is located at  $(\pi/2, \pi/2)$ , and it is not a grating lobe but the steering angle. If  $p = 0$ ,  $q = -1$ , there are grating lobes in the angles  $(\theta_{pq}, \phi_{pq})$  that satisfy  $\sin(\theta_{pq}) \cos(\phi_{pq}) = 0$  and  $\sin(\theta_{pq}) \sin(\phi_{pq}) = -1$ . The grating lobe is located at  $(\pi/2, -\pi/2)$  and is pointing opposite to the main lobe but on the Y axis.

Finally, if  $d_x = d_y = \lambda/2$ , and the steering angle is  $(\pi/2, 0)$ , the beam is pointing

perpendicular to the XZ plane, and

$$\begin{aligned}\sin(\theta_{pq}) \cos(\phi_{pq}) &= \sin(\pi/2) \cos(0) + 2p \\ \sin(\theta_{pq}) \sin(\phi_{pq}) &= \sin(\pi/2) \sin(0) + 2q\end{aligned}\tag{2.63}$$

$$\begin{aligned}\sin(\theta_{pq}) \cos(\phi_{pq}) &= 1 + 2p \\ \sin(\theta_{pq}) \sin(\phi_{pq}) &= 2q.\end{aligned}\tag{2.64}$$

For the first equation in (2.64), if  $p = q = 0$ , there are grating lobes in the angle in the angles  $(\theta_{pq}, \phi_{pq})$  that satisfy  $\sin(\theta_{pq}) \cos(\phi_{pq}) = 1$  and  $\sin(\theta_{pq}) \sin(\phi_{pq}) = 0$ . The one angle satisfying the condition is located at  $(\pi/2, 0)$ , and it is not a grating lobe but the steering angle. If  $p = -1, q = 0$ , there are grating lobes in the angles  $(\theta_{pq}, \phi_{pq})$  that satisfy  $\sin(\theta_{pq}) \cos(\phi_{pq}) = -1$  and  $\sin(\theta_{pq}) \sin(\phi_{pq}) = 0$ . The grating lobe is located at  $(\pi/2, \pi)$  and is pointing opposite to the main lobe but on the X axis.

The previous exercise has been replicated for different combinations of steering angles and separation of elements. From the experiment, the author concluded the following about the location of the grating lobes. First, there are grating lobes if  $d_x$  or  $d_y$  are larger than  $\lambda/2$ . Second, the dimension where the grating lobes appear is related to the distance between elements in that dimension. For example, if  $d_x$  is larger than  $\lambda/2$ , but  $d_y$  is not, there will be only grating lobes parallel to the X axis. The same is true in the perpendicular dimension. If  $d_x$  and  $d_y$  are both larger than  $\lambda/2$ , there will be grating lobes in both dimensions. Third, the larger the separation between elements in one direction, the more grating lobes will be, and the closer they will be to the main lobe and one another.

Aside from grating lobes, in Section 2.3.1 it was assumed that  $f(\theta, \phi)$  is the same for each element in the array if the same kind of element is used. In reality, the radiation patterns of the elements are affected by diffracted fields observed mainly at the

edges of the array. Those effects are generated from the radiated electromagnetic fields interacting with the edges or discontinuities on the phased array antenna. They spread differently depending on their incident angle and the geometry of the discontinuity. These effects are known in the antenna community as diffraction or edge effects [75, 78, 79].

Edge effects have a significant impact on the performance of the phased array radars and its cross-polar performance [78, 80]. It varies for each element pattern, so  $f(\theta, \phi)$  is replaced by  $f_i(\theta, \phi)$ . The edge effects are a function of the kind of element used, their position in the array, the physical distance from the borders of the array to the elements, the polarization transmitted, and others. Figure 2.3, extracted from Ortiz [80], is presented to illustrate the edge effects. In Figure 2.3 the individual  $f_i(\theta, \phi)$  from a 3x3 MPA are provided.

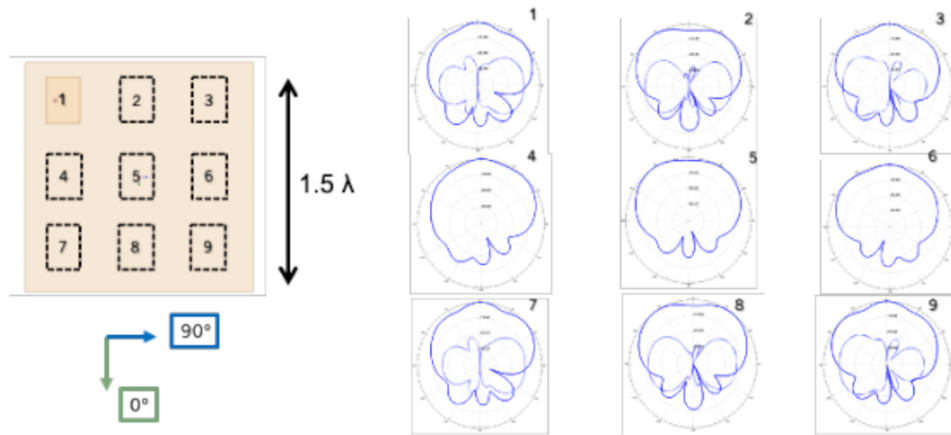


Figure 2.3: Diffraction effect observed on a 3x3 MPA. In the left plot, there is presented a schematic of the array. In the right plot, there are presented each of the  $f_i(\theta, \phi)$ , illustrating the edge effects. Extracted from [80].

Equations (2.35), (2.45) and (2.52) need to be modified to count for the diffraction effects. An alternative is to repurpose  $f(\theta, \phi)$ . Before, this term was related to the element pattern of all elements on the array. To maintain an approximately equal  $f(\theta, \phi)$

for all the elements,  $f(\theta, \phi)$  definition will be changed. Thus,  $f(\theta, \phi)$  will be defined as the derived average/embedded element pattern. Nevertheless, the previous alternative is based on an approximation. A better alternative is to change the  $f(\theta, \phi)$  inside the summations and replace it by  $f_i(\theta, \phi)$  or  $f_{m,n}(\theta, \phi)$ . Then, the equations will now be expressed as Equations (2.65), (2.66) and (2.67) respectively.

$$E(r, \theta, \phi) = \frac{\exp(-jkR_a)}{R_a} \sum_i a_i f_i(\theta, \phi) \exp(jk\mathbf{r}_i \hat{r}) \quad (2.65)$$

$$E(r, \theta, \phi) = \frac{\exp(-jkR_a)}{R_a} \sum_i |a_i| f_i(\theta, \phi) \exp(jk(i-1)d_x(\sin(\theta)\cos(\phi) - \sin(\theta_0))) \quad (2.66)$$

$$E(r, \theta, \phi) = \frac{\exp(-jkR_a)}{R_a} \sum_m \sum_n |a_{m,n}| f_{m,n}(\theta, \phi) \exp(jk((m-1)d_x(\sin(\theta)\cos(\phi) - \sin(\theta_0)\cos(\phi_0)) + (n-1)d_y(\sin(\theta)\sin(\phi) - \sin(\theta_0)\sin(\phi_0)))) \quad (2.67)$$

### 2.3.5 Cross-Polar Component and Contamination

Single and dual-polarized antennas transmit in a defined polarization. For linear polarization systems, the antenna transmits in either  $H$  or  $V$  polarization, perpendicular to each other. Ideally, when an antenna transmits or receives an electromagnetic wave, it is purely in a particular polarization. However, the isolation between the  $H$  and  $V$  ports in the antenna is not perfect, and there is a leak in the perpendicular polarization. This leak is increased by other factors including edge effects [80]. This leak is called a

cross-polar component and causes the cross-polar contamination.

The cross-polar contamination is not exclusive to phased array radars. Reflector antennas also suffer from this effect. However, a dish radar only has one beam to calibrate. For phased array radars, the cross-polar contamination is more problematic due to the several number of beams to calibrate.

The cross-polar component is derived from Equation (2.68), extracted from the work of Bringi and Chandrasekar [81], Zrnić *et al.* [82], and Ivić [83]. The equation corresponds to the echo voltage  $V_H(R_s, m)$  and  $V_V(R_s, m)$ , in volts, received from the radar resolution volume after the  $m^{\text{th}}$  pulse is transmitted, at a range  $R_s$ , in km, and from each polarization.

$$\begin{bmatrix} V_H(R_s, m) \\ V_V(R_s, m) \end{bmatrix} = C \begin{bmatrix} F_{HH} & F_{VH} \\ F_{HV} & F_{VV} \end{bmatrix} \mathbf{T}^T \begin{bmatrix} s_{HH} & 0 \\ 0 & s_{VV} \end{bmatrix} \mathbf{T} \begin{bmatrix} F_{HH} & F_{HV} \\ F_{VH} & F_{VV} \end{bmatrix} \begin{bmatrix} A_H(m) \\ A_V(m) \exp(j\beta) \end{bmatrix} \exp(-j2kR_s(m)), \quad (2.68)$$

where  $F$  represents the array factor with the antenna patterns from the array, in volts. If the two sub-indices are equal, i.e., HH or VV, it corresponds to the copolar fields ( $F_{HH}$  or  $F_{VV}$ ). In contrast, if the two indices are different, i.e., HV or VH, the term corresponds to the cross-polar fields ( $F_{HV}$  or  $F_{VH}$ ). The terms  $s_{HH}$  and  $s_{VV}$  represent the backscattering coefficient for the horizontal and vertical copolarization, unitless.  $\beta$  is the phase difference between  $H$  and  $V$  transmitter paths.  $A_H$  and  $A_V$  are the excitation amplitude components, unitless.  $A_H$  and  $A_V$  are normalized to unity.  $C$  is described as a factor containing the dependence on the range to the resolution volume, unitless.  $\mathbf{T}$  corresponds to the transmission matrix.  $\mathbf{T}$  represents the effects of the

weather across the propagation path, and it is defined in Equation (2.69).

$$\mathbf{T} = \begin{bmatrix} \exp(-j\phi_{\text{DP}}/2) & 0 \\ 0 & 1 \end{bmatrix}, \quad (2.69)$$

where  $\phi_{\text{DP}}$  correspond to the differential phase in radians.

For STSR mode, where  $H$  and  $V$  polarization are transmitted at the same time ( $A_H = A_V = 1$ ), Equation (2.71) is derived from Equation (2.68).

$$\begin{bmatrix} V_H(R_s, m) \\ V_V(R_s, m) \end{bmatrix} = C \begin{bmatrix} F_{\text{HH}} \exp(-j\phi_{\text{DP}}/2) & F_{\text{VH}} \\ F_{\text{HV}} \exp(-j\phi_{\text{DP}}/2) & F_{\text{VV}} \end{bmatrix} \begin{bmatrix} s_{\text{HH}} \exp(-j\phi_{\text{DP}}/2) & 0 \\ 0 & s_{\text{VV}} \end{bmatrix} \begin{bmatrix} F_{\text{HH}} + F_{\text{HV}} \exp(j\beta) \\ F_{\text{VH}} + F_{\text{VV}} \exp(j\beta) \end{bmatrix} \exp(-j2kR_s(m)) \quad (2.70)$$

$$\begin{bmatrix} V_H(R_s, m) \\ V_V(R_s, m) \end{bmatrix} = C \begin{bmatrix} F_{\text{HH}} s_{\text{HH}} \exp(-j\phi_{\text{DP}}) & F_{\text{VH}} s_{\text{VV}} \\ F_{\text{HV}} s_{\text{HH}} \exp(-j\phi_{\text{DP}}) & F_{\text{VV}} s_{\text{VV}} \end{bmatrix} \begin{bmatrix} F_{\text{HH}} + F_{\text{HV}} \exp(j\beta) \\ F_{\text{VH}} + F_{\text{VV}} \exp(j\beta) \end{bmatrix} \exp(-j2kR_s(m)) \quad (2.71)$$

The copolar components of  $V_H(R_s, m)$  and  $V_V(R_s, m)$  are presented in Equation (2.72).

$$\begin{bmatrix} V_{\text{H(co)}}(R_s, m) \\ V_{\text{V(co)}}(R_s, m) \end{bmatrix} = C \exp(-j2kR_s(m)) \begin{bmatrix} F_{\text{HH}}^2 s_{\text{HH}} \exp(-j\phi_{\text{DP}}) \\ F_{\text{VV}}^2 s_{\text{VV}} \exp(j\beta) \end{bmatrix} \quad (2.72)$$

The cross-polar components of  $V_H(R_s, m)$  and  $V_V(R_s, m)$  are presented in Equations (2.73) and (2.74).

$$V_{H(\text{cross})}(R_s, m) = C \exp(-j2kR_s(m)) \{ F_{HH} F_{HV} s_{HH} \exp(j(\beta - \phi_{DP})) + F_{VH}^2 s_{VV} + F_{VH} F_{VV} s_{VV} \exp(j\beta) \} \quad (2.73)$$

$$V_{V(\text{cross})}(R_s, m) = C \exp(-j2kR_s(m)) \{ F_{HV} F_{HH} s_{HH} \exp(-j\phi_{DP}) + F_{HV}^2 s_{HH} \exp(j(\beta - \phi_{DP})) + F_{VH} F_{VV} s_{VV} \} \quad (2.74)$$

On the contrary, Equation (2.68) needs to be modified for radars transmitting on alternate transmission and simultaneous reception of  $H/V$  polarization mode (ATSR). For the case when only  $H$  polarization is transmitted,  $A_H = 1$  and  $A_V = 0$ , then:

$$\begin{bmatrix} V_H(R_s, m) \\ V_V(R_s, m) \end{bmatrix} = C \begin{bmatrix} F_{HH} & F_{VH} \\ F_{HV} & F_{VV} \end{bmatrix} \mathbf{T}^T \begin{bmatrix} s_{HH} & 0 \\ 0 & s_{VV} \end{bmatrix} \mathbf{T} \begin{bmatrix} F_{HH} & F_{HV} \\ F_{VH} & F_{VV} \end{bmatrix} \begin{bmatrix} 1 \\ 0 \end{bmatrix} \exp(-j2kR_s(m)) \quad (2.75)$$

$$\begin{bmatrix} V_H(R_s, m) \\ V_V(R_s, m) \end{bmatrix} = C \exp(-j2kR_s(m)) \begin{bmatrix} F_{HH}^2 s_{HH} \exp(-j\phi_{DP}) + F_{VH}^2 s_{VV} \\ F_{HV} F_{HH} s_{HH} \exp(-j\phi_{DP}) + F_{VH} F_{VV} s_{VV} \end{bmatrix}. \quad (2.76)$$

The co- and cross-polar component from (2.76) are presented in Equations (2.77) and (2.78).

$$\begin{bmatrix} V_{\text{H(co)}}(R_s, m) \\ V_{\text{V(co)}}(R_s, m) \end{bmatrix} = C \exp(-j2kR_s(m)) \begin{bmatrix} F_{\text{HH}}^2 s_{\text{HH}} \exp(-j\phi_{\text{DP}}) \\ 0 \end{bmatrix} \quad (2.77)$$

$$\begin{bmatrix} V_{\text{H(cross)}}(R_s, m) \\ V_{\text{V(cross)}}(R_s, m) \end{bmatrix} = C \exp(-j2kR_s(m)) \begin{bmatrix} F_{\text{VH}}^2 s_{\text{VV}} \\ F_{\text{HV}} F_{\text{HH}} s_{\text{HH}} \exp(-j\phi_{\text{DP}}) + F_{\text{VH}} F_{\text{VV}} s_{\text{VV}} \end{bmatrix} \quad (2.78)$$

A similar derivation is performed for the co- and cross-polar components for ATSR mode when the  $V$  component is transmitted. Therefore,  $A_{\text{H}} = 0$  and  $A_{\text{V}} = 1$ .

$$\begin{bmatrix} V_{\text{H}}(R_s, m) \\ V_{\text{V}}(R_s, m) \end{bmatrix} = C \begin{bmatrix} F_{\text{HH}} & F_{\text{VH}} \\ F_{\text{HV}} & F_{\text{VV}} \end{bmatrix} \mathbf{T}^{\text{T}} \begin{bmatrix} s_{\text{HH}} & 0 \\ 0 & s_{\text{VV}} \end{bmatrix} \mathbf{T} \begin{bmatrix} F_{\text{HH}} & F_{\text{HV}} \\ F_{\text{VH}} & F_{\text{VV}} \end{bmatrix} \begin{bmatrix} 0 \\ \exp(j\beta) \end{bmatrix} \exp(-j2kR_s(m)) \quad (2.79)$$



$$\begin{bmatrix} V_H(R_s, m) \\ V_V(R_s, m) \end{bmatrix} = C \exp(-j2kR_s(m)) \begin{bmatrix} F_{HH}F_{HV}s_{HH} \exp(j(\beta - \phi_{DP})) + F_{VH}F_{VV}s_{VV} \exp(j\beta) \\ F_{HV}^2s_{HH} \exp(j(\beta - \phi_{DP})) + F_{VV}^2s_{VV} \exp(j\beta) \end{bmatrix} \quad (2.80)$$

The co- and cross-polar component from (2.80) are presented in Equations (2.81) and (2.82).

$$\begin{bmatrix} V_{H(\text{co})}(R_s, m) \\ V_{V(\text{co})}(R_s, m) \end{bmatrix} = C \exp(-j2kR_s(m)) \begin{bmatrix} 0 \\ F_{VV}^2s_{VV} \exp(j\beta) \end{bmatrix} \quad (2.81)$$

$$\begin{bmatrix} V_{H(\text{cross})}(R_s, m) \\ V_{V(\text{cross})}(R_s, m) \end{bmatrix} = C \exp(-j2kR_s(m)) \begin{bmatrix} F_{HH}F_{HV}s_{HH} \exp(j(\beta - \phi_{DP})) + F_{VH}F_{VV}s_{VV} \exp(j\beta) \\ F_{HV}^2s_{HH} \exp(j(\beta - \phi_{DP})) \end{bmatrix} \quad (2.82)$$

## 2.4 Summary and the Need for Technical Solutions

Chapter 2 reviewed the fundamental concepts in weather radar signal processing, including the radar range equation, pulse compression, and the fundamentals of phased array radars. Of particular note, the blind range challenge and the need to mitigate cross-polar contamination was emphasized. Subsequent chapters will specifically address these two important challenges to the weather radar community.

In the next chapter, it is presented a signal processing technique (PPC) to mitigate the blind range in radar using pulse compression.

## **Chapter 3**

### **Progressive Pulse Compression**

This chapter focuses on the technical aspect of the PPC method [39, 84], which is one novelty of this dissertation.

As mentioned before, the PPC does not require the use of fill pulses. Therefore, no additional bandwidth is needed. Compared to other solutions in literature [42–44], the partial long pulse is generally longer than the fill pulse, which resulted in a sensitivity improvement inside the blind range. Additionally, the PPC is generally less expensive in bandwidth to implement.

#### **3.1 Methodology**

##### **3.1.1 Algorithm Description**

The PPC technique is intended for blind range mitigation for radars use frequency modulated pulses for PC. Partial decoding and PC methods are utilized where the data from different temporal samples is coherently integrated into a single sample. In the scope of PPC, all data within the transmission cycle is considered lost, the recovery of the blind range is accomplished by using the remaining data beyond the transmission cycle.

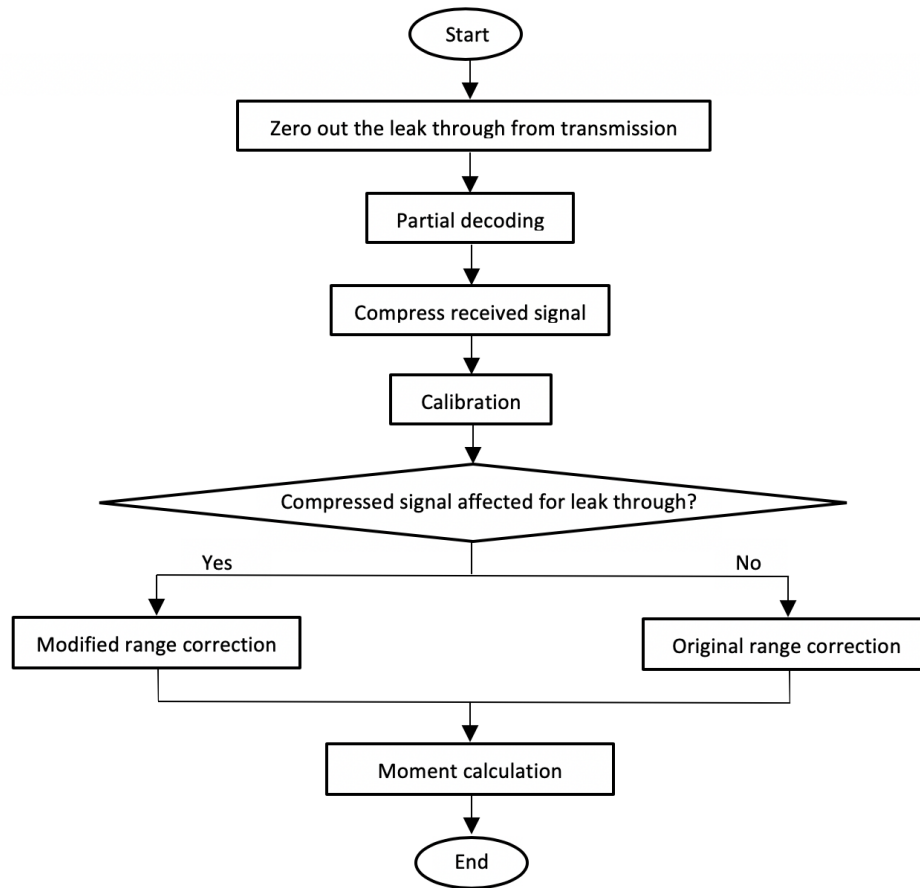


Figure 3.1: Flow chart of the PPC technique. Key differences from the PPC include using a window function to zero out the leak-through from the transmission, partial decoding, and a new calibration factor to estimate the reflectivity inside the blind range.

The algorithm is divided into three steps. First, the leak-through from the transmission into the receiver is eliminated where all samples with the leak-through contamination are replaced with zeros. Then, the remaining signals are partially decoded and compressed using a match filter. This is equivalent to performing a moving compression filter with a progressively changing width to match the usable length of the pulse, and hence the name Progressive Pulse Compression. Finally, the partially compressed

pulse is calibrated to correctly estimate the signal power or target reflectivity. The calibration is necessary since only a portion of the received signal is used for compression. A flow chart of the PPC technique is shown in Figure 3.1.

### **3.1.2 Leak-Through Elimination and Partial Decoding**

Figure 3.2 illustrates the concept of partial decoding. It can be observed that the received echoes from point targets have the same width as the transmit signal. If a target is located inside the blind range (target #1), conventional method, referred to as the legacy pulse compression (LPC), renders it unusable because the leak-through masks the desired signal. The composite signal includes the leak-through and the echoes from the targets (see the yellow line in the conventional method). However, the dynamic range of the receiver caps the maximum power that a radar can receive (saturation level), indicated by a dotted line on the composite plot of the conventional method. Consequently, the leak-through saturates the receiver inside the blind range, and the contribution from targets there is now obscured.

Nonetheless, the signal received from each target is long. A portion of the received signal is free from this contamination and not affected by the saturation (see the pink line in the new method column). If the target is located inside the blind range, the transmission leak-through only masks a portion of the return echo, leaving a tail portion free from the leak-through contamination. PPC uses the data from that tail portion to recover the obscured but desired target.

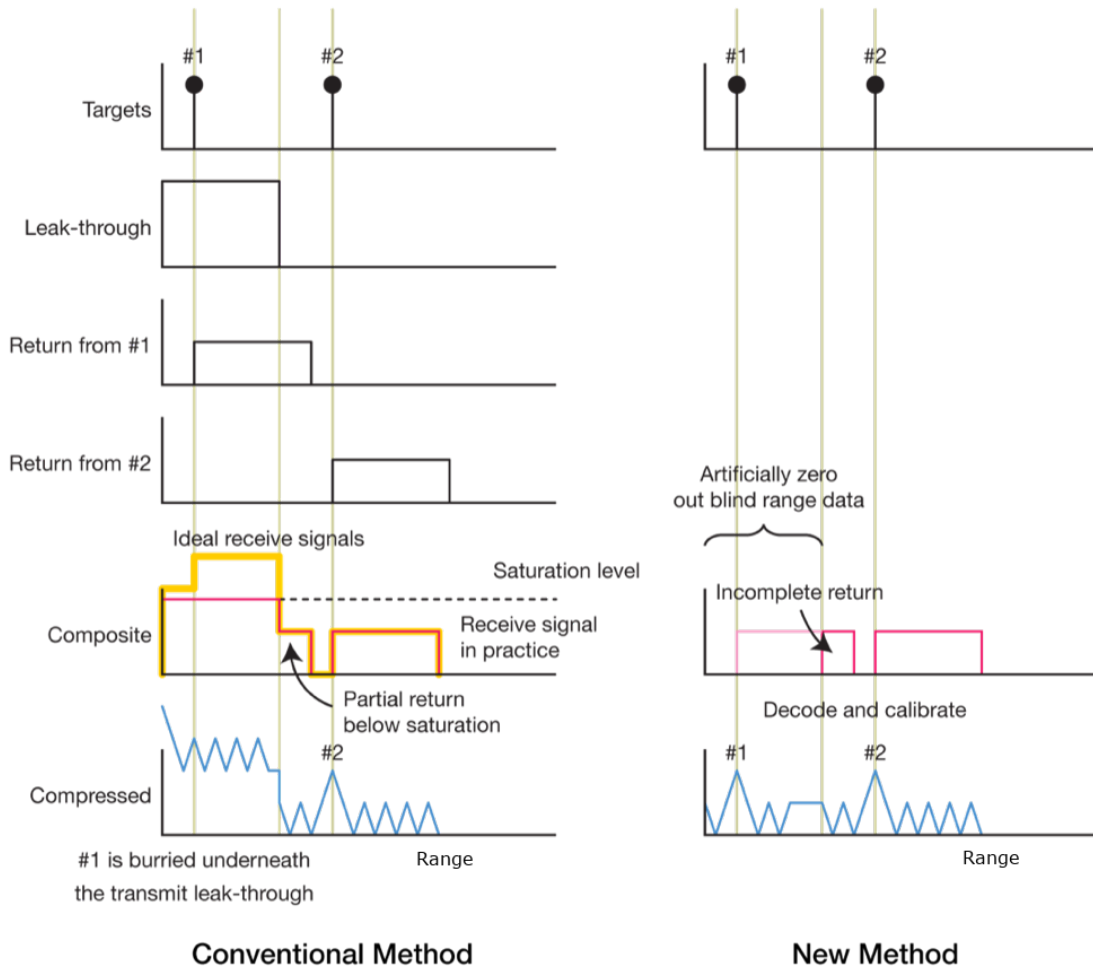


Figure 3.2: The principle of partial decoding. The target inside the blind range becomes obscured by strong leak-through when processed using the conventional method. When the PPC is applied, the target can be correctly estimated, as shown on the right.

For a target located  $R_t$  km away from the radar ( $R_t \leq R_b$ ), the return signal of the target spans the range  $R \in [R_t, R_t + R_p]$ , where  $R_p$  is the pulse length (see Equation (1.2)), and  $R_p = R_b$ . A strong leak-through obscures the first  $R_b$  meters. However, the signal usable for uncovering the target starts immediately after  $R_b$  and ends at the tail of the return ( $R_t + R_p$  meters). This is illustrated in Figure 3.3.

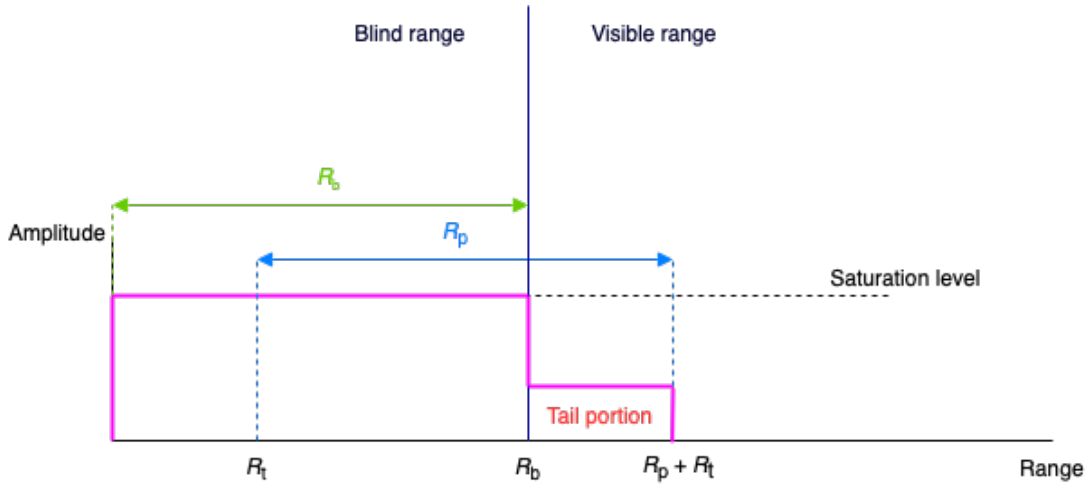


Figure 3.3: Illustration of the uncontaminated tail portion of a target inside the blind range. The tail portion is used for partial decoding in the PPC.  $R_b$  is the blind range. The received signal of a target located at  $R_t$  spans the range  $R \in [R_t, R_t + R_p]$ . Additionally,  $R_p = R_b$ .

A numerical example is examined here. Consider a 10 km pulse ( $R_p = 10$  km). If a target is located at 3 km, its signal return is observed from 3 to 13 km. The first 10 km are obscured but not the last 3 km of the return from the target. This 3-km tail portion is used for estimating the target.

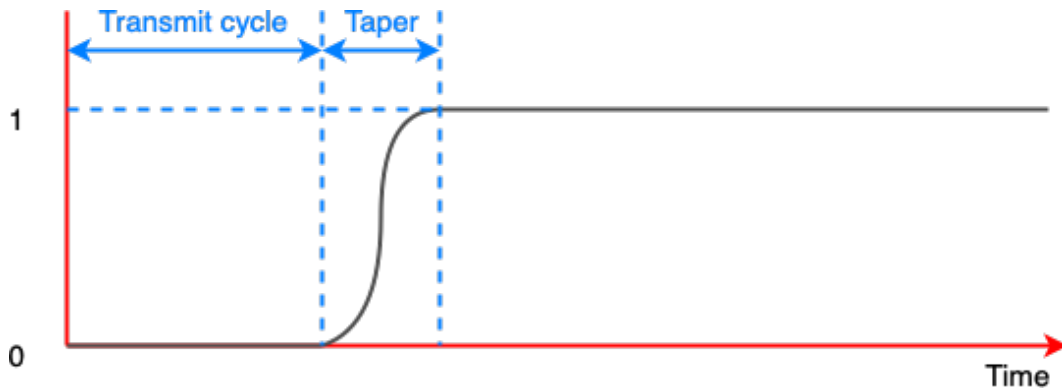


Figure 3.4: Depiction of the zeroing-out process. Received samples are replaced with zeros if they are within the transmit cycle. A taper, which is a gradual transition from zero to one is applied for reducing sidelobes of the pulse compression.

In addition to replacing the contaminated samples with zeros, a taper is also applied

to smooth the transition from zero to full amplitude of the receive signals. Figure 3.4 shows an example taper that mimics a raised cosine function. In this study, a width of  $67 \mu\text{s}$  provides a ramp-up time of  $4 \mu\text{s}$ .

The matched filter, shown in Equation (3.1), is used to compress the received signal [1, 85].

$$y(n) = \sum_{\tau} x(\tau + n)x_t^*(\tau), \quad (3.1)$$

where  $y(n)$  is the compressed signal,  $x(n)$  is the received signal,  $x_t(n)$  is the matched filter (template),  $(\cdot)^*$  is the complex conjugate operator and  $n$  corresponds to the sample index in range. As explained before, the received signal is multiplied by a window function  $w(n)$  to eliminate leakage from the transmission. The new received signal is expressed in Equation (3.2).

$$x'(n) = w(n)x(n) \quad (3.2)$$

Using the newly introduced zero-out and taper procedures, the PPC compressed signal  $y'(n)$  can be represented in Equation (3.3).

$$y'(n) = \sum_{\tau} x'(\tau + n)x_t^*(\tau) \quad (3.3)$$

The new compressed received signal is called a progressive compressed signal. The leak-through is eliminated. Because of using the residual tail of the received signals for compression, the progressive compressed signal needs to be compensated differently for reflectivity estimation.

### 3.1.3 Calibration

As mentioned earlier, it is necessary to calculate a calibration or compensating factor to estimate the reflectivity values correctly inside the blind range. Note that the uncontaminated tail portion is a function of range (Section 3.1.2). For example, using a 10-km transmit pulse, with two targets located at 5 km and 8 km, both of which are inside the blind range, the end of the return signals from each target will be at 15 and 18 km, respectively. After the windowing process, the remaining uncontaminated portions are 5 km (10-15 km) and 8 km (10-18 km) from these two targets (PPC only has this much signal from each target). Therefore, after compression, it is necessary to calibrate for approximately the 50% and 80% signal availability of these two targets (calibration considers the ramp-up in the window function), respectively, for reflectivity estimation. The calculation of the calibration factor is described next.

The calculation of the scaling factor is a function of the transmitted waveform, the window function, and the position in range of the target. The calibration factor is used to estimate the target reflectivity at each range. From Equation (3.3), the compressed signal  $y'(n)$  contains just a fraction of the received signal, and the required  $y(n)$  is the compressed signal if there is no leak-through and no blind range. It is impossible to obtain the  $y(n)$  wanted, but it can be estimated by multiplying a scaling factor, denoted as  $s(n)$ , to  $y'(n)$ . The estimated compressed signal is named  $y_e(n)$ .

$$y_e(n) = s(n)y'(n) \quad (3.4)$$

$$y_e(n) = s(n) \sum_{\tau} x'(\tau + n)x_t^*(\tau) \quad (3.5)$$

The scaling factor  $s(n)$  is derived from Equations (3.4) and (3.5), and is shown in Equation (3.6).



$$s(n) = \sqrt{\frac{\sum_{\tau} |x_t(\tau)|^2}{\sum_{\tau} |w(n + \tau)x_t(\tau)|^2}} \quad (3.6)$$

The new scaled and compressed output estimates the fully compressed received signal in the blind range, free from leak-through. This new scaled and compressed signal is used for radar product calculations (e.g., reflectivity factor, radial velocity, etc.). Calibration is the last step of this PPC algorithm. From here, the radar product calculation is done using standard implementations.

An in-depth analysis of the performance and advantages of PPC is presented in the following sections of this chapter. There are drawbacks in PPC. They include a loss in range resolution, a shift in the main lobe, and a decrease in sensitivity as the range gates are closer to the radar (discussed in detail in the following sections). Software improvements are proposed in Chapter 5 to reduce the first two drawbacks.

## 3.2 Advantages and Limitations of PPC

### 3.2.1 Sensitivity Analysis

The main advantage of using the PPC over the other blind-range filling methods [42–44] is the sensitivity ( $Z_{\min}$ ) gain inside the blind range. The  $Z_{\min}$  equation has been derived in Section 2.1.3 (see Equation (2.22)).

$Z_{\min}$  is inversely proportional to  $\tau$ . So, the larger  $\tau$  gets, the lower  $Z_{\min}$  becomes, increasing the sensitivity of the radar. Existing techniques to mitigate the blind range use a so-called fill pulse with a shorter  $\tau$  to fill in the blind range [42–44]. The data collected using the long pulse and short pulse are merged to produce a complete scan. Consequently, there is a jump in radar sensitivity between the blind range and the visible range.

On PPC, inside the blind range, the usable  $\tau$  ( $\tau_u$ ) changes as a function of range, and it is proportional to the portion of the pulse (range) that is free from the contamination. The expression for  $\tau_u$  is derived in (3.8).

$$\tau_u \approx \frac{2(R_p + R_t - R_b)}{c} \quad (3.7)$$

$$\tau_u \approx \frac{2R_t}{c} \quad (3.8)$$

Then, for PPC,  $Z_{\min}$  is approximately equal to the expression on Equation (3.9)).

$$Z_{\min} \approx \frac{P_n 2^{10} \ln(2) \lambda^2 R^2 l^2 l_r}{\pi^3 P_t G^2 g_s \theta^2 c \tau_u |K_w|^2} \quad (3.9)$$

$Z_{\min}(r)$  is inversely proportional to  $\tau_u$ , and it gradually decreases (improves) as the  $R$  increases.

To illustrate this effect, a routine to compute radar sensitivity (according to Equation (3.9)) for different blind range mitigation techniques has been developed. The results are shown in Figure 3.5.

Three sensitivity profiles are calculated using the PX-1000 system parameters ( $P_t = 200$  W and  $\tau = 67$   $\mu$ s) and they are shown as red solid line, black dashed line, and yellow solid line. A fourth sensitivity profile is calculated using  $P_t = 5$  kW and  $\tau = 0.5$   $\mu$ s and is shown as a green solid line. This can represent a low-cost magnetron-based system, such as the CASA IP-1 [86].

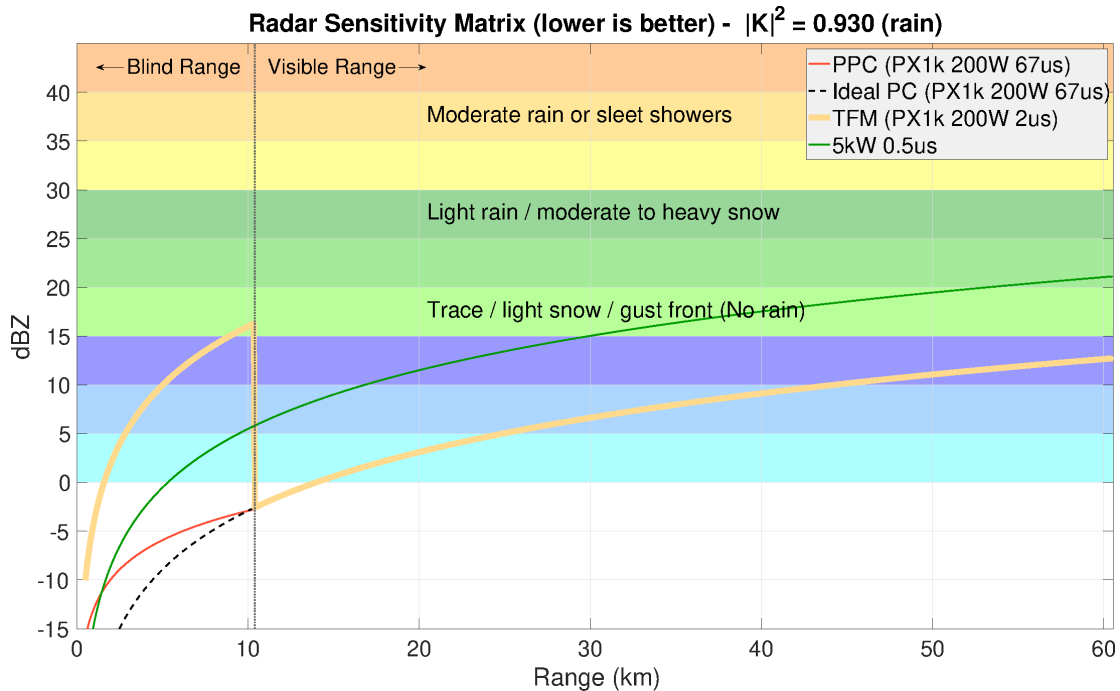


Figure 3.5: Radar sensitivity of different systems. PPC provides a smooth transition in sensitivity between the blind and visible ranges. In addition, PPC provides better sensitivity values inside the blind range compared to the time-frequency multiplexed waveform technique and has comparable sensitivity values to radar systems using higher power transmitters.

The red line indicates sensitivity profile from the PPC technique using an optimized frequency modulation (OFM) waveform [6, 38], which belongs to the non-linear frequency modulated (NLFM) waveform family. The baseband representation, frequency function, and ambiguity function of the OFM waveform are shown in Figure 3.6. The black dashed line indicates a hypothetical radar sensitivity of the 67- $\mu$ s OFM pulse configuration with no blind range (ideal PC when received signals can be isolated from the leak-through). The yellow line indicates the radar sensitivity of the TFM with a 67- $\mu$ s OFM waveform and a 2- $\mu$ s fill pulse.

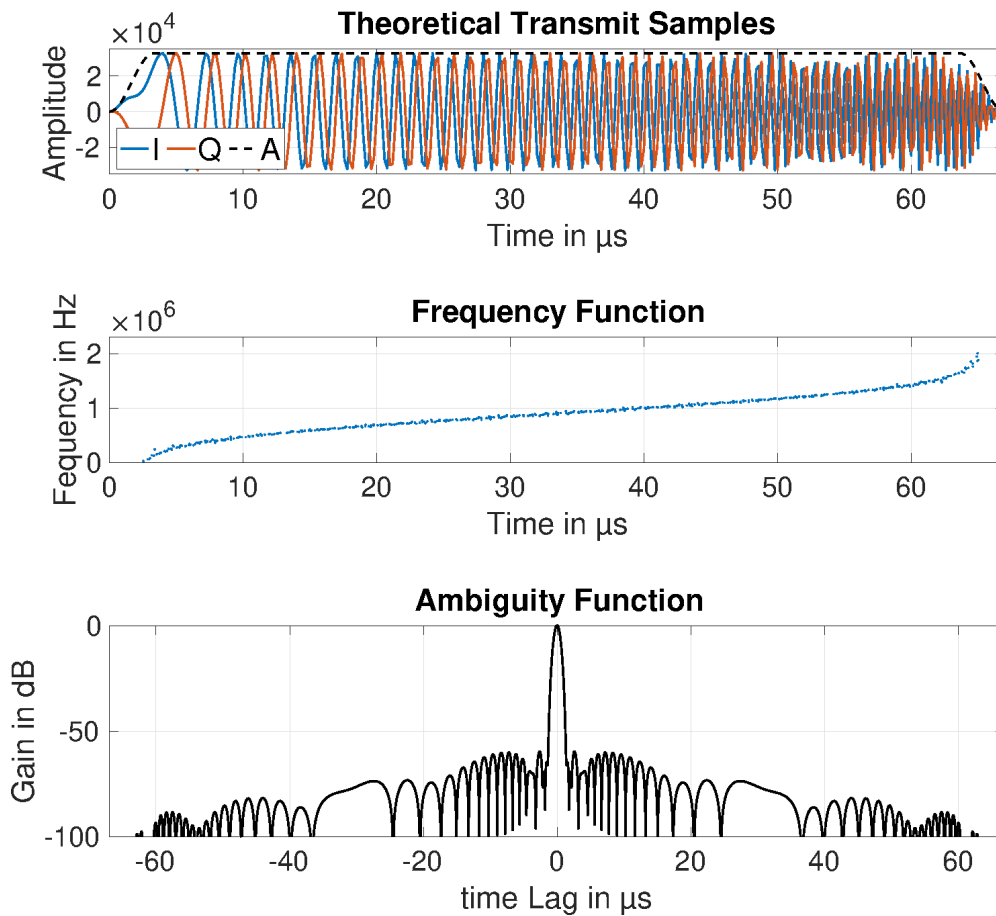


Figure 3.6: Waveform used for PPC experiments. A non-linear frequency modulated waveform has been selected, designed and optimized for the PX-1000 [6, 38]. Only the long pulse is used since the PPC technique requires no fill pulse.

The PPC technique provides comparable sensitivity as the CASA-like radar system. The sensitivity profile obtained using the PPC technique has a gradual degradation inside the blind range. It can be noted that the PPC technique has a slightly poorer sensitivity at close range compared to the 5 kW system.

### 3.2.2 Limitations of PPC

The limitations of the PPC depend on the transmit waveform. Two different waveforms are analyzed here. One is the OFM waveform and the other is a linear frequency modu-

lated (LFM) waveform, which has  $\tau = 67 \mu\text{s}$  and 2.2 MHz of bandwidth. The baseband representation, frequency function, and ambiguity function of the LFM waveform are shown in Figure 3.7. As expected, the range resolution and ambiguity function of the LFM are slightly different than respective counterparts of the OFM waveform.

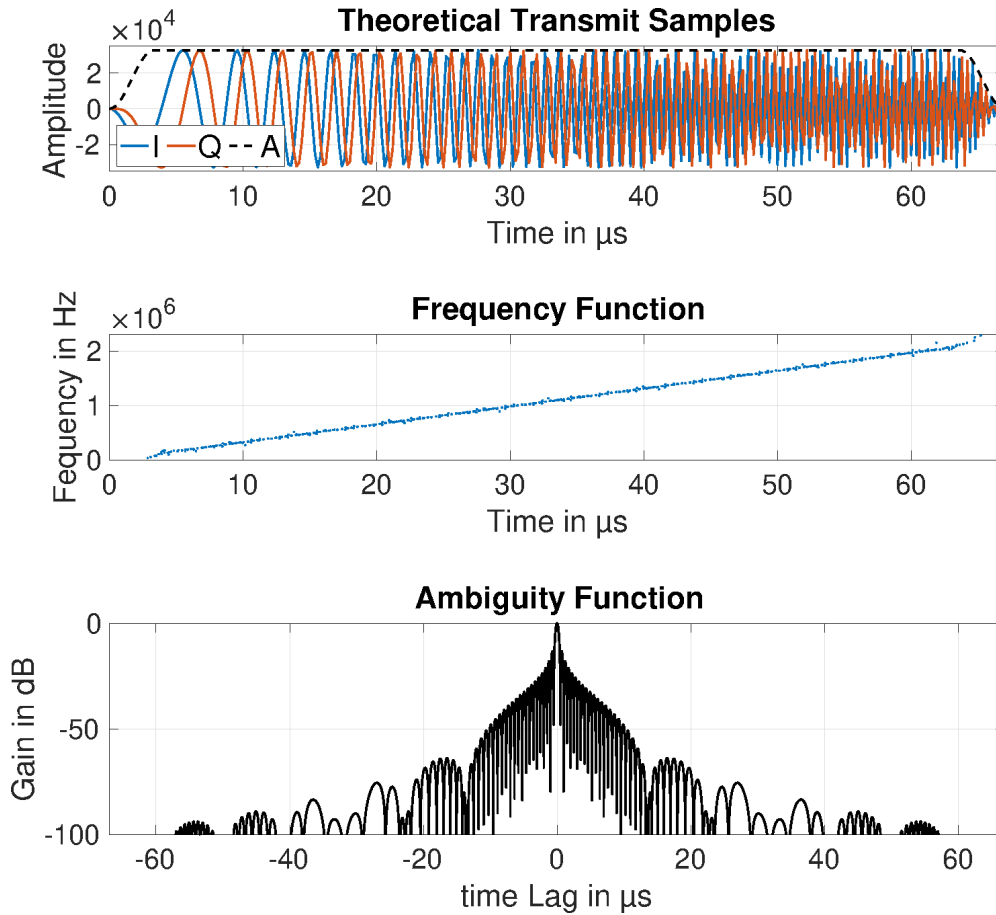


Figure 3.7: Similar to Figure 3.6 but for the designed linear frequency modulated waveform.

Generally, pulse compression increases range resolution and radar sensitivity. The range resolution can be attributed to the effective bandwidth of the waveform. In the partial decoding process (used on PPC), parts of the received signal are zeroed out, using only the uncontaminated tail portion. The original long pulse has been frequency modulated with a specific bandwidth to provide a targeted range resolution. However,

the uncontaminated tail portion inside the blind range has a fraction of such bandwidth, which changes as a range function. Recall from Equation (2.23) that the range resolution is inversely proportional to bandwidth. The progressive reduction of the remaining bandwidth reduces the range resolution of the PPC inside the blind range as  $R$  decreases.

The range resolution of the OFM waveform using the PPC technique in the recovered blind range is shown in Figure 3.8. For the complete pulse ( $\tau = 67 \mu\text{s}$ ), the bandwidth of the waveform is 2.2 MHz producing a range resolution of approximately 60 meters. The results obtained when the LFM is transmitted are presented in Figure 3.9.

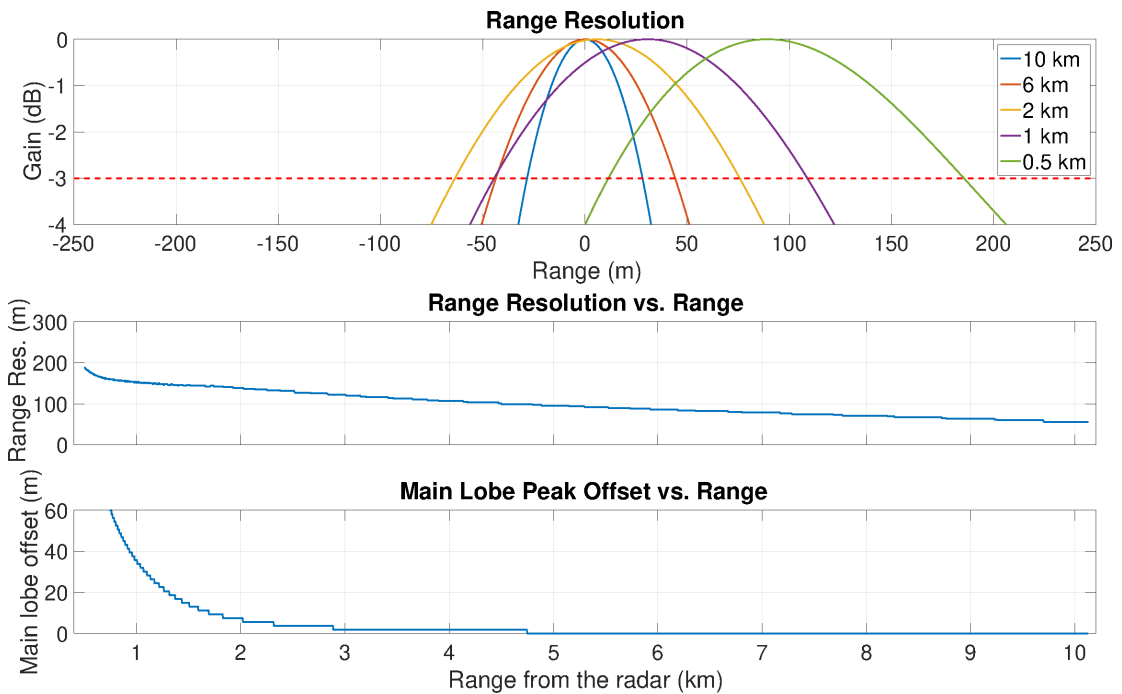


Figure 3.8: Various waveform behaviors of the PPC technique. The waveform ambiguity function at various ranges are shown in the top panel, where the loss of range resolution from closer targets is apparent. In addition, there is a range shift of the peaks. The middle and bottom panels show the shift of the peak and reduction of range resolution, respectively, as a function of range.

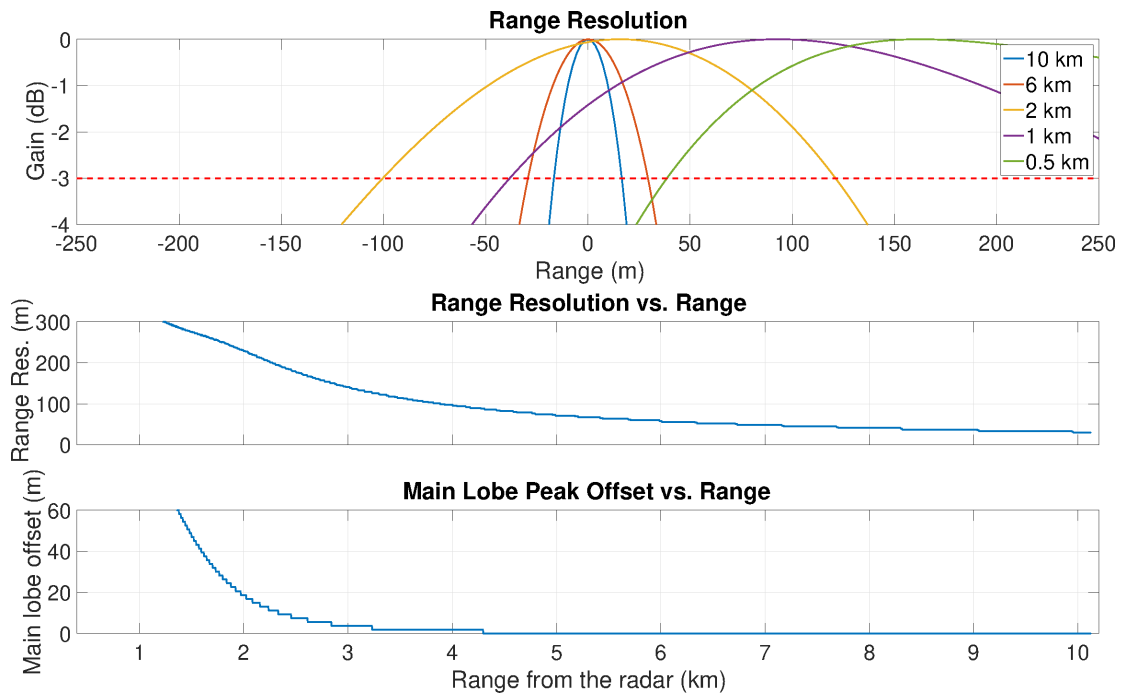


Figure 3.9: Similar to Figure 3.8 but from a 2.2-MHz LFM waveform.

In the upper plot of Figures 3.8 and 3.9, the impulse response of a few point targets located inside the blind range is shown. The upper plot illustrates the loss of range resolution as the range decreases.

The range resolution as a function of the range is numerically quantified in the middle plot of Figures 3.8 and 3.9. It is observed in these plots that the range resolution decreases as the range decreases. The change in range resolution as a range function follows a non-linear behavior (mainly in the first kilometers), especially noticeable when using an LFM.

It is theorized that the non-linearity of the function is caused by the modulation of the partially decoded tail portion. The “matched filter” and the tail portion have different frequency content and center frequency. Moreover, the “matched filter” has a different length and tapering (the received signal is multiplied by a window). This difference in frequency and amplitude affects the cross-correlation product between

them.

The difference in frequency and amplitude content also affects the main lobe position (see the lower plot in Figures 3.8 and 3.9). The second drawback of PPC.

Finally, the cross-correlation of the “matched filter” of the tail portion results in poorer range sidelobe levels for targets inside the blind range. This is illustrated in Figures 3.10 and 3.11. From Figures 3.10 and 3.11, it can be seen that the sidelobe levels are not symmetrical (low toward the radar and high away from it), which can be attributed to the non-symmetrical frequency chirp of the remaining pulse. From Figures 3.10 and 3.11, one can see the “shoulders” of the main lobe, effectively result in a pointer to appear elongated.

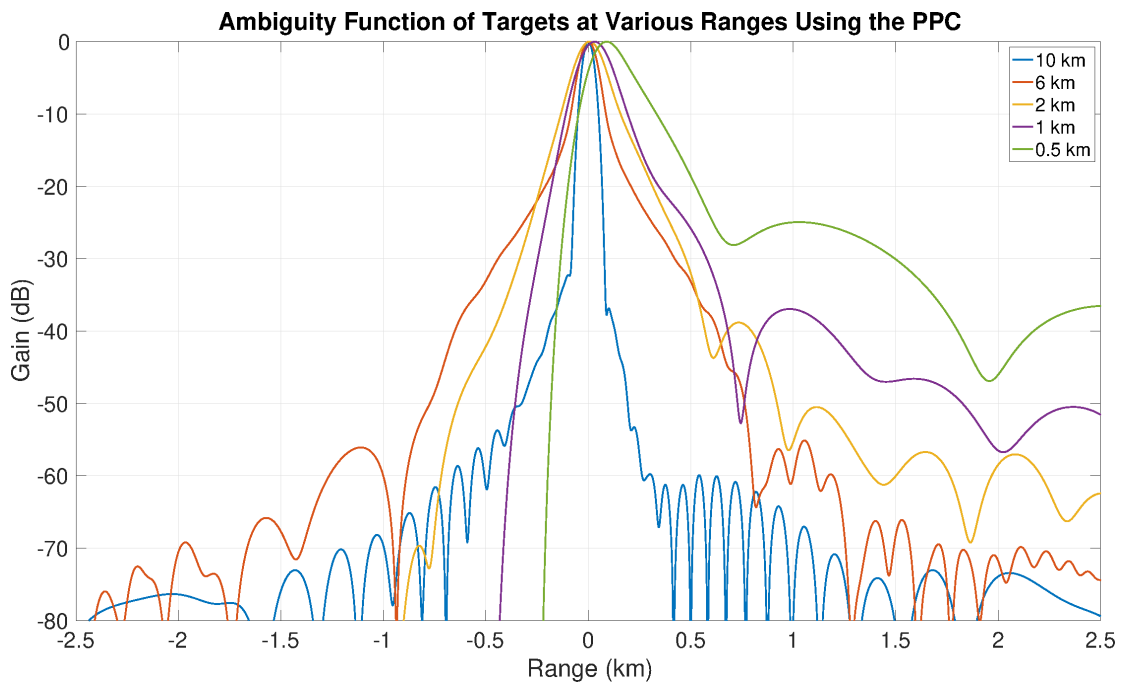


Figure 3.10: Similar to the top panel of Figure 3.8 but with a larger range of y-axis, which represents gain. Besides the main lobe, the range sidelobe levels also vary depending on the target range.



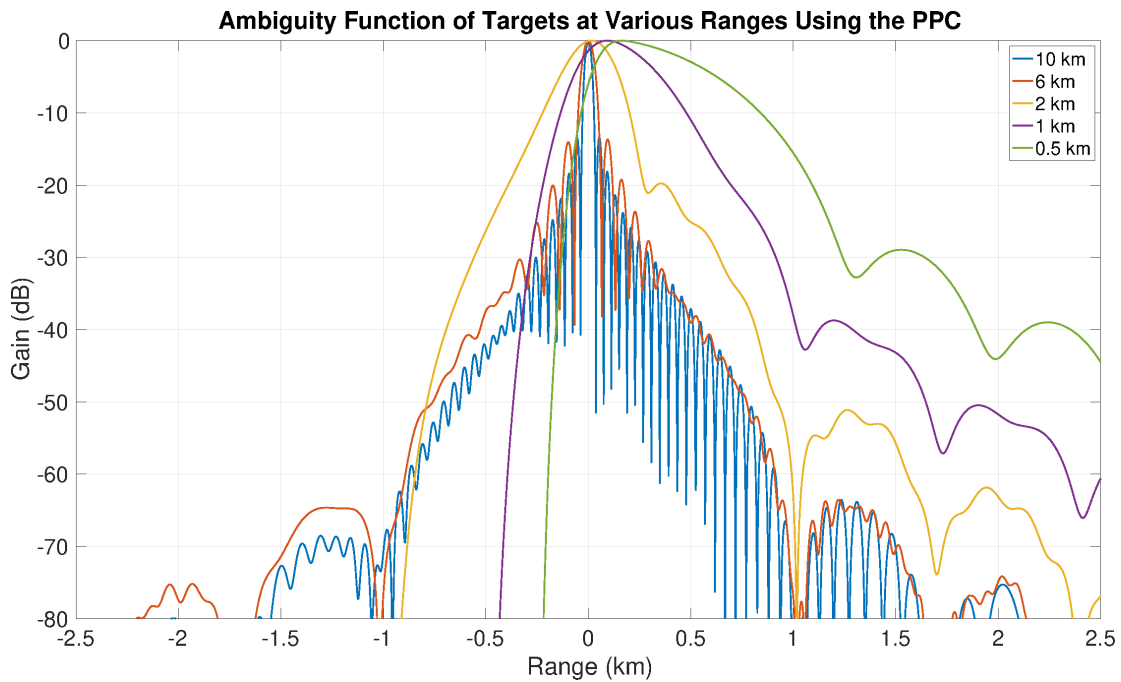


Figure 3.11: Similar to Figure 3.10 but using a 2.2-MHz LFM waveform.

In Figures 3.10 and 3.11 the ambiguity function from simulated targets located at different ranges is shown. Figures 3.10 and 3.11 are similar to the upper plot in Figures 3.8 and 3.11, but showing the sidelobe levels.

In Chapter 5, the author will revisit these three drawbacks and discuss a mitigation strategy.

### 3.3 Results

In this section, PPC performance will be evaluated using both simulation and experimental results. The simulation results compare the performance of PPC against LPC. In the experimental results, PPC was tested using real data from PX-1000, and its performance was compared against TFM (also implemented in PX-1000).

### 3.3.1 Simulation Results

A realistic simulation was undertaken to study the potential performance of two waveforms, i.e., OFM and LFM. They are shown in Figures 3.6 (OFM) and 3.7 (LFM).

Four point targets are simulated. Two are located inside the blind range (approximately 10 km with  $\tau = 67 \mu\text{s}$ ) and the others are outside the blind range. The leak-through is simply a power-altered and phased-shifted copy of the transmitted waveform, similar to the leakage in the PX-1000. A realistic noise level was added.

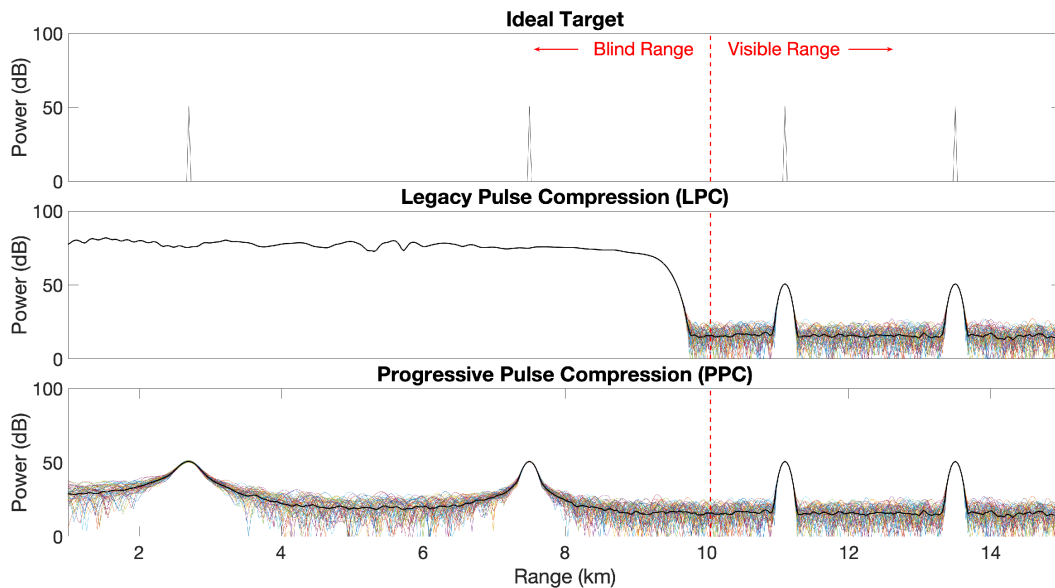


Figure 3.12: Simulation setup and results, transmitting the OFM waveform. In the middle plot are presented the simulation results from the LPC. Similar results are shown on the lower plot but from the PPC. The simulation demonstrates that when processed using the LPC, the targets inside the blind range are obscured by the leak-through. In contrast, the targets are visible when using the PPC.

In Figures 3.12 and 3.13 there is shown in both the simulation setup and return-power profile from the LPC and the PPC techniques but transmit different waveforms. The top panel shows the target locations. When the received signal is processed using the LPC, as shown in the middle plot, two of the four targets are fully obscured (the targets inside the blind range). The bottom panel shows results processed using the

PPC, and the two previously covered targets are now visible.

The subplots on Figures 3.12 and 3.13 are divided (in range) into two regions, the visible range and the blind range. In the visible range, the results from both LPC and PPC are alike. Targets show the same peak power and resolution, and the noise levels of both plots are identical.

In Section 3.1 it was explained that the PPC technique eliminates the uncontaminated signal using a window function. Nevertheless, the window does not modify the received signal from targets located over 10 km (end of the blind range).

Consequently, outside the blind range, the PPC algorithm performs the same as LPC. Additionally, techniques using fill pulse for blind range mitigation also use the long pulse as a “matched filter” in the visible range [42–44], performing similarly to LPC and PPC.

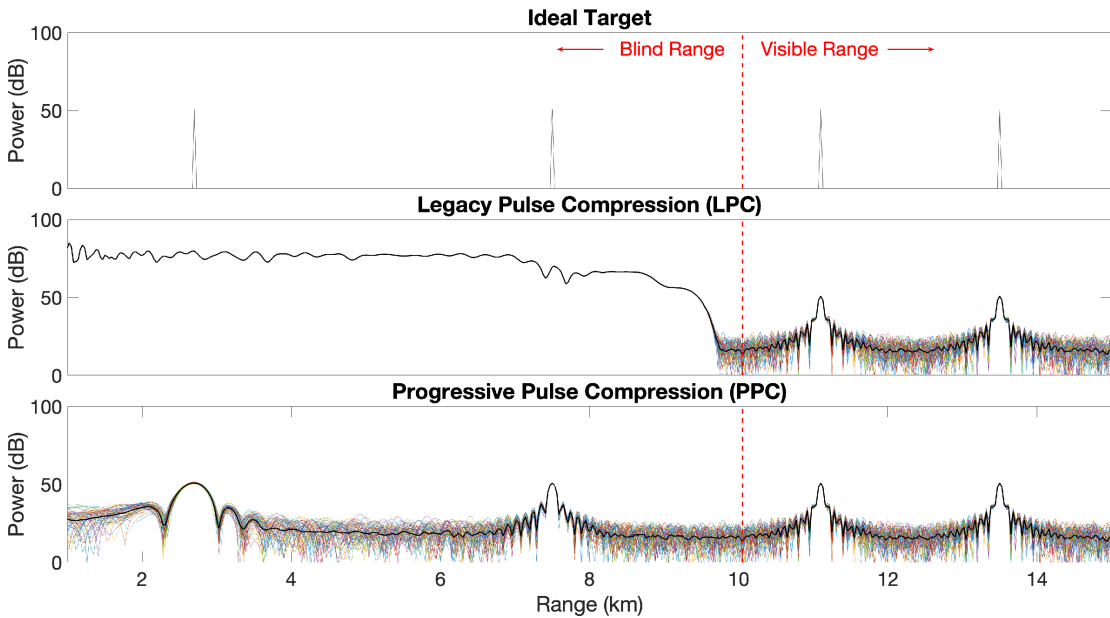


Figure 3.13: Similar to Figure 3.12 but for the designed LFM waveform.

Inside the blind range, LPC suffers from the strong leak-through, which obscures the targets. In contrast, the PPC can correctly estimate the two targets. However, the

loss in range resolution is noticeable, especially on the target closer to the radar.

As explained in Section 3.2.2, the range resolution is lower closer to the radar, as the leftover tail portion is shorter. This effect is manifested as wider targets being produced closer to the radar. In addition, the main lobe peak is slightly shifted, and the sidelobes structure is modified (“shoulder” effect). With respect to the target gain, it can be estimated as expected with the calculated PPC calibration.

### 3.3.2 Experimental Results

#### PPC vs TFM

In this section, the blind range mitigation capabilities of PPC are tested using real data. The PPC technique has been implemented on the PX-1000 radar system and is currently in use on that system (The real data imagery is available through a web portal at <https://radarhub.arrc.ou.edu>). Results in this section are processed using raw data from this system. The radar is transmitting a  $67 \mu\text{s}$  similar to the OFM.

The PPC technique is compared to another blind range mitigation technique referred to as the TFM (using a  $2 \mu\text{s}$  fill pulse) [44]. The advantages of PPC over TFM are described in this section.

The dataset was collected on September 14, 2014, 22:33:13 UTC at an elevation angle of  $3^\circ$ . The dataset has a moderate precipitation spanning approximately 15-km of the north half of the radar coverage. The weather signals span both the visible range and the blind range.

A subset of radar products are calculated from the selected dataset. They include the SNR, reflectivity factor ( $Z$ ), and radial velocity ( $v_r$ ), which are presented in Figure 3.14, and differential reflectivity ( $Z_{DR}$ ), differential phase ( $\Phi_{DP}$ ), and correlation coefficient ( $\rho_{HV}$ ), which are presented in Figure 3.15.

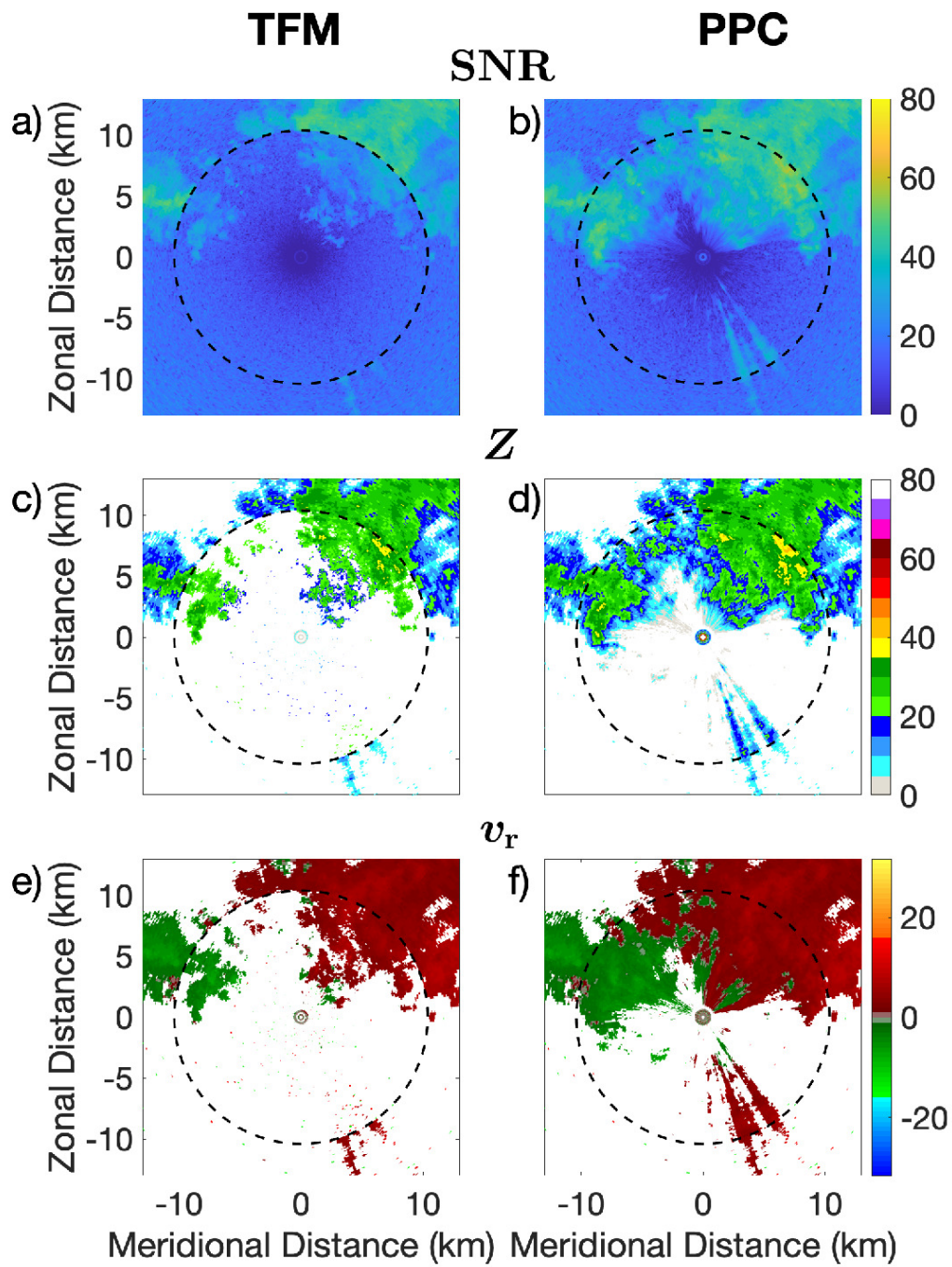


Figure 3.14: Products processed using TFM: a) SNR, c)  $Z$ , e)  $v_r$ . Products processed using PPC: b) SNR, d)  $Z$ , f)  $v_r$ . In these plots it is shown that radar sensitivity is higher inside the blind range on PPC and that the discontinuity in sensitivity has been eliminated.

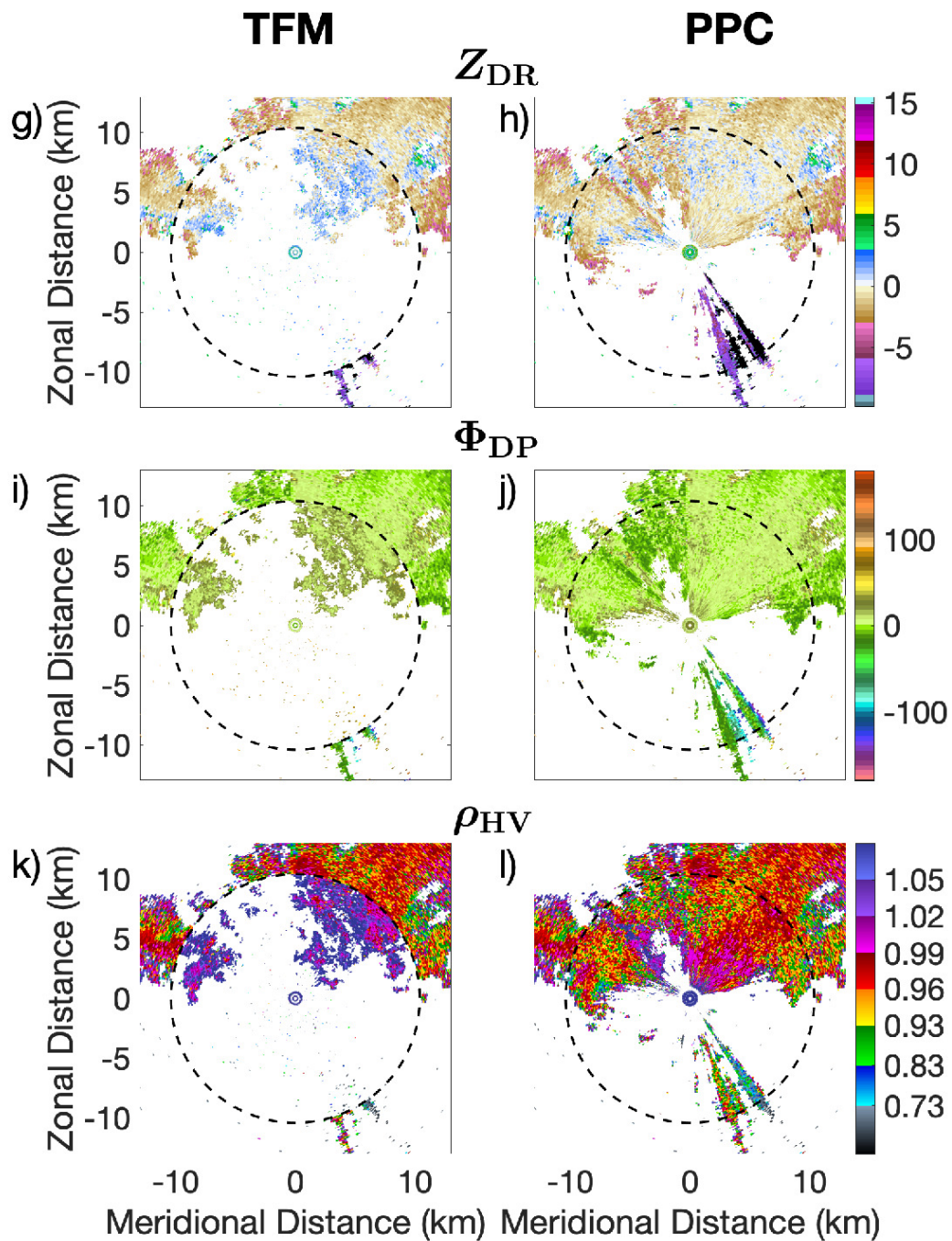


Figure 3.15: Products processed using TFM: g)  $Z_{DR}$ , i)  $\Phi_{DP}$ , k)  $\rho_{HV}$ . Products processed using PPC: h)  $Z_{DR}$ , j)  $\Phi_{DP}$ , l)  $\rho_{HV}$ . The spatial continuity is carried through the polarimetric variables as well.

From Figure 3.14, in the  $Z$  subplot processed with TFM (see Figure 3.14), there

is a jump in sensitivity at the transition between the blind range and the visible range (black dashed circle), which was previously described in Section 3.2.1. On TFM, radar sensitivity is considerably improved (lower) inside the blind range. This increase in sensitivity extends the radar coverage of all radar products.

The main advantage of the PPC compared to the TFM and other fill-pulse mitigation techniques [42–44] is the sensitivity improvement inside the blind range. The PPC has a continuous sensitivity across all ranges. However, there is a loss in range resolution of weather signals closer to the radar. Because of the sensitivity improvement, more weather signals can be observed inside the blind range, especially at the northern portion of the PPI plot, approximately 8 km away from the radar.

Besides the improvements in  $Z$ , all other radar products, i.e., ( $Z_{DR}$ ,  $\Phi_{DP}$  and  $\rho_{HV}$ ), also exhibit similar sensitivity improvement and spatial continuity on PPC when compared to TFM.

In Figure 3.16, it is shown the minimum detectable reflectivity factor ( $Z_{min}$ ) values from the TFM and PPC techniques as a function of range (using the same dataset). The ( $Z_{min}$ ) value corresponds to the minimum ( $Z$ ) from all radials. This calculation is a proxy to estimate the radar sensitivity.

Experimental results from the estimated radar sensitivity values are in agreement with the sensitivity values obtained from the simulation. The improved sensitivity inside the blind range using the PPC technique compared to the TFM technique is approximately 15 dB. This can be attributed to the increase in the usable pulse width  $\tau_u$  as  $R$  increases, indicated by Equation (3.9).

Compared to the TFM technique (which uses a fill pulse with a  $\tau$  of 2  $\mu$ s), the radar sensitivity of the PPC technique is higher as long as  $\tau_u \gtrsim 2 \mu$ s, or equivalently,  $R \gtrsim 300$  m.

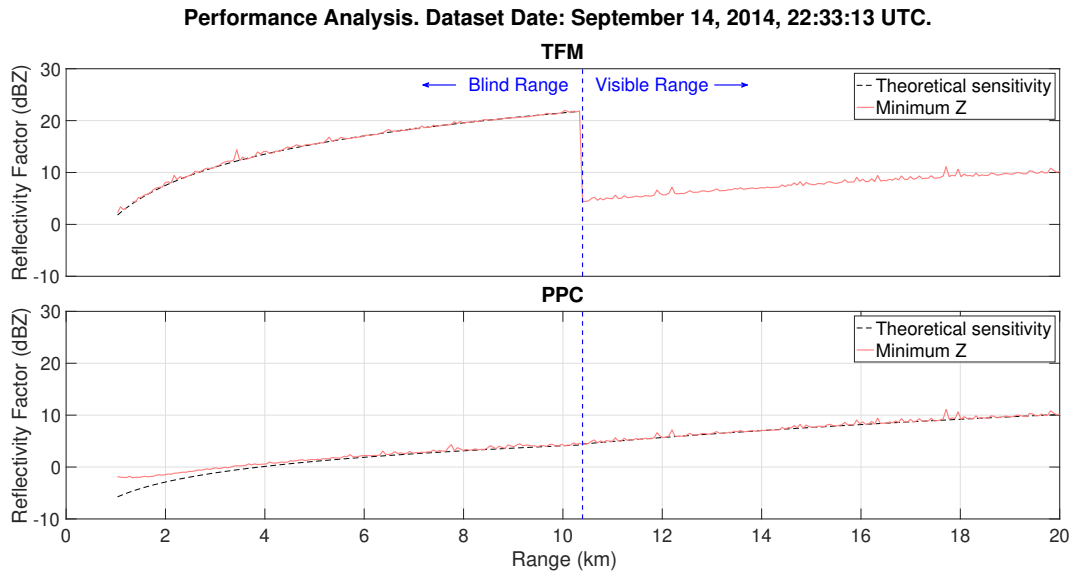


Figure 3.16: Estimated radar sensitivity using the TFM (top) and PPC (bottom) techniques from the dataset collected on September 14, 2014, 22:33:13 UTC. They are obtained by finding the minimum detectable reflectivity factor values from a collection of radials.

### 3.4 Summary

In Chapter 3, a novel technique to mitigate the so-called blind range was proposed. It is called PPC and is intended for radars using pulse compression. The radars can be based on reflector or phased array antennas.

The PPC technique uses a portion of the uncontaminated received signal in conjunction with pulse compression to estimate the echoes inside the blind range. The technique does not require a fill pulse or hardware modifications.

This technique has been tested and validated using the PX-1000 radar. Also, it will be implemented on most ARRC radars that use pulse compression, which include the Horus radar system [26, 33, 34].

All experimental results presented in Chapter 3 are obtained using data collected by



the PX-1000 radar system.

In the next chapter, it is presented a signal processing technique (XPC) to mitigate the cross-polar contamination problem on polarimetric phased array radars.

## **Chapter 4**

### **Cross-Polar Canceler Technique**

As explained in Section 2.3.5, cross-polar contamination is a leakage from the intended polarization into the other polarization. This leakage distorts the information received in the intended copolarization channel and is therefore undesirable.

The technique presented in this chapter, called Cross-Polar Canceler (XPC), is a signal-processing approach to mitigate cross-polar contamination [47, 49]. It is targeted for all-digital phased array radars under STSR mode. Therefore, it is adequate for polarimetric weather measurements as this mode is most traditionally adopted for weather observations worldwide.

The XPC technique will be implemented on the Horus radar system [26, 33, 34]. The S-Band mobile polarimetric all-digital Horus radar system is being developed by the ARRC, at OU, with funding from NOAA.

#### **4.1 Methodology**

The XPC technique takes advantage of the element-level control of the signals transmitted by an all-digital phased array antenna. XPC pre-configures a small group of elements (canceler elements) to transmit signals in the cross-polarization to reduce contamination. The canceler elements transmit the inverse (i.e., the mathematical negative)

of the original waveform scaled by a complex weight. After integrating the fields radiated by all elements, this inverse waveform will suppress the contamination. Depending on the characteristics and power of the cross-polar contamination, XPC tunes the number of canceler elements and their magnitude and phase to cancel the contamination properly. The concept is illustrated in Figure 4.1

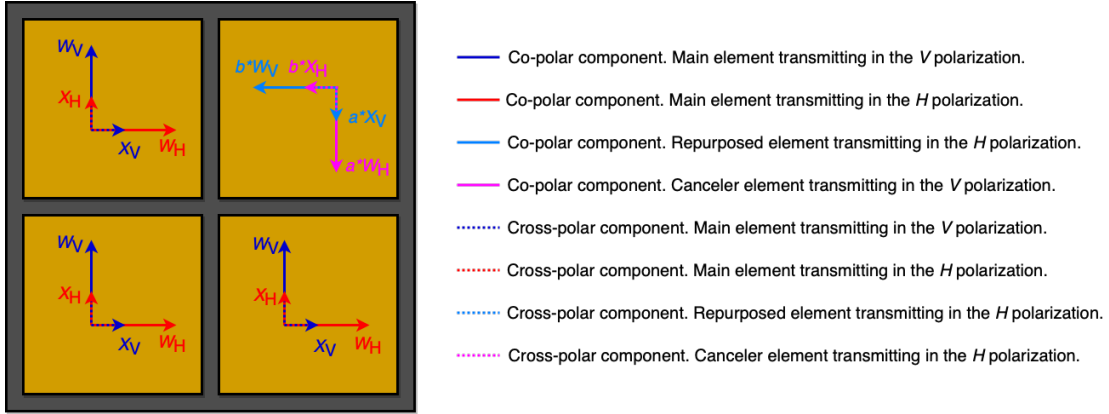


Figure 4.1: Illustration of the XPC concept in a  $2 \times 2$  array transmitting in  $H$  and  $V$  polarizations. The copolar patterns are shown as red and blue solid lines. The cross-polar pattern of each element is illustrated as red and blue dashed lines. One canceler element is necessary to mitigate cross-polar contamination on that particular array. In the perpendicular polarization, the canceler element transmits an amplitude and phase scaled version of the original waveform (the complex scaling factors are defined as  $a$  and  $b$ ). The canceler waveform is transmitted opposite the cross-polar pattern (cyan and magenta solid lines). In addition, the canceler element produces some cross-polarization in the intended polarization (dashed cyan and magenta lines).

In Figure 4.1, it is observed a  $2 \times 2$  dual-polarimetric phased array antenna (STSR mode). Each element on the array transmits a waveform in the  $H$  and  $V$  channels,  $W_H$  and  $W_V$  (blue and red solid lines). Additionally, on the perpendicular channels, the cross-polar contamination is leaked ( $X_H$  and  $X_V$ , represented as the blue and red dashed lines). To mitigate the cross-polar contamination, a percentage of the elements (one element in this example) is set as a canceler. The waveforms transmitted by the cancelers are represented as Cyan and Magenta solid lines. These waveforms are scaled

by the complex scaling factor  $a$  and  $b$ . The waveforms transmitted in the canceler elements also produced a cross-polar contamination component (see dashed cyan and magenta lines).

XPC is an iterative process, calculating the number of canceler elements, amplitude, and phase that mitigate the cross-polar contamination at each steering angle within a scanning region. In each steering angle, the calculation of the number of canceler elements and scaling factor are performed using the echo voltage equation for STSR mode (see (2.68) and (2.69)). The calculations of XPC are based on the assumption that the waveform transmitted on the  $H$  and  $V$  channels are equal,  $W_H = W_V$ . However, the array factors  $F$  are different due to diffraction and fabrication.

It is assumed that perfectly spherical raindrops are observed in the resolution volume. Then  $s_{HH} = s_{VV} = 1$ . Further, without loss of generality it is assumed that  $\phi_{DP} = 0$ ,  $\beta = 0$  and  $C$  is normalized to unity.

After implementing the previous assumptions, Equations (2.72), (2.73) and (2.74) are rewritten as,

$$\begin{bmatrix} V_{H(\text{co})}(R_s, m) \\ V_{V(\text{co})}(R_s, m) \end{bmatrix} = \exp(-j2kR_s(m)) \begin{bmatrix} F_{HH}^2 \\ F_{VV}^2 \end{bmatrix}, \quad (4.1)$$

$$V_{H(\text{cross})}(R_s, m) = \exp(-j2kR_s(m)) \{ F_{HH}F_{HV} + F_{VH}^2 + F_{VH}F_{VV} \} \quad (4.2)$$

and

$$V_{V(\text{cross})}(R_s, m) = \exp(-j2kR_s(m)) \{ F_{HV}F_{HH} + F_{HV}^2 + F_{VH}F_{VV} \}. \quad (4.3)$$

The array factor ( $F_{HV}$ ,  $F_{HV}$ ,  $F_{VH}$ ,  $F_{VV}$ ) and in consequence the echo voltage components ( $V_{H(\text{co})}(R_s, m)$ ,  $V_{H(\text{cross})}(R_s, m)$ ,  $V_{V(\text{co})}(R_s, m)$ ,  $V_{V(\text{cross})}(R_s, m)$ ) are evaluated

at the steering angle.

XPC divides the array into main sub-array and canceler elements sub-array. Then, for an array that transmits/receives a waveform in  $H$  ( $F_{HH}$ ), its cross-polar component is observed in  $V$  ( $F_{VH}$ ). The canceler sub-array transmits/receives in  $V$  the original waveform scaled by  $b$  ( $-bF_{VV2}$ ) and in the opposite direction. The rest of the elements transmit in the same intended polarization (main elements sub-array) but produce a different array factor ( $F_{HH1}$  and  $F_{VH1}$ ). Moreover, the canceler sub-array produces a cross-polar component in  $H$  ( $-bF_{HV2}$ ). Thus, implementing XPC modifies the array factors to

$$\begin{aligned} F_{HH} &= F_{HH1} - bF_{HV2} \\ F_{VH} &= F_{VH1} - bF_{VV2}. \end{aligned} \quad (4.4)$$

Similarly, the co- and cross-polar factors for the array transmitting in the  $V$  polarization are presented in (4.5).

$$\begin{aligned} F_{HV} &= F_{HV1} - aF_{HH2} \\ F_{VV} &= F_{VV1} - aF_{VH2}, \end{aligned} \quad (4.5)$$

where  $a$  is the scaling factor use to mitigate the cross-polar component observed in the  $H$  polarization. Equations (4.4) and (4.5) are replaced in (4.1), (4.2) and (4.3).

$$\begin{bmatrix} V_{H(\text{co})}(R_s, m) \\ V_{V(\text{co})}(R_s, m) \end{bmatrix} = \exp(-j2kR_s(m)) \begin{bmatrix} (F_{HH1} - bF_{HV2})^2 \\ (F_{VV1} - aF_{VH2})^2 \end{bmatrix} \quad (4.6)$$

$$V_{H(\text{cross})}(R_s, m) = \exp(-j2kR_s(m))\{(F_{HH1} - bF_{HV2})(F_{HV1} - aF_{HH2}) \\ + (F_{VH1} - bF_{VV2})^2 + (F_{VH1} - bF_{VV2})(F_{VV1} - aF_{VH2})\} \quad (4.7)$$

$$V_{V(\text{cross})}(R_s, m) = \exp(-j2kR_s(m))\{(F_{HV1} - aF_{HH2})(F_{HH1} - bF_{HV2}) \\ + (F_{HV1} - aF_{HH2})^2 + (F_{VH1} - bF_{VV2})(F_{VV1} - aF_{VH2})\} \quad (4.8)$$

It is expected that, if the number of canceler elements and the scaling factors are correctly calculated,  $V_{H(\text{cross})}(R_s, m)$  and  $V_{V(\text{cross})}(R_s, m)$  will be mitigated. The calculation of the number of canceler elements and the scaling factor is derived in the next section.

#### 4.1.1 Number and Location of Canceler Elements

The first step of the XPC technique is calculating the number of canceler elements. Correctly estimating the number of canceler elements is a first approximation to mitigate the cross-polar contamination.

Some assumptions are made to calculate the number of canceler elements. The first assumption is that the scaling factors ( $a$  and  $b$ ) are simplified as a real value (1). A second assumption is that the element patterns are equal in all elements. Finally, a third assumption is that perfect isolation of the cross-polar components is achieved. Thus,  $V_{H(\text{cross})}(R_s, m) = V_{V(\text{cross})}(R_s, m) = 0$ . Then,

$$0 = \exp(-j2kR_s(m))\{(F_{HH1} - F_{HV2})(F_{HV1} - F_{HH2}) \\ + (F_{VH1} - F_{VV2})^2 + (F_{VH1} - F_{VV2})(F_{VV1} - F_{VH2})\} \quad (4.9)$$

and

$$0 = \exp(-j2kR_s(m))\{(F_{HV1} - F_{HH2})(F_{HH1} - F_{HV2}) + (F_{HV1} - F_{HH2})^2 + (F_{VH1} - F_{VV2})(F_{VV1} - F_{VH2})\}. \quad (4.10)$$

The phase term ( $\exp(-j2kR_s(m))$ ) is different than zero, thus

$$0 = (F_{HH1} - F_{HV2})(F_{HV1} - F_{HH2}) + (F_{VH1} - F_{VV2})^2 + (F_{VH1} - F_{VV2})(F_{VV1} - F_{VH2}) \quad (4.11)$$

and

$$0 = (F_{HV1} - F_{HH2})(F_{HH1} - F_{HV2}) + (F_{HV1} - F_{HH2})^2 + (F_{VH1} - F_{VV2})(F_{VV1} - F_{VH2}). \quad (4.12)$$

The quadratic term in Equations (4.11) and (4.12) ( $(F_{VH1} - F_{VV2})^2$  and  $(F_{HV1} - F_{HH2})^2$ ) are considerably smaller with respect to the other terms, therefore they are approximated as zero and removed from the equations. After this simplification, Equations (4.11) and (4.12) are equal (see Equation (4.13)).

$$0 = (F_{HV1} - F_{HH2})(F_{HH1} - F_{HV2}) + (F_{VH1} - F_{VV2})(F_{VV1} - F_{VH2}) \quad (4.13)$$

The main and canceler co- and cross-patterns can be expressed as a function of the co- and cross-patterns of the entire array, from the second assumption (see Equations (4.14) and (4.15)).

$$\begin{aligned}
F_{\text{HH}1} &= \frac{eF_{\text{HH}}}{w} \\
F_{\text{HV}1} &= \frac{eF_{\text{HV}}}{w} \\
F_{\text{VH}1} &= \frac{eF_{\text{VH}}}{w} \\
F_{\text{VV}1} &= \frac{eF_{\text{VV}}}{w}
\end{aligned} \tag{4.14}$$

$$\begin{aligned}
F_{\text{HH}2} &= \frac{hF_{\text{HH}}}{w} \\
F_{\text{HV}2} &= \frac{hF_{\text{HV}}}{w} \\
F_{\text{VH}2} &= \frac{hF_{\text{VH}}}{w} \\
F_{\text{VV}2} &= \frac{hF_{\text{VV}}}{w},
\end{aligned} \tag{4.15}$$

where  $w$  is the total number of elements in the array. Out of the  $w$  elements,  $e$  are main elements and  $h$  are canceler elements.

$$\begin{aligned}
0 = \left( \frac{eF_{\text{HV}}}{w} - \frac{hF_{\text{HH}}}{w} \right) \left( \frac{eF_{\text{HH}}}{w} - \frac{hF_{\text{HV}}}{w} \right) \\
+ \left( \frac{eF_{\text{VH}}}{w} - \frac{hF_{\text{VV}}}{w} \right) \left( \frac{eF_{\text{VV}}}{w} - \frac{hF_{\text{VH}}}{w} \right)
\end{aligned} \tag{4.16}$$

$$\begin{aligned}
0 = \frac{e^2 F_{\text{HV}} F_{\text{HH}}}{w^2} - \frac{eh F_{\text{HV}}^2}{w^2} - \frac{eh F_{\text{HH}}^2}{w^2} + \frac{h^2 F_{\text{HV}} F_{\text{HH}}}{w^2} \\
+ \frac{e^2 F_{\text{VH}} F_{\text{VV}}}{w^2} - \frac{eh F_{\text{VH}}^2}{w^2} - \frac{eh F_{\text{VV}}^2}{w^2} + \frac{h^2 F_{\text{VH}} F_{\text{VV}}}{w^2}
\end{aligned} \tag{4.17}$$

The  $w$  value is greater than 0. Therefore, it can be simplified from the equation.



Thus,

$$0 = e^2 F_{\text{HV}} F_{\text{HH}} - eh F_{\text{HV}}^2 - eh F_{\text{HH}}^2 + h^2 F_{\text{HV}} F_{\text{HH}} \\ + e^2 F_{\text{VH}} F_{\text{VV}} - eh F_{\text{VH}}^2 - eh F_{\text{VV}}^2 + h^2 F_{\text{VH}} F_{\text{VH}}. \quad (4.18)$$

Equation (4.18) is rewritten to replace  $e$  in terms of  $h$  ( $e = w - h$ )

$$0 = (w - h)^2 F_{\text{HV}} F_{\text{HH}} - (w - h)h(F_{\text{HV}}^2 + F_{\text{HH}}^2) + h^2 F_{\text{HV}} F_{\text{HH}} \\ + (w - h)^2 F_{\text{VH}} F_{\text{VV}} - (w - h)h(F_{\text{VH}}^2 + F_{\text{VV}}^2) + h^2 F_{\text{VH}} F_{\text{VH}} \quad (4.19)$$

$$0 = (w^2 - 2wh + h^2) F_{\text{HV}} F_{\text{HH}} - (wh - h^2)(F_{\text{HV}}^2 + F_{\text{HH}}^2) + h^2 F_{\text{HV}} F_{\text{HH}} \\ + (w^2 - 2wh + h^2) F_{\text{VH}} F_{\text{VV}} - (wh - h^2)(F_{\text{VH}}^2 + F_{\text{VV}}^2) + h^2 F_{\text{VH}} F_{\text{VH}} \quad (4.20)$$

$$0 = w^2(F_{\text{HV}} F_{\text{HH}} + F_{\text{VH}} F_{\text{VV}}) \\ + wh(-2F_{\text{HV}} F_{\text{HH}} - F_{\text{HV}}^2 - F_{\text{HH}}^2 - 2F_{\text{VH}} F_{\text{VV}} - F_{\text{VH}}^2 - F_{\text{VV}}^2) \\ + h^2(2F_{\text{HV}} F_{\text{HH}} + F_{\text{HV}}^2 + F_{\text{HH}}^2 + 2F_{\text{VH}} F_{\text{VV}} + F_{\text{VH}}^2 + F_{\text{VV}}^2) \quad (4.21)$$

$$0 = w^2(F_{\text{HV}} F_{\text{HH}} + F_{\text{VH}} F_{\text{VV}}) \\ + wh(-(F_{\text{HV}} + F_{\text{HH}})^2 - (F_{\text{VH}} + F_{\text{VV}})^2) \\ + h^2((F_{\text{HV}} + F_{\text{HH}})^2 + (F_{\text{VH}} + F_{\text{VV}})^2). \quad (4.22)$$

Equation (4.22) is rewritten as follows,

$$0 = h^2\alpha_2 + h(-w\alpha_2) + w^2\alpha_1, \quad (4.23)$$

where

$$\begin{aligned} \alpha_1 &= F_{HV}F_{HH} + F_{VH}F_{VV} \\ \alpha_2 &= (F_{HV} + F_{HH})^2 + (F_{VH} + F_{VV})^2. \end{aligned} \quad (4.24)$$

Equation (4.23) is solved using the quadratic formula. Then,

$$h = \frac{w\alpha_2 \pm \sqrt{(-w\alpha_2)^2 - 4\alpha_2w^2\alpha_1}}{2\alpha_2} \quad (4.25)$$

$$h = \frac{w\alpha_2 \pm \sqrt{w^2(\alpha_2^2 - 4\alpha_2\alpha_1)}}{2\alpha_2} \quad (4.26)$$

$$h = \frac{w \pm \sqrt{w^2 \frac{\alpha_2^2 - 4\alpha_2\alpha_1}{\alpha_2^2}}}{2} \quad (4.27)$$

$$h = \frac{w \left( 1 \pm \sqrt{\frac{\alpha_2 - 4\alpha_1}{\alpha_2}} \right)}{2}. \quad (4.28)$$

Replacing  $\alpha_1$  and  $\alpha_2$  inside the square root term,

$$\frac{\alpha_2 - 4\alpha_1}{\alpha_2} = \frac{F_{HH}^2 + F_{VV}^2 + F_{HV}^2 + F_{VH}^2 - 2(F_{HV}F_{HH} + F_{VH}F_{VV})}{F_{HH}^2 + F_{VV}^2 + F_{HV}^2 + F_{VH}^2 + 2(F_{HV}F_{HH} + F_{VH}F_{VV})} \quad (4.29)$$

$$\frac{\alpha_2 - 4\alpha_1}{\alpha_2} = \frac{(F_{HV} - F_{HH})^2 + (F_{VH} - F_{VV})^2}{(F_{HV} + F_{HH})^2 + (F_{VH} + F_{VV})^2}. \quad (4.30)$$

Combining (4.28) and (4.30),

$$h = \frac{w \left( 1 \pm \sqrt{\frac{(F_{HV} - F_{HH})^2 + (F_{VH} - F_{VV})^2}{(F_{HV} + F_{HH})^2 + (F_{VH} + F_{VV})^2}} \right)}{2}. \quad (4.31)$$

The  $h$  expression derived in the previous equation is a complex term. Nevertheless,  $h$  corresponds to the number of canceler elements. Therefore,  $|h|$  is used to estimate the number of canceler elements ( $h = |h|$ ). The new  $h$  expression has two possible solutions. One solution produces an  $h$  larger than half the total number of elements in the array ( $h \geq w/2$ ). Having that many canceler elements will negatively impact the gain of the system. Therefore, the best estimation of the number of canceler elements is

$$h = \left| w/2 \left( 1 - \sqrt{\frac{(F_{HV} - F_{HH})^2 + (F_{VH} - F_{VV})^2}{(F_{HV} + F_{HH})^2 + (F_{VH} + F_{VV})^2}} \right) \right|. \quad (4.32)$$

Concerning the number of canceler elements, the expression in (4.32) is not necessarily an integer value, but it can be a decimal. Thus, if  $h$  is not an integer, it is necessary to round it.

If  $h$  is rounded to the largest integer, it would over estimate the number of canceler elements. Then, to compensate for the rounding effect, the calculated scaling factor will be lower or equal to one, reducing the copolar gain. In contrast, rounding to the lower integer will under estimate the number of cancelers. Thus, the scaling factor will have a value higher or equal to one to compensate for this. A scaling factor higher than one is equivalent to having a transmitter gain, which is not possible. As a result, XPC will always round the calculated number of canceler elements to the largest integer.

The distribution of the canceler elements in the array significantly impacts the per-

formance of XPC. Different locations have been tested to find the best one. The best allocation of canceler is selected by comparing the cross-polar mitigation, sidelobe level performance, and overall performance of XPC in each configuration (optimization algorithm). The experiment concluded that the best location of the canceler elements is often at the edges of the array, especially in the corners. The location of the canceler elements is chosen since they would have a less adverse impact on sidelobes.

### 4.1.2 Calculation of the Scaling Factors

After estimating and distributing the number of canceler elements, they are scaled to optimize the cross-polar mitigation impact. The scaling factor is a complex number, so it changes the amplitude and phase of the canceler elements. A different scaling factor is designed for each polarization ( $a$  and  $b$ ).

The calculation of the scaling factor are based on Equations (4.7) and (4.8). In (4.7) and (4.8), if the scaling factors are correctly tuned,  $V_{V(\text{cross})}(R_s, m) = V_{V(\text{cross})}(R_s, m) = 0$ . Thus,

$$0 = \exp(-j2kR_s(m))\{(F_{HH1} - bF_{HV2})(F_{HV1} - aF_{HH2}) + (F_{VH1} - bF_{VV2})^2 + (F_{VH1} - bF_{VV2})(F_{VV1} - aF_{VH2})\} \quad (4.33)$$

and

$$0 = \exp(-j2kR_s(m))\{(F_{HV1} - aF_{HH2})(F_{HH1} - bF_{HV2}) + (F_{HV1} - aF_{HH2})^2 + (F_{VH1} - bF_{VV2})(F_{VV1} - aF_{VH2})\}. \quad (4.34)$$

As explained in Section 4.1.1 the phase term  $\exp(-j2kR_s(m))$  is different than

zero. Therefore,

$$0 = (F_{HH1} - bF_{HV2})(F_{HV1} - aF_{HH2}) + (F_{VH1} - bF_{VV2})^2 + (F_{VH1} - bF_{VV2})(F_{VV1} - aF_{VH2}) \quad (4.35)$$

and

$$0 = (F_{HV1} - aF_{HH2})(F_{HH1} - bF_{HV2}) + (F_{HV1} - aF_{HH2})^2 + (F_{VH1} - bF_{VV2})(F_{VV1} - aF_{VH2}). \quad (4.36)$$

Both equations are the summation of three terms. Thus, if the result of that summation is zero, a simple solution is that every term in it is also zero. Then,

$$0 = (F_{HH1} - bF_{HV2})(F_{HV1} - aF_{HH2}), \quad (4.37)$$

$$0 = (F_{VH1} - bF_{VV2})(F_{VV1} - aF_{VH2}), \quad (4.38)$$

$$0 = (F_{VH1} - bF_{VV2})^2 \quad (4.39)$$

and

$$0 = (F_{HV1} - aF_{HH2})^2. \quad (4.40)$$

One pair of expressions for  $a$  and  $b$  that solves the four equations (4.37, 4.38, 4.39 and 4.40) simultaneously are presented in Equations (4.41) and (4.42).

$$a = \frac{F_{HV1}}{F_{HH2}} \quad (4.41)$$

$$b = \frac{F_{VH1}}{F_{VV2}} \quad (4.42)$$

In some cases, the derived solution for the scaling factor might produce an  $a$  or  $b$  with a magnitude slightly larger than one. If that is the case, XPC normalizes the magnitude of the scaling factor.

The previous solutions hold not only for STSR, but also for ATSR.

## **4.2 Advantages and Limitations of XPC**

### **4.2.1 XPC Performance with Respect to the Steering Angle**

From Section 4.1, it has been established that the equations to calculate the number of canceler elements and scaling factor are a function of the co- and cross-components of the array pattern in a particular steering location. In a phased array system, the cross-polar contamination increases, and the copolar gain decreases as the beam is steered away from the principal planes. Thus, XPC recalculates the number of canceler elements and the scaling factor to maximize the cross-polar isolation per steering angle. This iterative process is an advantage of this technique compared to other hardware implementations [50].

Concerning the number of canceler elements, it is directly proportional to the co- and cross-polar components of the array pattern in both polarizations (see Equation (4.32)). In the ideal best-case scenario (the cross-polar component is negligible), the expression inside the square root is approximately equal to unity. Thus the number of canceler elements is zero. The number of canceler elements increases as the cross-polar components get larger. Suppose the co- and cross-polar components in each polarization are equal (the expression inside the square root is equal to zero). In that case, the number of canceler elements is half the total number of elements. Nevertheless, this is uncommon. Therefore, as the beam steers away from the principal planes, more canceler elements are necessary to minimize the cross-polar contamination.

Similarly, the scaling factors in both polarizations are directly proportional to the ratio between the cross-polar component on the array pattern of main elements sub-array divided by the copolar component of the one with canceler elements. The higher the fraction, the closer to one they will be.

Different steering locations may have similar co- and cross-polar patterns. Therefore, the same number of canceler elements might be estimated for both (due to rounding). Nevertheless, the scaling factor between them will be different to compensate for rounding. The one with a more significant difference between the co- and cross-polar component will produce a scaling factor closer to one (higher).

#### **4.2.2 Limitations of XPC**

In a phased array radar, The  $H$  and  $V$  element patterns can differ significantly. Then, as the array is steered off the broadside, the beam on the  $H$  and  $V$  array patterns could point in slightly different directions (from each other and the steering angle). This effect will be termed angular mismatch. Additionally, as explained in Chapter 2, phased array radars using phase shifters may suffer from beam squint, producing a similar angular mismatch. In XPC, the number of canceler elements and the scaling factors are calculated based on the co- and cross-polar components or the  $H$  and  $V$  array patterns in the steering position. Therefore, the performance of XPC might suffer due to the angular mismatch effect. Figure 4.2 illustrates this effect.

The array pattern for a simulated  $8 \times 8$  array populated with crossed-dipole elements is provided in Figure 4.2. In the simulation, it was assumed that all elements have the same pattern. The element pattern has been estimated from an infinite-array approach (edge effects not considered). The array is steered  $-38^\circ$  in azimuth and  $18^\circ$  in elevation. Nevertheless, there is an angular mismatch in both the  $H$  and  $V$  patterns. The  $H$

pattern points  $-40^\circ$  in azimuth and  $18^\circ$  in elevation, and  $V$  to  $-38^\circ$  in azimuth and  $18^\circ$  in elevation.

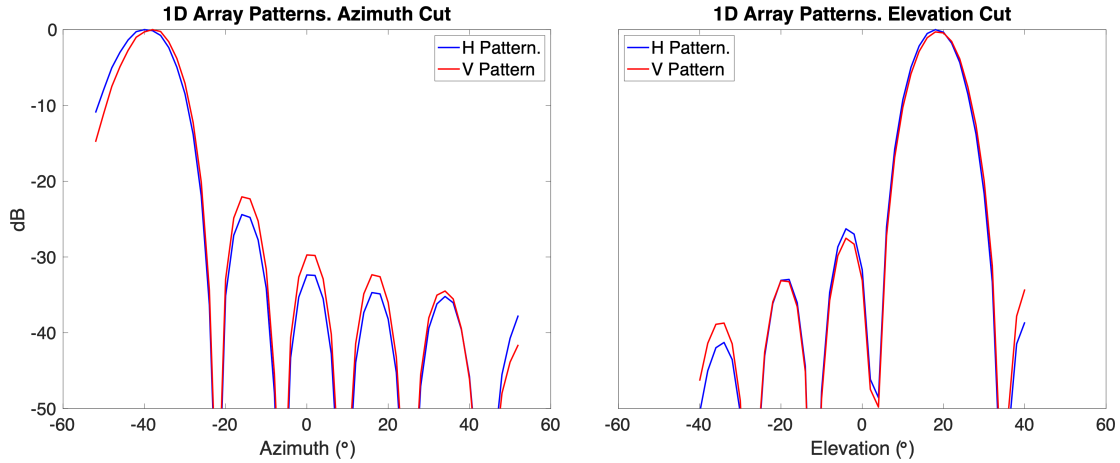


Figure 4.2: Angular mismatch effect of a simulated  $8 \times 8$  array populated with crossed-dipole elements. The array is steered  $-38^\circ$  in azimuth and  $18^\circ$  in elevation. Nevertheless, the  $H$  pattern points  $-40^\circ$  in azimuth and  $18^\circ$  in elevation, and  $V$   $-38^\circ$  in azimuth and  $18^\circ$  in elevation. This change in the beam position is termed angular mismatch.

Nonetheless, the angular mismatch is not noticeable when steering close to the broadside (depending on the angular resolution of the pattern samples). The simulated array shown in Figure 4.2 has an angular resolution of  $2^\circ$  in azimuth and elevation. For example, when the same array is steered  $12^\circ$  in azimuth and  $8^\circ$  in elevation, the angular mismatch effect is unnoticeable ( $H$  and  $V$  patterns point  $12^\circ$  in azimuth and  $8^\circ$  in elevation), as shown in Figure 4.3.



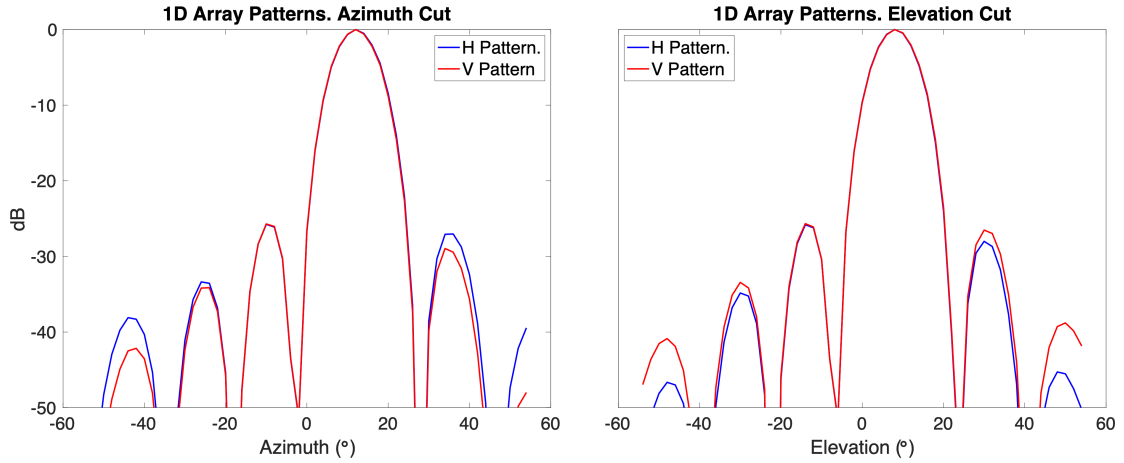


Figure 4.3: Similar to Figure 4.2 but the array is steered to a different position ( $12^\circ$  in azimuth and  $8^\circ$  in elevation). The angular mismatch effect is unnoticeable for an angular resolution of  $2^\circ$  in azimuth and elevation.

XPC has been implemented for the two cases presented before. Results are presented in Figures 4.4 and 4.5. In the case where the angular mismatch is not significant (array steered  $12^\circ$  in azimuth and  $8^\circ$  in elevation), the cross-polar isolation (difference between the co- and cross-polar components) was improved from 30.37 dB in  $H$  and 30.3 dB in  $V$  to 320 dB in  $H$  and  $V$ . The improvement is high enough to reduce the cross-polar component to numerical precision (16 bits). In contrast, when the patterns suffer from the angular mismatch (array steered  $-38^\circ$  in azimuth and  $18^\circ$  in elevation), the cross-polar isolation is improved but less significantly. For that case, the cross-polar isolation was improved from 14.24 dB in  $H$  and 11.41 dB in  $V$  to 48.42 dB in  $H$  and 31.49 dB in  $V$ .

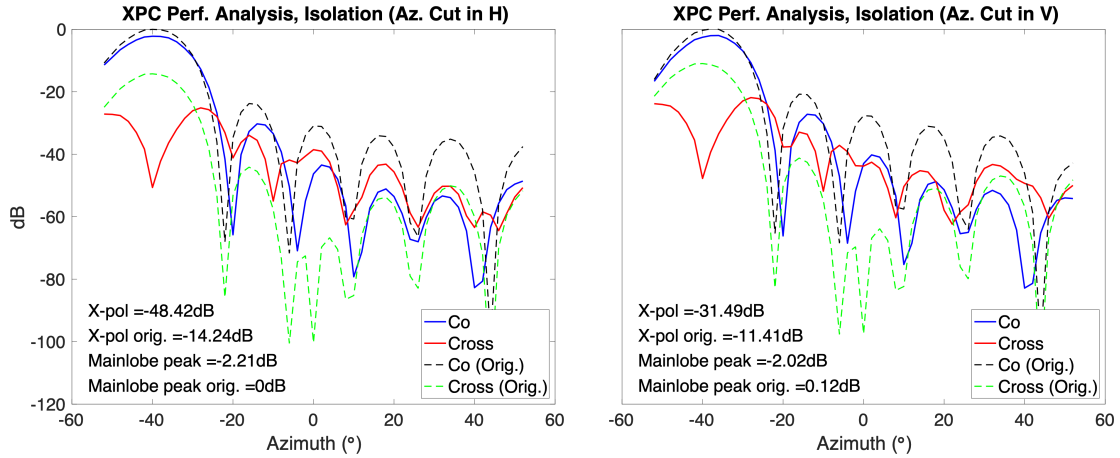


Figure 4.4: XPC was applied on a simulated  $8 \times 8$  array populated with crossed-dipole elements. The array is steered  $-38^\circ$  in azimuth and  $18^\circ$  in elevation. Seven elements have been repurposed as canceler elements. The scaling factors on those elements are  $a = 0.92 + j0.40$  and  $b = 0.67 - j0.29$ . The cross-polar isolation is improved from 14.24 dB in  $H$  and 11.41 dB in  $V$  to 48.42 dB in  $H$  and 31.49 dB in  $V$ .

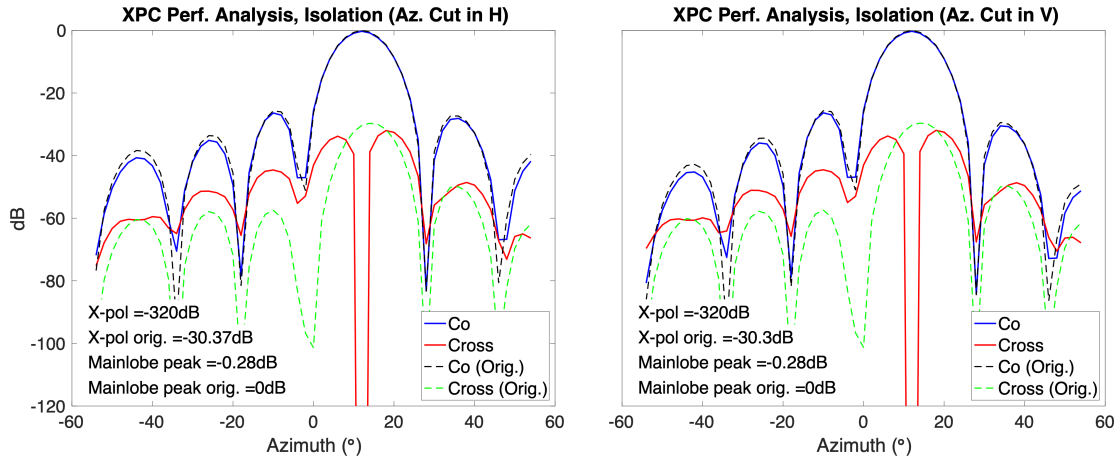


Figure 4.5: XPC was applied on a simulated  $8 \times 8$  array populated with crossed-dipole elements. The array is steered  $12^\circ$  in azimuth and  $8^\circ$  in elevation. One element have been repurposed as canceler elements. The scaling factors on this element are  $a = 0.92 + j0.06$  and  $b = 0.98 + j0.01$ . The cross-polar isolation is improved from 30.37 dB in  $H$  and 30.3 dB in  $V$  to 320 dB in  $H$  and  $V$ .

Additionally, XPC modifies the direction and severity of the angular mismatch as a function of the number of elements repurposed as cancelers and the scaling factor. A calibration algorithm to mitigate the effects of the angular mismatch in the calculation

and implementation of XPC will be developed and discussed in Chapter 5.

Another limitation of XPC is observed in Equation (4.6). Two factors reduce the copolar component (copolar gain) after XPC is implemented. The largest contributor is the reduced number of main elements (changed to canceler elements). The lower the number of elements transmitting in the main polarization, the lower the copolar gain. The second factor is the cross-polar component generated by the canceler elements, slightly reducing the copolar gain. Therefore, The larger the cross-polar contamination, the higher the loss in the copolar gain.

From the examples in Figure 4.4, originally, the cross-polar isolation was 14.24 dB in  $H$  and 11.41 dB in  $V$ . To obtain better cross-polar isolation, seven elements were set as cancelers (the scaling factors are  $a = 0.81 + j0.55$  and  $b = 0.59 - j0.45$ ). Thus, the copolar gain is reduced by roughly 2.21 dB in  $H$  and 2.01 dB in  $V$ . On the contrary, for the examples in Figure 4.4 originally, the cross-polar isolation was 30.37 dB in  $H$  and 30.3 dB in  $V$ . To obtain the better cross-polar isolation, one element was set as canceler (the scaling factors are  $a = 0.92 + j0.06$  and  $b = 0.98 - j0.01$ ). Therefore, the copolar gain is reduced by roughly 0.28 dB in  $H$  and  $V$ .

### 4.3 Results

The XPC technique will be implemented as part of the Horus all-digital phased array radar, currently being assembled by the team of engineers at the ARRC at OU. In the meantime, XPC has been tested using simulations from an  $8 \times 8$  array populated with cross-dipole elements.

Concerning the element patterns, The co- and cross-polar patterns for the elements have been simulated using ANSYS High-Frequency Structure Simulations (HFSS). Two different procedures have been established to generate the element patterns:

- The element patterns are obtained from an infinite-array approach. This approach is ideal and ignores the edge effects. Throughout, the element patterns simulated using this procedure are called infinite-array element patterns. This procedure is less precise, but it is simpler to generate. This procedure is generally used on larger arrays in the phased array radar community.
- The element patterns are derived as embedded element patterns, obtained from the finite  $8 \times 8$  array (edge effects considered). Throughout, the element patterns generated using this procedure are termed finite-array embedded element patterns. The embedded element patterns are more precise but computationally expensive and time-consuming to simulate. The complexity of the simulation is directly proportional to the size of the array.

The resolution of the element patterns is  $2^\circ$  in both azimuth and elevation. The simulated element patterns, combined in the array described before, are used to calculate the array pattern. The simulated array has been steered within a scanning region between  $-45^\circ$  to  $45^\circ$  in azimuth and  $0^\circ$  to  $20^\circ$  in elevation. There is a  $2^\circ$  separation in the steering angles in azimuth and elevation. On each steering location, XPC calculates the number of canceler elements and scaling factors that improve the cross-polar isolation.

The simulation results are designed to test XPC under different conditions and to represent its performance when implemented on an operational phased array system. Therefore, two approaches are proposed to evaluate XPC:

- Approach 1: The simulated element patterns of a system, used as inputs on XPC, are a subpar estimation of the system. In approach 1, the number of canceler elements and scaling factors are calculated from the array with infinite-array element patterns. Then, the calculated values are tested in the array with finite-array embedded element patterns. Amplitude and phase errors have been added dur-

ing evaluation to simulate the performance of an operational array. The errors follow a zero mean-gaussian distribution with a standard distribution of -6 dB in amplitude and  $\pm 6^\circ$  in phase.

- Approach 2: The simulated element patterns of a system are a reasonable estimation of the system. This approach is similar to approach 1, but with one difference. The number of canceler elements and the scaling factors are calculated from the array with finite-array embedded element patterns.

It is expected that XPC performs better on approach 2 compared to one. Both approaches have been tested with the simulated array pointing broadside. Results are presented in Figures 4.6 and 4.7.

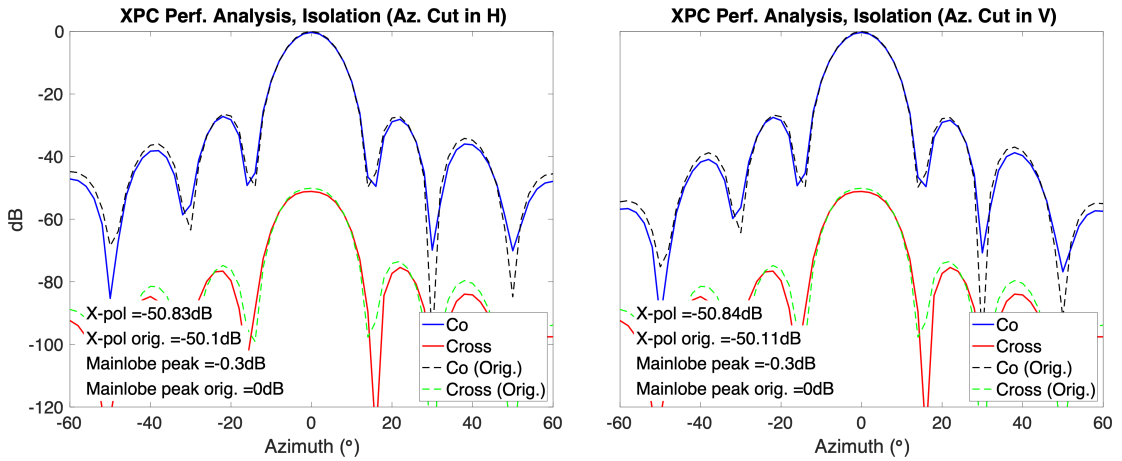


Figure 4.6: Evaluation of XPC under approach 1. The Array is pointing broadside. One element is repurposed as a canceler. The scaling factors on this element are  $a = 0.01 + j0$  and  $b = 0.01 - j0$ . The cross-polar isolation is improved from 50.1 dB in  $H$  and 50.11 dB in  $V$  to 50.83 dB in  $H$  and 50.84 dB  $V$ .

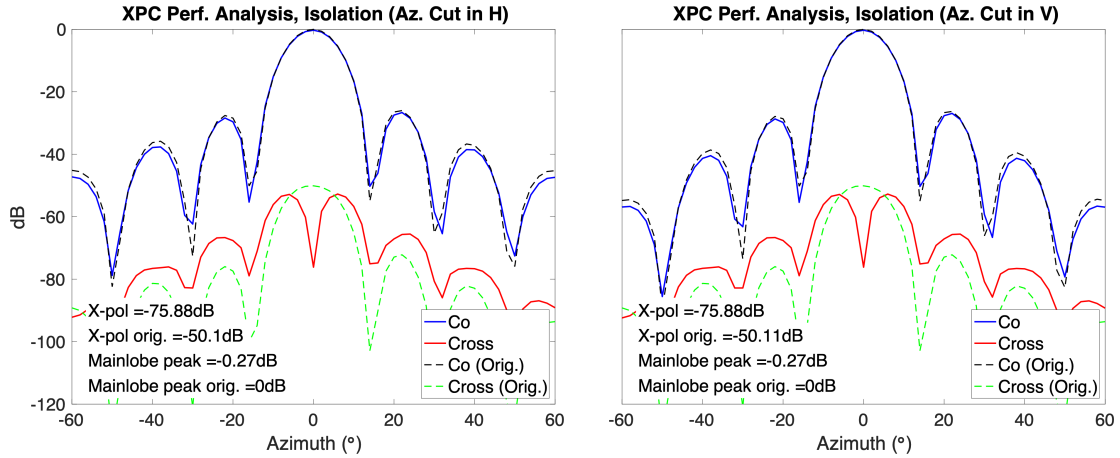


Figure 4.7: Evaluation of XPC under approach 2. The Array is pointing broadside. One element is repurposed as a canceler. The scaling factors on this element are  $a = 0.11 + j0.01$  and  $b = 0.09 - j0.01$ . The cross-polar isolation is improved from 50.1 dB in  $H$  and 50.11 dB in  $V$  to 75.88 dB in  $H$  and  $V$ .

From Figures 4.6 and 4.7, at broadside, there is minimal improvement over Approach 1. This effect has been hinted at previously. Nevertheless, this lack of improvement is mainly caused by the measurements provided by the XPC calculations. In addition, on the broadside, the cross-polar contamination is already fairly low and difficult to improve in both approaches. Moreover, the added errors also limit the XPC performance. Finally, the best solution in both approaches is to use one canceler element. Therefore, there is a loss in the copolar gain in both approaches. Specifically, 0.3 dB in  $H$  and  $V$  in approach 1 and 0.27 dB in  $H$  and  $V$  in approach 2.

A second test was performed with the array steered  $-20^\circ$  in azimuth and  $4^\circ$  in elevation. Results are presented in Figures 4.8 and 4.9. Unlike the previous case, when steered off the broadside, the cross-polar contamination is improved in both approaches. However, The loss in the copolar gain is similar to the previous case (same number of canceler elements).

Due to the randomness of the added errors, the XPC performance will be different each time the experiment is repeated. Nevertheless, it will not change the overall result

(XPC mitigates the cross-polar contamination).

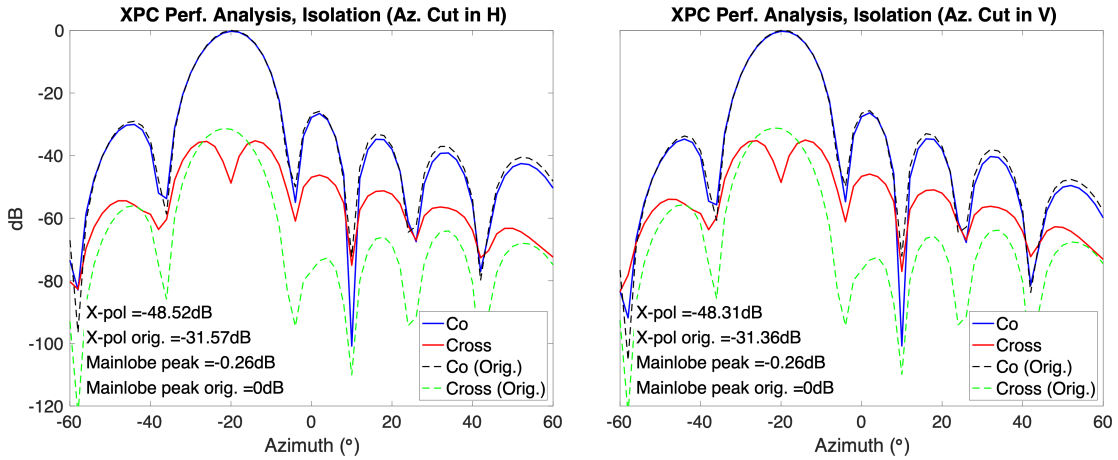


Figure 4.8: Similar to Figure 4.6, but for the array steered  $-20^\circ$  in azimuth and  $4^\circ$  in elevation. One element is used as canceler. The scaling factors on this element are  $a = 0.75 + j11$  and  $b = 0.78 - j0.12$ . The cross-polar isolation is improved from 31.57 dB in  $H$  and 31.36 dB in  $V$  to 48.52 dB in  $H$  and 48.31 dB in  $V$

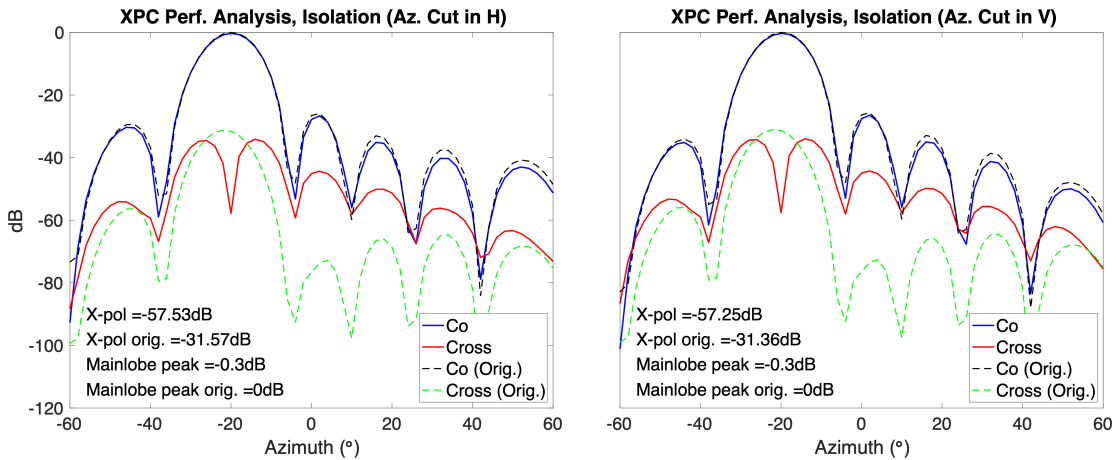


Figure 4.9: Similar to Figure 4.7, but for the array steered  $-20^\circ$  in azimuth and  $4^\circ$  in elevation. One element is used as canceler. The scaling factors on this element are  $a = 0.90 + j0.14$  and  $b = 0.75 - j0.12$ . The cross-polar isolation is improved from 31.57 dB in  $H$  and 31.36 dB in  $V$  to 57.53 dB in  $H$  and 57.25 dB in  $V$

The previous results are expressed in terms of the co- and cross-polar components of the array pattern. Nevertheless, in STSR, those components are not separable and are observed as one array pattern. Thus, another metric to measure the performance of

XPC is the array pattern purity (percentage). If there is no cross-polar contamination, in each polarization, the array pattern will equal its copolar component (100% array pattern purity). Nevertheless, the cross-polar contamination adds some distortion over this pure array pattern reducing the array purity. The pattern purity for each polarization ( $P_{0H}^{\%}$  and  $P_{0V}^{\%}$ ) are defined in (4.43) and (4.44).

$$P_{0H}^{\%} = \frac{V_{H(\text{co})}(R_s, m)}{V_H(R_s, m)} \quad (4.43)$$

$$P_{0V}^{\%} = \frac{V_{V(\text{co})}(R_s, m)}{V_V(R_s, m)} \quad (4.44)$$

Figures 4.10 and 4.11 reprocess the previous results in terms of the array pattern purity.

As expected, from Figures 4.10 and 4.11, the array pattern purity is significantly increased when XPC is implemented.

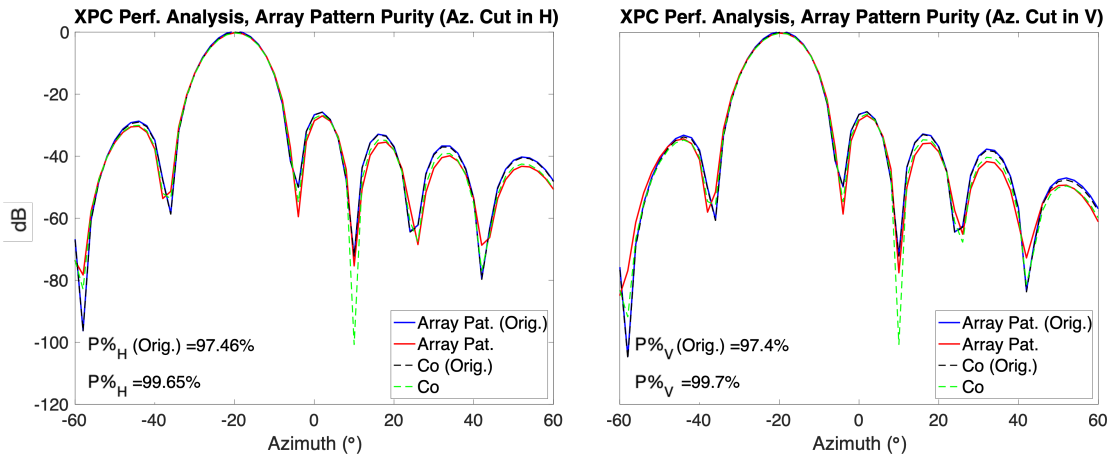


Figure 4.10: Similar to Figure 4.8, but plotting the array pattern purity. The array pattern purity increases from 97.46% in  $H$  and 97.4% in  $V$  to 99.65% in  $H$  and 99.7% in  $V$ .



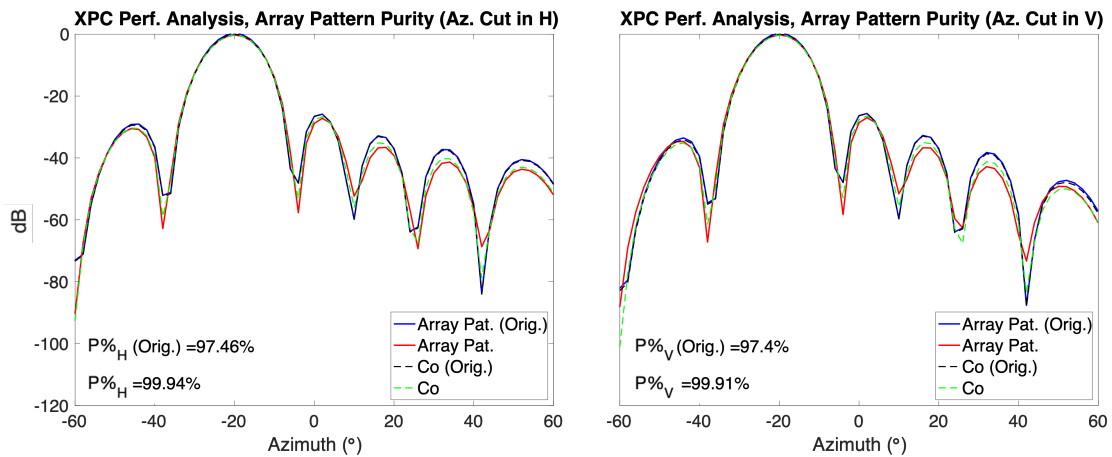


Figure 4.11: Similar to Figure 4.9, but plotting the array pattern purity. The array pattern purity increases from 97.46% in  $H$  and 97.4% in  $V$  to 99.94% in  $H$  and 99.91% in  $V$ .

In the previous examples, the performance of XPC at two angular locations has been evaluated. Nevertheless, the performance of XPC changes as the array is steered. The following sections evaluate XPC performance based on the derived array patterns for the entire scanning region. The parameters used for evaluation are the co- and cross-polar component of the array pattern, the loss in the copolar gain, and the array pattern purity.

### 4.3.1 Approach 1 Results

The calculations of the number of canceler elements and scaling factors as a function of steering angle are presented in Figure 4.12.

From Figure 4.12, the number of canceler elements increases as the array is steered (maximum of 10). The same is true for the magnitude of the scaling factor, but only in the regions where the number of canceler elements has not changed. Finally, the phase is close to zero radians. Nevertheless, it drastically changes at some particular steering positions. These positions are where the angular mismatch is noticeable.

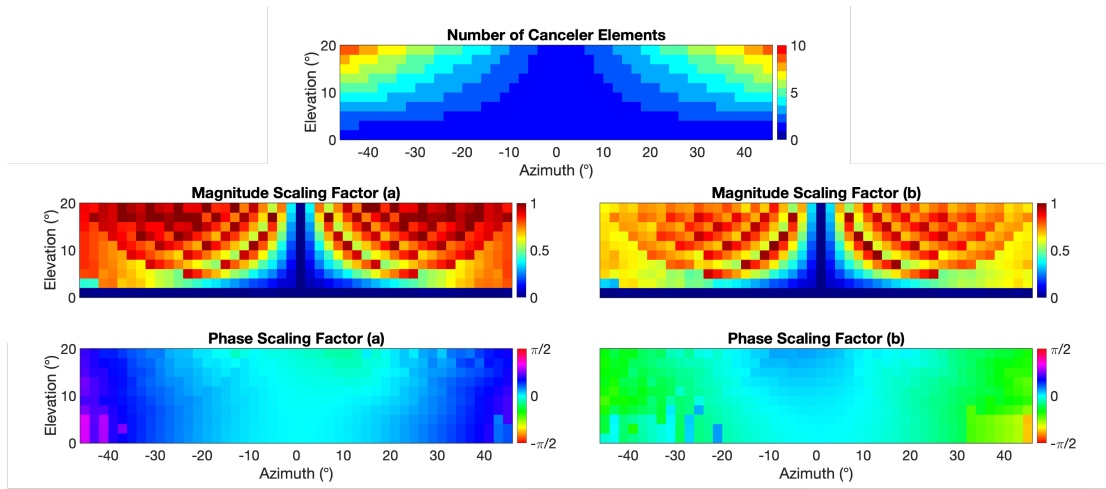


Figure 4.12: The calculated number of canceler elements and scaling factor on each steering position (approach 1). The number of elements (top) varies between 1 and 10. The magnitude of the scaling factor (middle) oscillates between zero and one. Finally, the phase of the scaling factor (bottom) is approximately zero radians except for the angles where the angular mismatch is noticeable in the patterns.

The canceler elements, and the corresponding scaling factors are used for testing XPC. The XPC performance as a function of steering angle is presented in Figures 4.13 and 4.14.

From Figure 4.13, implementing XPC improves the cross-polar isolation, regardless of the limited quality of the patterns used for its calculation. Numerically, in average, it is improved from 34.99 dB to 52.48 dB in  $H$  and 34.54 dB to 52.16 dB in  $V$ . Therefore, the extra improvement is approximately 14.55 dB in  $H$  and 14.16 dB in  $V$ . From Figure 4.14, implementing XPC increases the array pattern purity. In average, it is improved from 93.85% to 99.40% in  $H$  (5.56% improvement) and 92.48% to 99.38 dB in  $V$  (6.90% improvement).

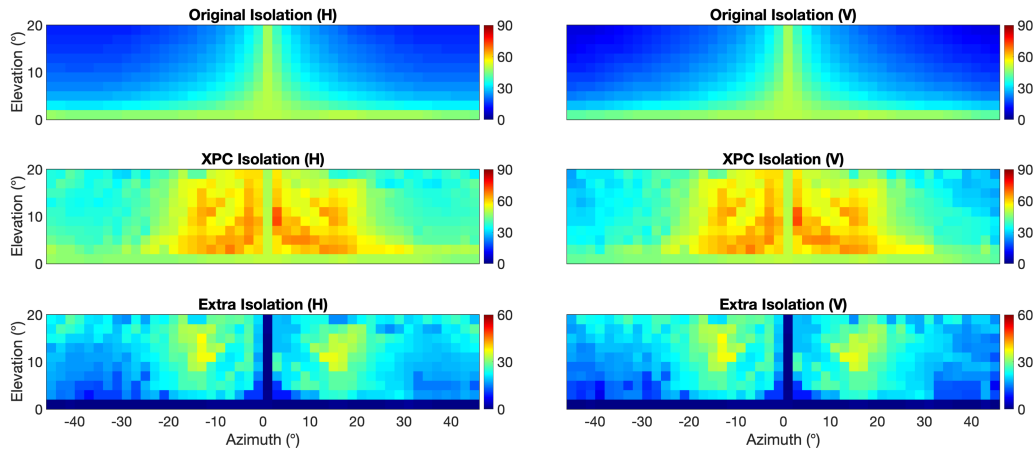


Figure 4.13: XPC performance from approach 1, based on the cross-polar isolation. The top two panels correspond to the original cross-polar isolation (in dB). In the middle panels, the improved cross-polar isolation, after implementing XPC, is presented (in dB). Finally, in the bottom two panels, the extra cross-polar isolation from XPC compared to the original one, is presented (in dB). The figure is divided into two columns. The left column corresponds to the results for the  $H$  polarization and the right for the  $V$  polarization.

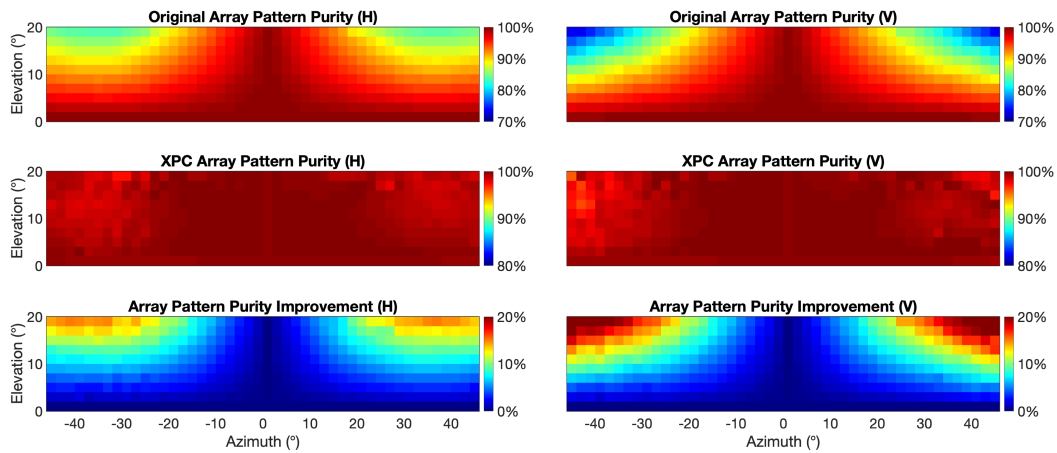


Figure 4.14: Similar to Figure 4.13, but for the array pattern purity (in %).

However, such improvement is not visible on the principal planes due to the difference in the array pattern for calculation and evaluation and the added errors. Additionally, there is observed that the improvement is lower as the beam is steered far from

the principal planes (farther than  $-25^\circ$  and  $25^\circ$  in azimuth). The edge effects (not considered in the calculations of approach 1) and the angular mismatch at these locations limit the performance of XPC.

In section 4.2.2, it has been explained that XPC impacts the copolar gain. This loss, as a function of steering angle, is presented in Figure 4.15.

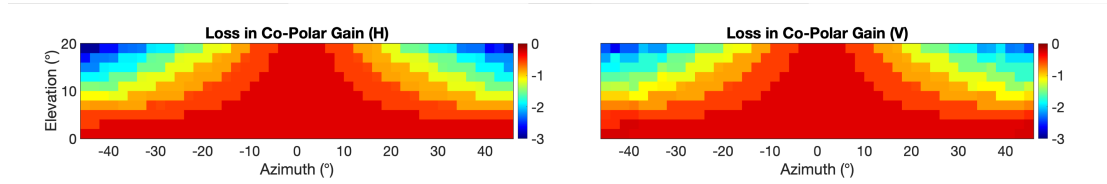


Figure 4.15: Loss in the copolar gain, as a function of steering angle, when XPC is implemented. The left panel corresponds to the loss in  $H$  and the right to the one in  $V$ . It is approximately proportional to the number of canceler elements.

From Figure 4.15, it is observed that the loss in copolar gain increases as the array is steered off-broadside. In a gross approximation, the loss can be assumed proportional to the number of canceler elements. Nonetheless, it also increases as the cross-polar contamination gets larger.

### 4.3.2 Approach 2 Results

The calculations of the number of canceler elements and scaling factors as a function of steering angle are presented in Figure 4.16. The calculations are similar to the ones from approach 1, except for the areas where the angular mismatch effect is visible (abrupt change in phase).

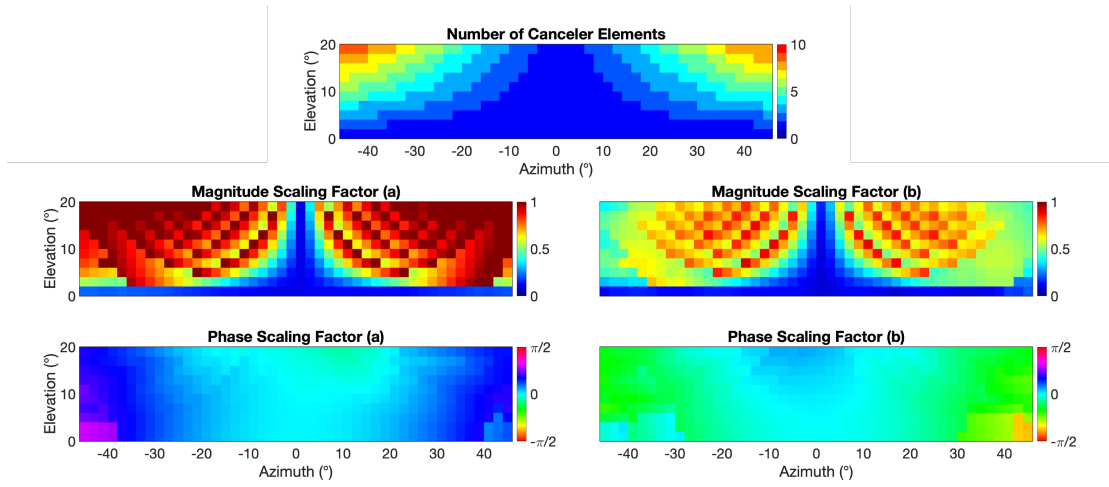


Figure 4.16: Similar to Figure 4.12, but calculated under the approach 2.

The canceler elements and the corresponding scaling factors are used for testing XPC. The XPC performance as a function of steering angle is presented in Figures 4.17 and 4.18. From Figures 4.17 and 4.18. The isolation and purity improvements are greater under approach 2, as expected. Numerically, in average, the isolation it is improved from 34.99 dB to 61.43 dB in  $H$  and 34.54 dB to 60.66 dB in  $V$ . Therefore, the extra improvement is approximately 25.55 dB in  $H$  and 23.27 dB in  $V$ . Concerning the array pattern purity, on average, it is improved from 93.85% to 99.78% in  $H$  (5.94% improvement) and 92.48% to 99.61 dB in  $V$  (7.12% improvement).

Compared to the previous results, XPC performs better under approach 2, especially in the principal planes. Nevertheless, the cross-polar mitigation is still not perfect. The angular mismatch and the added noise limit the performance of XPC.

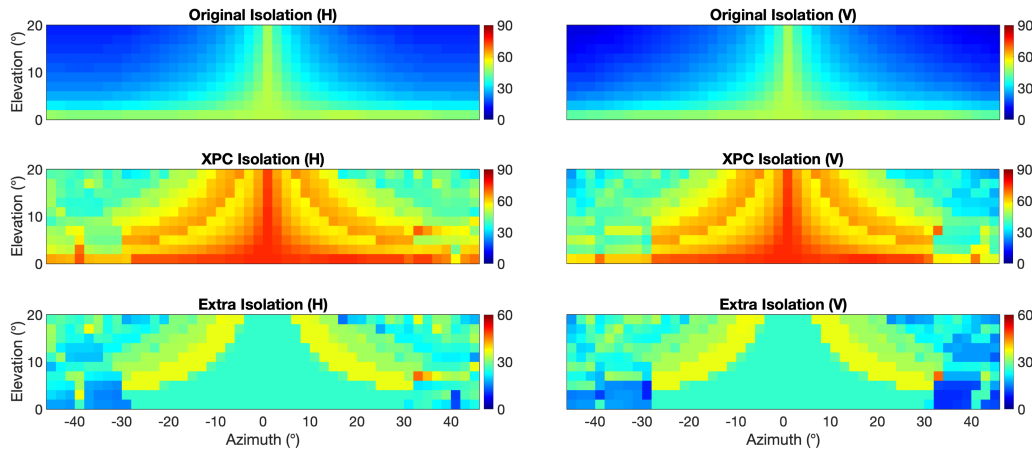


Figure 4.17: Similar to Figure 4.13, but evaluated under the approach 2.

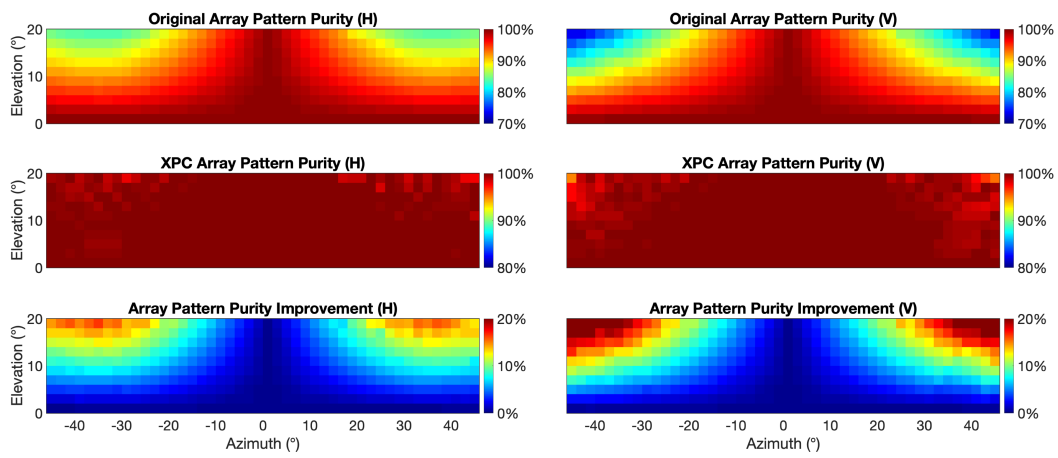


Figure 4.18: Similar to Figure 4.14, but evaluated under the approach 2.

The loss in the copolar gain is very similar to the one from approach 1 (see Figure 4.19). Therefore, concerning this, the same conclusions hold when compared to approach 1.

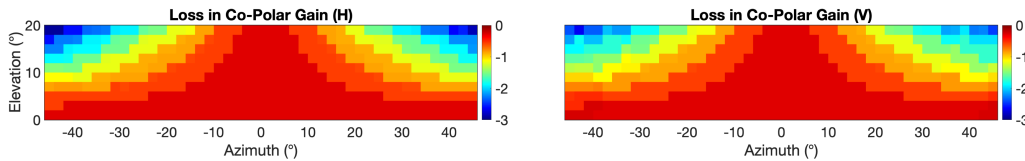


Figure 4.19: Loss in the copolar gain, as a function of steering angle, when XPC is implemented (approach 2). The left panel corresponds to the loss in  $H$  and the right to the one in  $V$ . It is approximately proportional to the number of canceler elements.

From the previous results, it has been shown that the XPC technique is a viable solution to mitigate cross-polar contamination. Its performance holds even when the patterns provided in the design are not realistic enough.

Based on the simulated array, and for both approaches, on average, XPC improves the cross-polar isolation in 15 dB at the expense of 0.85 dB in the copolar loss. Moreover, after implementing XPC, the average cross-polar isolation for the array is roughly 55 dB.

#### 4.4 Summary

In Chapter 4, a novel technique to mitigate cross-polar contamination in polarimetric phased array radars has been proposed. The technique is called XPC. It is a signal processing technique targeted to all-digital phased array radars.

For a specific array, XPC pre-configures a small group of canceler elements to transmit the inverse (i.e., the mathematical negative) of the original waveform in the cross-polarization direction. The canceler elements patterns are scaled in magnitude and phase. XPC calculates the number of canceler elements and the scaling factors necessary to better cancel the cross-polar contamination in each polarization ( $H$  and  $V$ ). XPC has been tested using simulations. Nevertheless, in the future, it will be necessary to validate these results in an operational all-digital phased array radar (Horus).

Even though XPC has been proposed to mitigate the cross-polar contamination on PARs, it is possible to implement this technique on more traditional radars based on reflector antennas. On those systems, auxiliary radiators could be mounted at the edge of the reflector antenna and programmed as canceler elements. Nevertheless, this concept has yet to be tested.

In the next chapter, there will be proposed improved versions of XPC and the PPC (see Chapter 3). These enhanced versions are developed to mitigate the limitations discussed in Chapters 3 and 4. The improved techniques are mainly focused on the “shoulder” effect (PPC) and the angular mismatch (XPC).



## Chapter 5

### Further Challenges and Proposed Solutions for the PPC and XPC Techniques

This chapter explores improvements to PPC and XPC for the limitations described in Chapters 3 and 4. The first section of Chapter 5 describes PPC+, an improved version of PPC. The second part discussed a new calibration strategy to mitigate the beam mismatch between the  $H$  and  $V$  array patterns.

#### 5.1 Mismatched Filter to Improve PPC - From PPC to PPC+

PPC has been implemented on PX-1000 and has been operational in that radar system since 2020. PPC has been used in different weather campaigns to collect various weather datasets (e.g., thunderstorms, storms, and snow). After implementing PPC, PX-1000 data inside the old “blind” range is indistinguishable from the visible range. Additionally, the sensitivity values in the blind range are higher when compared to the previous solution implemented for the system (TFM). In Figure 5.1 PPI plots are shown corresponding to different radar variables processed using PPC. The radar variables correspond to a dataset gathered from a snow event in the metropolitan area of Oklahoma City on February 03, 2022, 01:57:28 UTC at an elevation angle of  $4^\circ$ .

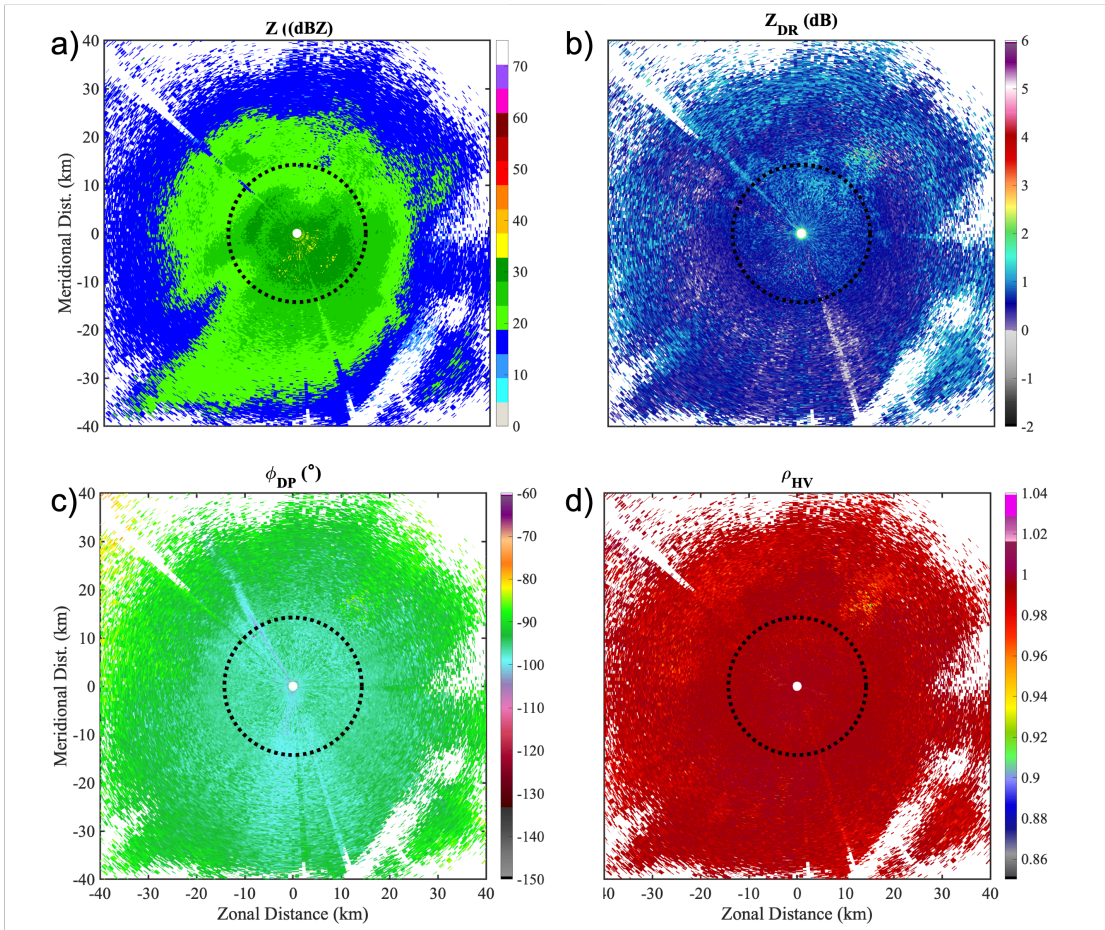


Figure 5.1: PPI plots of different radar variables processed using PPC: a)  $Z$  (top plot), b)  $Z_{DR}$ , c)  $\phi_{DP}$ , and d)  $\rho_{HV}$ , from a snow event observed in the metropolitan area of Oklahoma City on February 03, 2022, 01:57:28 UTC at an elevation angle of  $4^\circ$ .

Results presented in Figure 5.1 look similar to the ones presented in Section 3.3.2. Nevertheless, the waveform used in PX-1000 has been updated. One difference is the pulse width. The new waveform is significantly longer  $\tau = 95 \mu\text{s}$  (based on a similar NLFM). Therefore, when using the new waveform, the theoretical blind range is larger (i.e., 14.2 km in this case).

Additionally, different transmission modes have been implemented on PX-1000. One example is the ATSR mode, and PPC has been proven applicable within this mode. In Figure 5.2 there are presented the range height indicator (RHI) plots corresponding

to different radar variables processed using PPC. The radar variables are  $Z$  (top panel), SNR (middle panel), and the linear depolarisation ratio (LDR) (bottom panel). They correspond to a dataset gathered (in ATSR mode) from a storm event on May 23, 2022, 16:33:42 UTC, and processed using PPC.

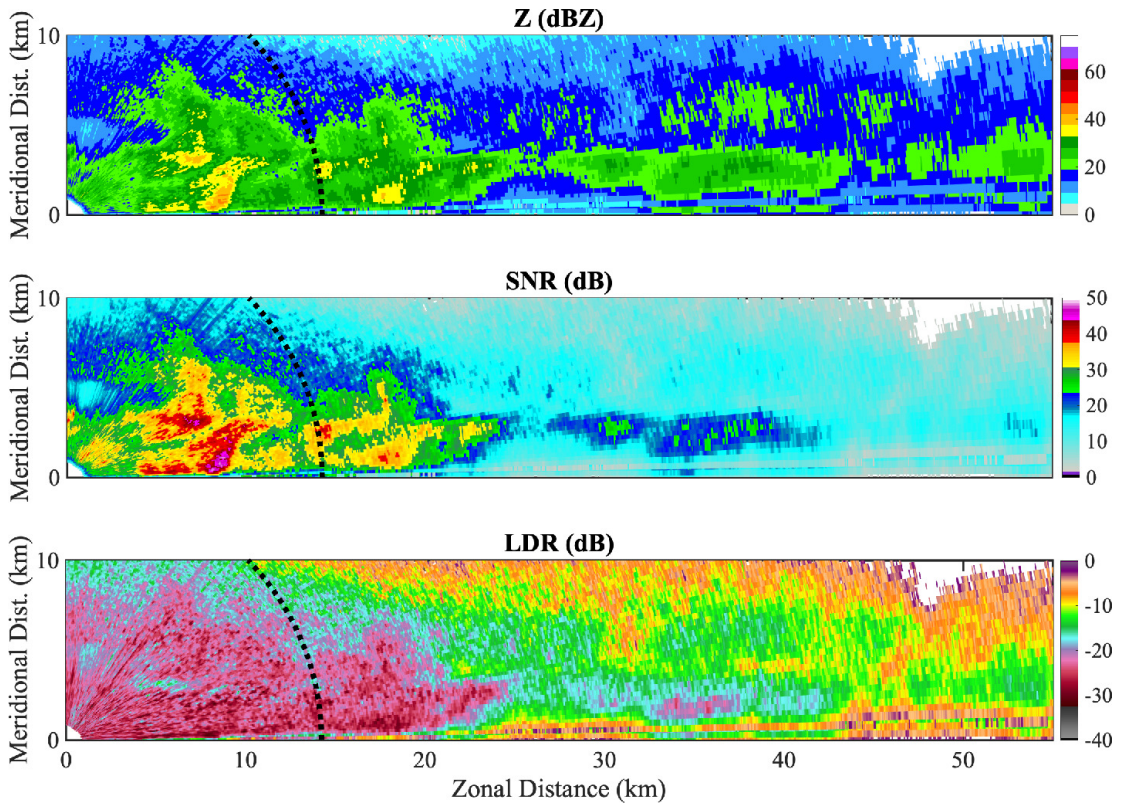


Figure 5.2: RHI plots of different radar variables processed using PPC:  $Z$  (top plot), SNR (middle plot), and LDR (bottom plot), from a storm event observed with the ATSR mode on May 23, 2022, 16:33:42 UTC.

From Figures 5.1 and 5.2, it can be seen that there is virtually no observable difference between the “blind” range and the visible range. Therefore, the term blind range is not applicable when using PPC. Then, from now on, the blind range will be termed the transmission range.

This seamless transition in the transmission range has also proven helpful in generating quasi-vertical profiles (QVP) [87]. Using QVP is an inventive way to emulate

the results from vertical profilers from PPI scans collected at high elevations [87]. Figure 5.3 illustrates the QVP of  $Z$  (left plot),  $Z_{DR}$  (center plot), and  $\rho_{HV}$  (right plot) generated from a PPI gathered from a snow event in the metropolitan area of Oklahoma City on February 03, 2022, 02:37:39 UTC ( $12^\circ$  in elevation). The PPI has been collected from PX-1000 and processed using PPC.

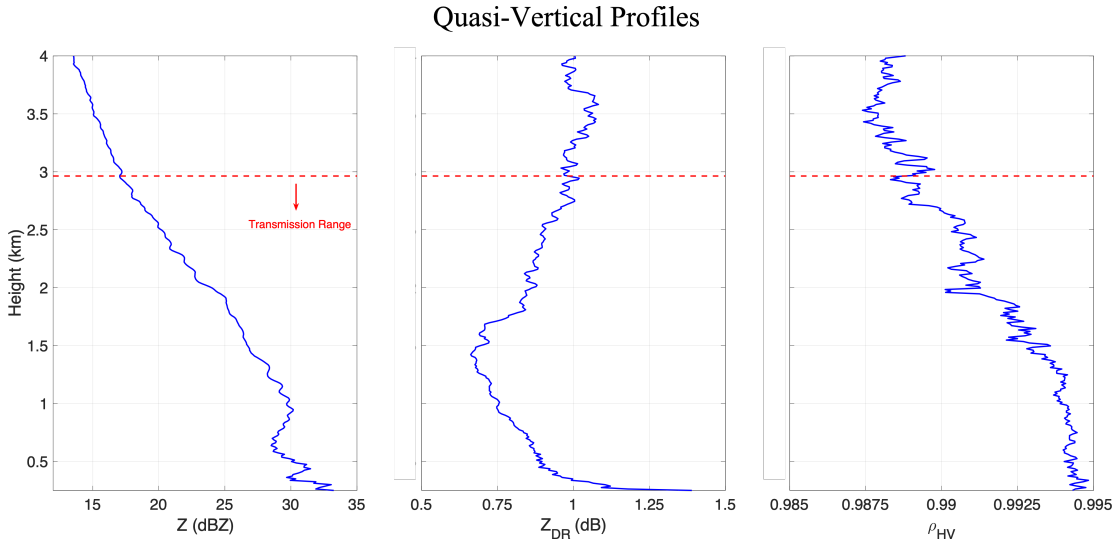


Figure 5.3: QVP of  $Z$  (left plot),  $Z_{DR}$  (center plot), and  $\rho_{HV}$  (right plot) generated from a PPI gathered from a snow event in the metropolitan area of Oklahoma City on February 03, 2022, 02:37:39 UTC ( $12^\circ$  in elevation).

From Figure 5.3 it can be observed that the first 3 km in elevation of the QVP corresponds to the transmission range. Additionally, when using PPC, there are no drastic changes in the values of  $Z$ ,  $Z_{DR}$ , and  $\rho_{HV}$  before and after the transmission range.

Nonetheless, PPC has some downsides discussed in Chapter 3, mainly the “shoulder” effect. This shoulder effect is present in certain datasets processed with PPC and has been pointed out by the scientific community. This limitation is observable in the PPI plots presented in Figure 5.4. The PPI plots correspond to a dataset gathered from a convective storm event on March 18, 2022, 00:33:44 UTC at an elevation angle of  $2^\circ$

, and have been processed using PPC.

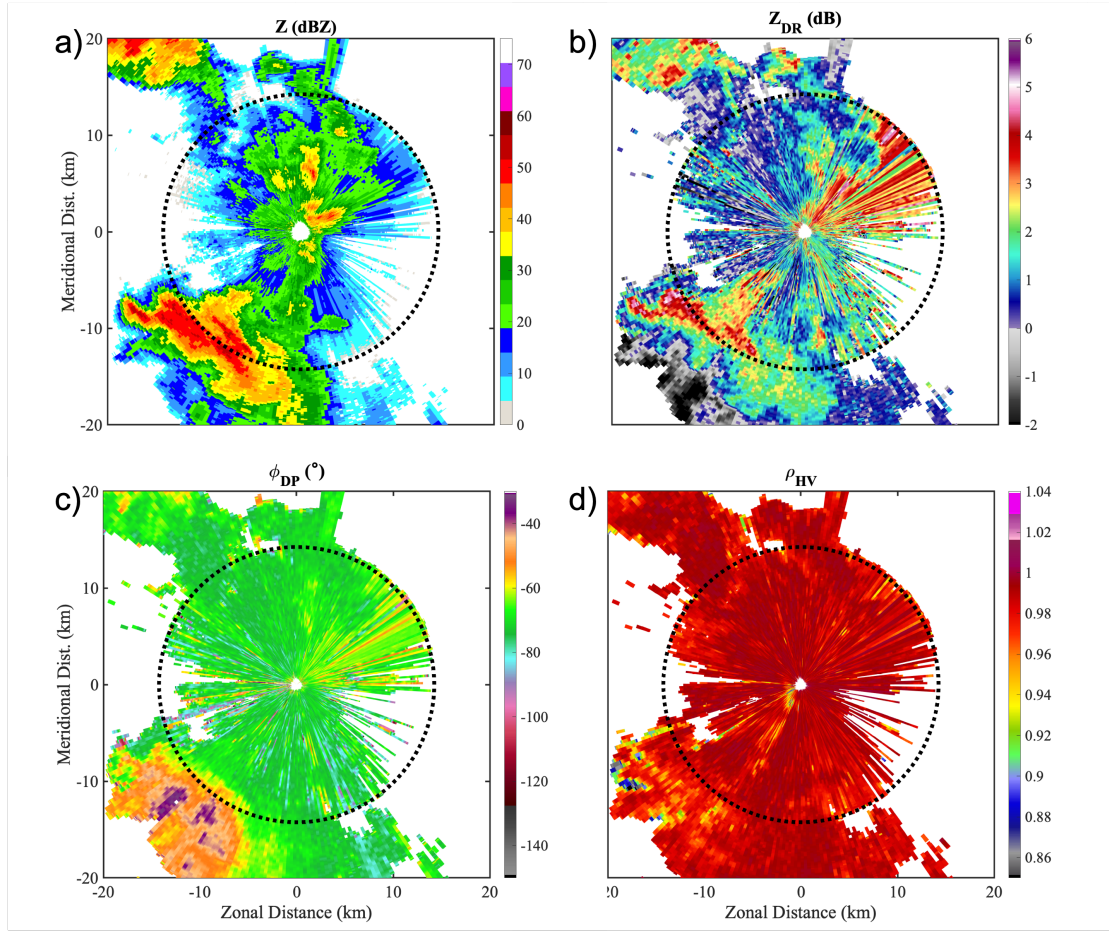


Figure 5.4: PPI plots of different products processed using PPC: a)  $Z$  (top plot), b)  $Z_{DR}$ , c)  $\phi_{DP}$ , and d)  $\rho_{HV}$ , from a convective storm event observed on March 18, 2022, 00:33:44 UTC at an elevation angle of  $2^\circ$ .

In Figure 5.4, contamination from the shoulders of the PPC waveform can be observed in the northeast, southeast, and west regions of the transmission range (especially in the  $Z$  plot). The shoulders can obscure weaker echoes located in the same azimuth direction. They shadow the returns along the range. The shoulders contaminate both sides of the scatterers in the range direction. Moreover, this shadow becomes longer as the weather gets closer to the radar.

An improved version of PPC, termed PPC+, is proposed as an alternative to mitigate

the undesirable shoulder effect. The improved PPC+ methodology is explained in the following section.

### **5.1.1 Methodology**

The received signal is modified to eliminate the contamination from the transmission when using PPC. The modified received signal corresponding to a specific range is then pulse-compressed with a matched filter. However, inside the transmission range, the return signal used for compression differs depending on the range gate. Thus, the frequency content, length, and design of the matched filter are different than the one from the modified signal (see Section 3.2.2), producing the shoulder effect. Therefore, a fixed matched filter is inadequate for compressing the incomplete return signal. A solution to this issue is to implement a changing filter inside the transmission range. This new changing filter is termed a range-dependent mismatched filter. PPC+ is then similar to PPC but uses a mismatched filter.

The design of the mismatched filter and the practical implications in PPC+ are discussed in the next section.

#### **Mismatched Filter Design and Partial Decoding**

The mismatched filter is a modulated version of the original matched filter. The mismatched filter replaces the matched filter in the compression inside the transmission range. There are two alternatives for the design of the mismatched filter, i.e., using frequency modulation [88] or using amplitude modulation (tapering). A solution based on amplitude modulation is investigated here.

The design of the mismatched filter is a two-step process. The first step is to zero out part of the original matched filter. This modification will reduce the shift in the

main lobe observed with PPC. The zero-out process changes some samples in the filter to zero to match the number of zeroes in the corresponding modified received signal. Therefore, each modified filter will have a different number of zeroes as a range function.

The number of zeroes in the mismatched filter can be estimated based on Figure 3.3. From Figure 3.3, the received signal has an echo located  $R_t$  km ( $t_t$   $\mu$ s), that extends  $R_p$  km ( $\tau$   $\mu$ s), and ends at  $R_t + R_p$  km ( $t_t + \tau$   $\mu$ s). Additionally, the first  $R_p$  km ( $\tau$   $\mu$ s) samples of the received signal are zeroed out due to contamination from the transmission. Therefore, the samples corresponding to the first  $R_p - R_t$  km ( $\tau - t_t$   $\mu$ s) of the echo are zeroed out. Then, the mismatched filter to compress the signal should have the same number of samples zeroed out at the beginning.

The second step in the mismatched filter design is to apply a taper in amplitude to the remaining non-zero samples in the mismatched filter using a window function. This step is designed to reduce the sidelobe levels, causing the shoulder effect.

The window function must be carefully tuned to reduce the sidelobe contamination and minimize the power loss in the compressed signal. An aggressive taper is more effective in mitigating the shoulders. However, it negatively impacts the sensitivity of the system.

The aggressiveness of the taper can be changed based on the window function selected and its design parameters. In this work, a tapered cosine (Tukey) window function [89] is used. The roll-off factor used in the Tukey function (expressed as a normalized weight) is related to the number of samples modulated by the cosine. For example, if the roll-off factor is one, 100% of the elements are modulated (the most aggressive option for the Tukey window). On the contrary, if the roll-off factor is zero, the taper is equivalent to using a boxcar or rectangular window [89, 90].

An illustration of the window used to produce the mismatched filter is presented in

Figure 5.5, at the range  $R_t$  km ( $t_t$   $\mu$ s).

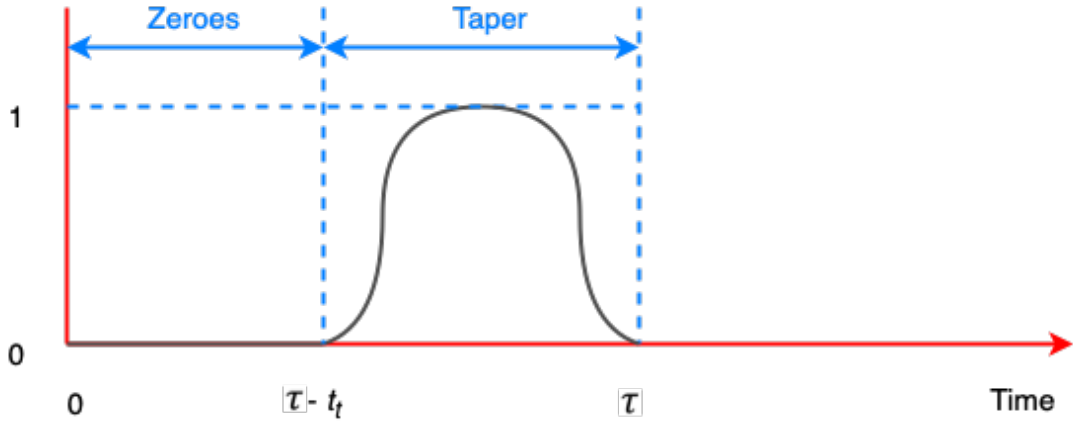


Figure 5.5: Depiction of the window used to generate the mismatched filter, at the range  $R_t$  km ( $t_t$   $\mu$ s).

The use of a mismatched filter changes the pulse-compressed signal (Equation (3.3)). The new equation to calculate the compressed signal in PPC+ is

$$y'(n) = \sum_{\tau} x'(\tau + n)x_n^*(\tau), \quad (5.1)$$

where  $x_n(\tau)$  is the mismatched filter at the sample index  $n$ , and  $x_n(\tau)$  is

$$x_n(\tau) = w_n(\tau)x_t(\tau), \quad (5.2)$$

where  $w_n(\tau)$  is the window function to derive the mismatch filter at the range index  $n$ . If  $n$  is located outside the transmission range, the matched filter is used, and then  $x_n(\tau) = x_t(\tau)$ .

In Equation (5.1), the complex conjugate of  $x_n(\tau)$  is used,

$$x_n^*(\tau) = w_n^*(\tau)x_t^*(\tau). \quad (5.3)$$

Since the values in the  $w_n(\tau)$  expression are not complex, then,



$$x_n^*(\tau) = w_n(\tau)x_t^*(\tau). \quad (5.4)$$

It is necessary to recalculate the calibration factor used in PPC to compensate for the taper in PPC+. The calculation is presented in the following section.

### Calibration Factor

From Equation (3.4), the estimated compressed signal at the sample gate  $n$  ( $y_e(n)$ ) is a function of  $y'(n)$ . A new expression for  $y'(n)$  is derived here for PPC+. The new equation for  $y_e(n)$  is derived combining (3.4) and (5.1),

$$y_e(n) = s(n) \sum_{\tau} x'(\tau + n)x_n^*(\tau). \quad (5.5)$$

The scaling factor  $s(n)$  is derived from Equations (3.4) and (5.5), and it is approximately equal to

$$s(n) = \sqrt{\frac{\sum_{\tau} |x_t(\tau)|^2}{\sum_{\tau} w(n + \tau)w_n(\tau)|x_t(\tau)|^2}}. \quad (5.6)$$

The new calibration factor correctly estimates the fully compressed received signal inside the transmission range, including the effects of the mismatched filter. Additionally, using a mismatched filter affects the sensitivity of the radar inside the transmission range.

### 5.1.2 Sensitivity Analysis

The sensitivity function is calculated using Equation (3.9). Nevertheless, in PPC+, the mismatched filter affects the sensitivity of the radar system, generating an additional loss. The sensitivity loss can be quantified using the taper efficiency equation [38].

$$L_w(n) = \frac{\left( \sum_{\tau} w(n + \tau)w_n(\tau) \right)^2}{N_w \left[ \sum_{\tau} (w(n + \tau)w_n(\tau))^2 \right]}, \quad (5.7)$$

where  $N_w$  represents the number of range-time samples over the pulse (pulse width  $\tau$ ). Then, for PPC+, the sensitivity ( $Z_{min}$ ) is approximately equal to

$$Z_{min}(n) \approx \frac{P_n 2^{10} \ln(2) \lambda^2 R^2 l^2 l_r}{\pi^3 P_t L_w(n) G^2 g_s \theta^2 c \tau |K_w|^2}. \quad (5.8)$$

A sensitivity plot for PPC+ compared to PPC and TFM is presented in Figure 5.6. The different sensitivity profiles in Figure 5.6 have been calculated using the OFM waveform described in Chapter 3. Additionally, the pulse compression filter used for PPC+ is designed using a Tukey window with a roll-off factor of one.

As seen in Figure 5.6, implementing PPC+ reduces the sensitivity of the system when compared to the legacy PPC. Inside the transmission range, the sensitivity profile of PPC+ (green line) is approximately 2 to 3 dB higher than PPC (red line). This loss is observed throughout the transmission range and causes a discontinuity in PPC+ inside the transmission range. Nevertheless, even with the extra sensitivity loss inside the transmission range, PPC+ provides better sensitivity than TFM (yellow line).

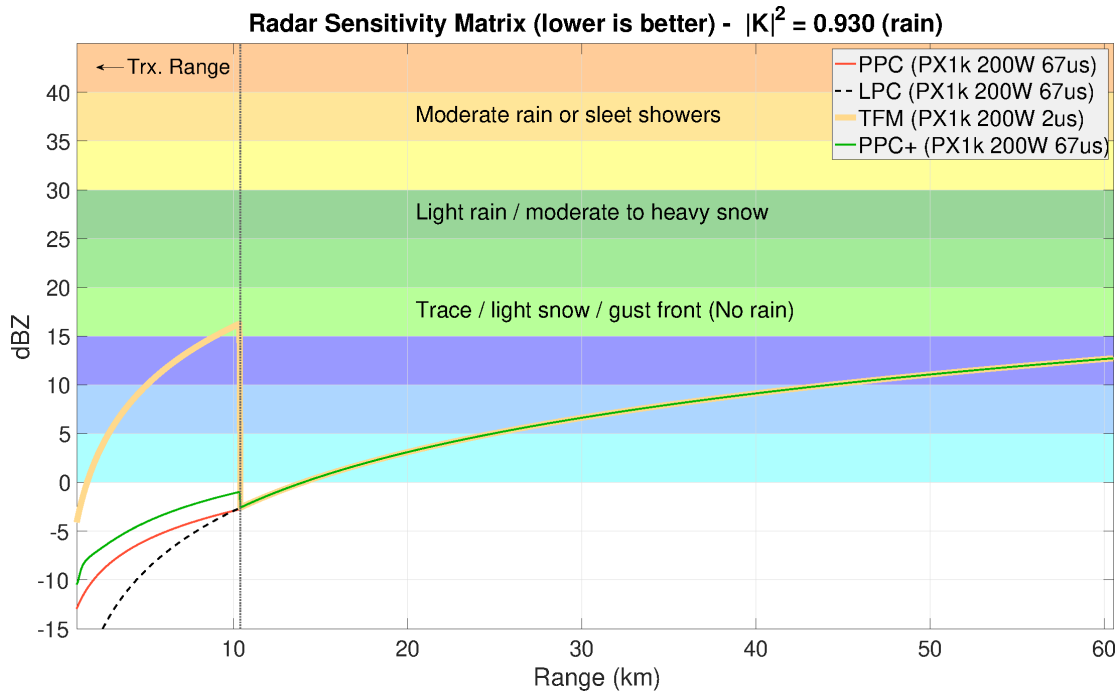


Figure 5.6: sensitivity profiles for different blind mitigation techniques implemented on PX-1000. Similar to Figure 3.5, the hypothetical sensitivity profile of the OFM waveform is included in the plot (black dashed line). Using a mismatched filter reduces the sensitivity of PPC+ compared to PPC inside the transmission range. Nonetheless, using PPC+ still provides significantly better sensitivity than TFM.

The use of PPC+ has advantages over PPC. The main advantage is the mitigation of the shoulder effect. Nevertheless, the technique has some limitations to be discussed. One of the limitations is the decrease in the sensitivity inside the transmission range compared to PPC. An in-depth review of the advantages and limitations of PPC+ compared to PPC is presented in the following section.

### 5.1.3 Advantages and Limitations of PPC+

#### Ambiguity Function of Targets Inside the Transmission Range

As explained in previous sections, the main improvements of PPC+ over PPC are the reduction in the main lobe peak shift and the mitigation of the shoulder effect. The im-

improvements can be illustrated by calculating the ambiguity function using PPC+ (Tukey window and roll-off factor of one) and based on the OFM waveform (compare with similar results in Chapter 3), as shown in Figure 5.7.

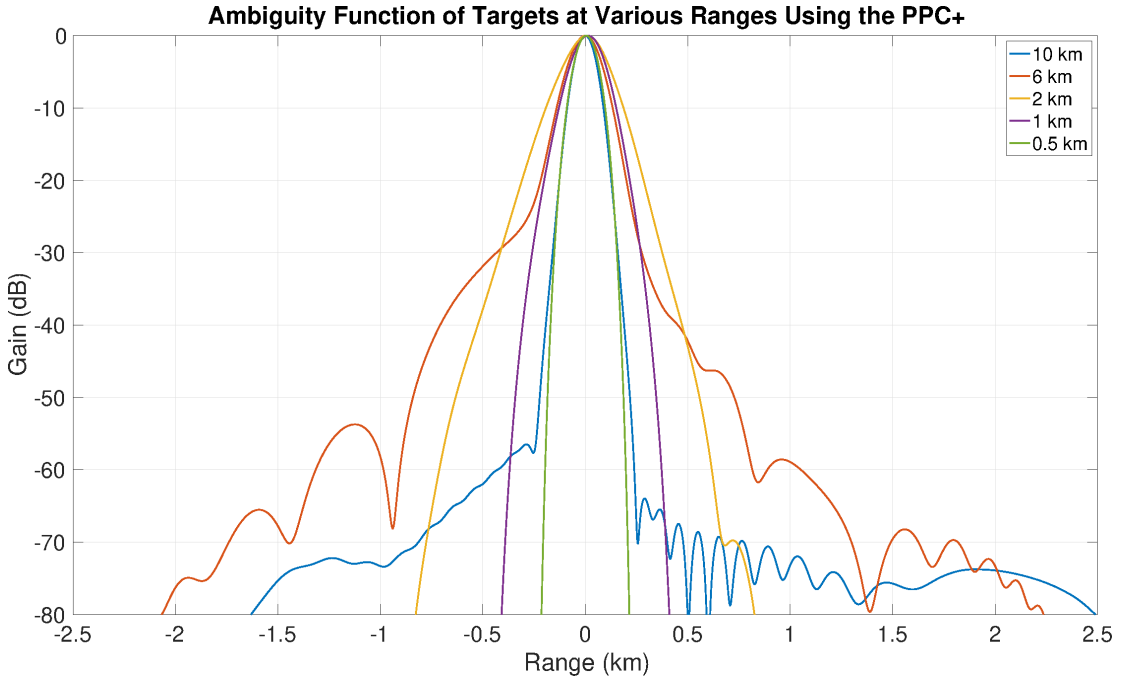


Figure 5.7: Ambiguity function using PPC+ and based on the OFM waveform at different range gates. Comparing the results from PPC+ to the ones from PPC (see Figure 3.10), it can be seen that the main lobe peak migration is lower in PPC+, and the shoulder effect is less prominent. The shoulder reduction is more pronounced at closer ranges.

The ambiguity functions in Figure 5.7 have been calculated for the same range gates as those in Figure 3.10. In Figure 5.7, the shoulders observed when using PPC+ are less pronounced (narrower main lobe) compared to the ones in PPC, especially in the range gates closer to the radar. Additionally, a significant reduction in the main lobe peak migration is observed on PPC+ compared to PPC. Nevertheless, to better illustrate these improvements, the ambiguity functions at two range gates (1 and 8 km) are calculated with both PPC and PPC+ (see Figure 5.8).

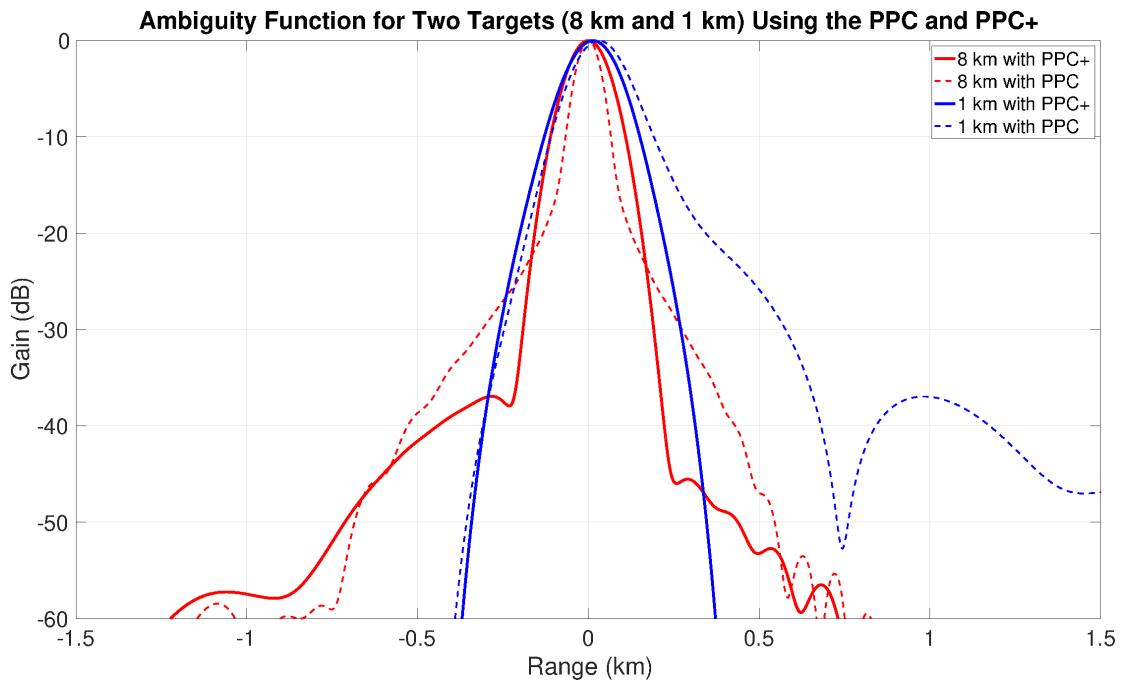


Figure 5.8: Ambiguity functions for two range gates located 1 and 8 km from the radar (blue and red lines), using PPC (dashed lines) and PPC+ (solid lines). A noticeable reduction in the shoulder effect is observed in the PPC+ ambiguity functions.

From Figure 5.8, the shoulders in both ambiguity functions are lower when processed with PPC+. For the range gate at 1 km, sidelobes are at least 60 dB below the main lobe, and no shoulders are visible on the plot. Concerning the main lobe peak offset, a reduction is expected when using PPC+. Nevertheless, to better observe this improvement, a zoomed-in version is shown in Figure 5.9. From Figure 5.9, the main lobe peak offset is visible on the ambiguity function from the range gate at 1 km. After implementing PPC+, that offset is still present but has been significantly reduced, from 30 m (when using PPC) to roughly 13 m.

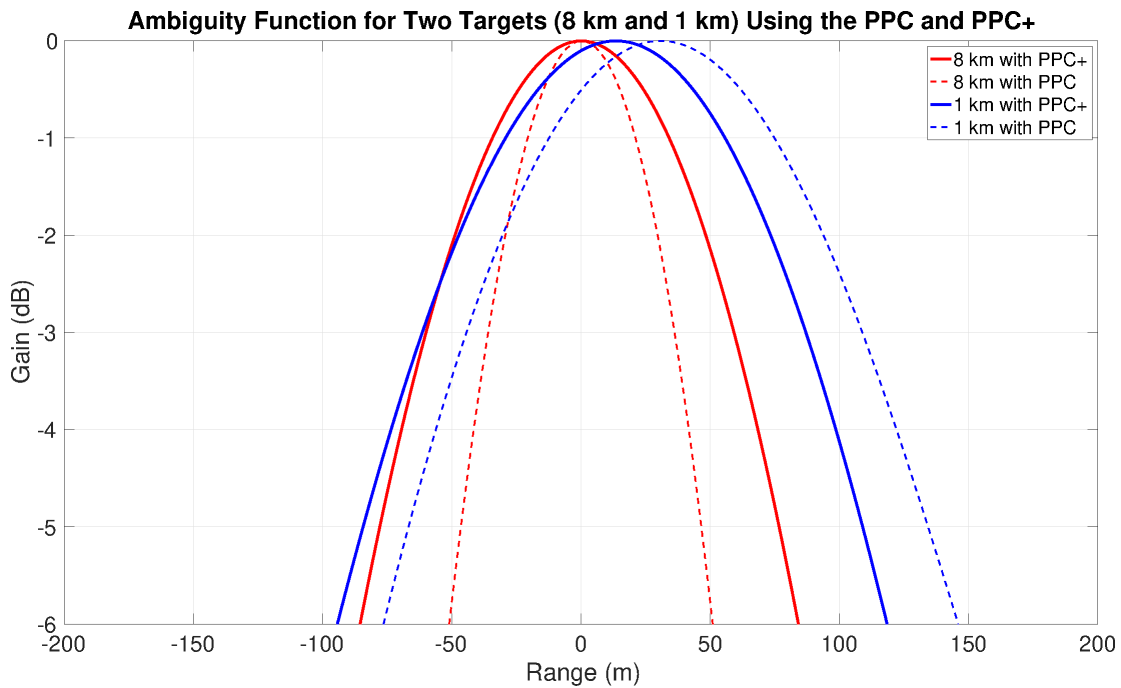


Figure 5.9: Similar to Figure 5.8, but zoomed in to observe the main lobe peak locations.

Applying a mismatched filter on receive provides a simple and effective solution for the limitations observed in PPC. However, PPC+ also has some limitations, caused mainly by the amplitude taper used in the mismatched filter. These limitations will be discussed in the following section.

### Limitations of PPC+

One of the limitations of PPC+ is that radar sensitivity inside the transmission range is lower than that of PPC. The reduction is proportional to the difference in power between the mismatched and matched filters. Additionally, when using PPC+, there is a discontinuity at the end of the transmission range. This discontinuity is also proportional to the difference in power described before, but generally, it is less significant than the one observed when using TFM.

Additionally, using a window function also widens the main lobe width, affecting the range resolution of the compressed return. The reduction in the range resolution varies as a function of range. The wider main lobe is the second limitation of modulating the mismatched filter using a window function. This is illustrated in Figure 5.10.

In the top panel of Figure 5.10, the range resolution resulting from PPC+ (Tukey window and roll-off factor of one) is estimated as a function of range (based on the OFM waveform). The estimated range resolution is compared with the corresponding one using PPC (presented in the middle plot in Figure 3.8). Also, a similar comparison is performed based on the estimated main lobe peak offset as a function of range (see bottom panel in Figure 5.10).

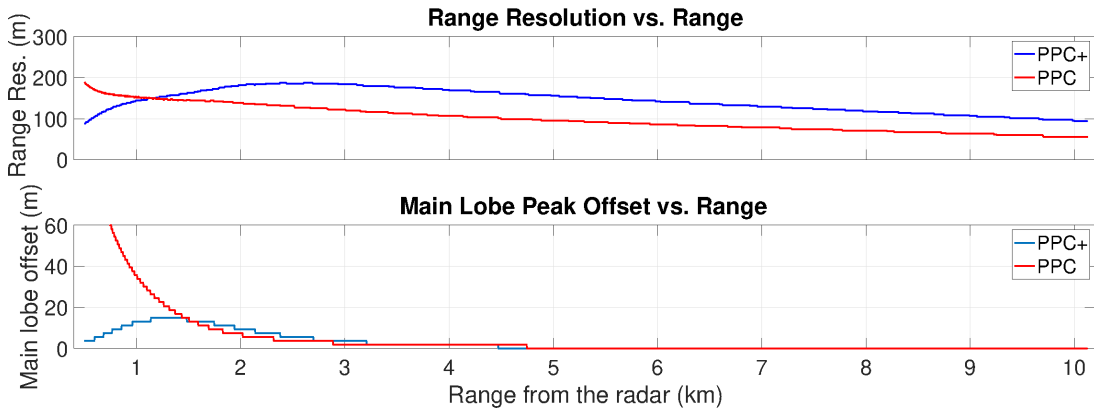


Figure 5.10: The top and bottom panels show the range resolution and main lobe peak offset as a range function. Results from PPC+ are compared with similar ones processed using PPC (extracted from Figure 3.8)

From the top panel in Figure 5.10, it is observed that using a mismatched filter in PPC+ negatively impacts the range resolution (lower than the one from PPC). The lower range resolution is observed in most range gates except those closest to the radar. In the closer range gates, the shoulders observed when using PPC are more prominent (broader and higher in magnitude), affecting the range resolution, as observed in Figure 3.10. PPC+ mitigates the shoulders, improving the range resolution at these range

gates. It could be argued that the shoulder mitigation from PPC+ overcomes the loss in range resolution from the taper.

Finally, in the lower panel of Figure 5.10, it is observed that the main lobe peak offset is significantly reduced when using PPC+. Nevertheless, offset mitigation is not perfect, which is another limitation of using a window function to modulate the mismatched filter.

The limitations above are not related to using a mismatched filter but to using amplitude modulation in its design. It is theorized that using a mismatched filter modulated in phase (rather than amplitude) might produce a comparable shoulder mitigation and none of the limitations described before. Nevertheless, implementing a mismatched filter using phase modulation is out of the scope of this dissertation. Its design, analyses, and testing are proposed as a future research path to improve PPC+ further.

#### **5.1.4 Results**

In this section, PPC+ (Tukey window and roll-off factor of one) will be evaluated using both simulated and real data. The real data were collected with PX-1000, a radar system currently using PPC. Thus, PPC and PPC+ can be easily compared using data from PX-1000.

##### **Simulation Results**

A realistic simulation was performed to evaluate the performance of PPC+ and compare it to legacy PPC.

Four targets are simulated. Two are located inside the transmission range and two outside. The simulation is based on the OFM waveform and is designed similarly to the one in Section 3.3.1. Nevertheless, different from Section 3.3.1, both PPC and



PPC+ are implemented and compared here. The simulation results are presented in Figure 5.11.

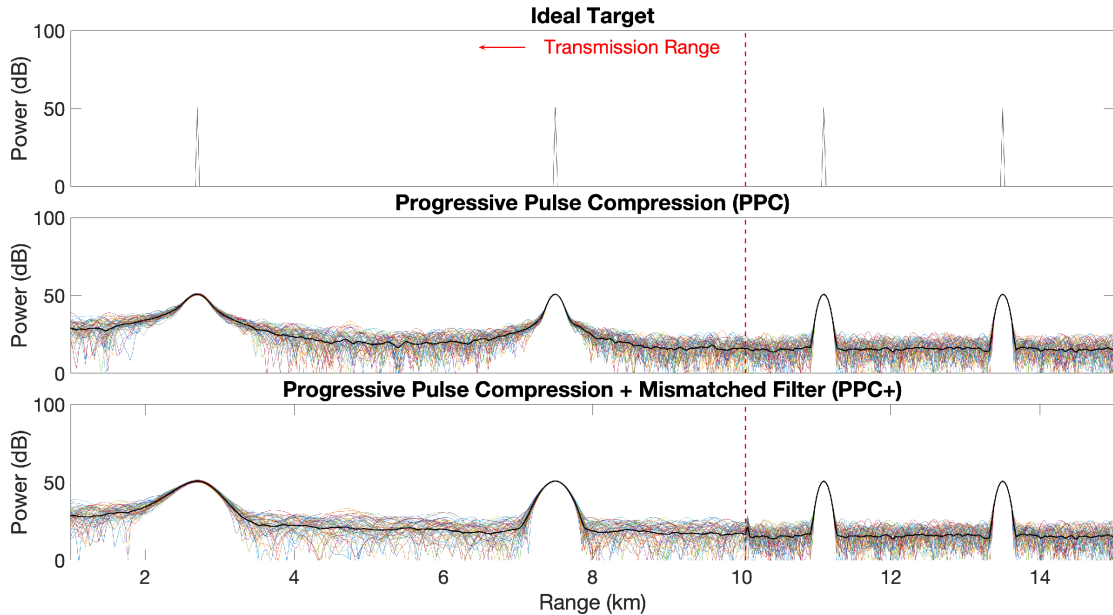


Figure 5.11: Simulation results when transmitting the OFM waveform. The top plot illustrates the ideal location and power of the simulated targets. In the middle panel, the simulation results from the PPC are presented. Similar results are shown on the lower plot but from the PPC+. The simulation demonstrates that when processed using PPC+, the shoulder contamination is significantly reduced compared to PPC.

In Figure 5.11 it is shown the simulation setup and power profile from the PPC and the PPC+ techniques. The top panel shows the target locations, while the middle and bottom panels correspond to the results processed with PPC and PPC+. As expected, PPC+ has less shoulder contamination than PPC. Moreover, the shoulder contamination is fully mitigated for the target closer to the end of the transmission range. Nevertheless, the mitigation is still not perfect, as the target located closer to the radar is still affected by it when using PPC+. In addition, the increase in the main lobe width of the target can also be observed in Figure 5.11. A trade-off that must be considered when designing the mismatched filter.

## Experimental Results

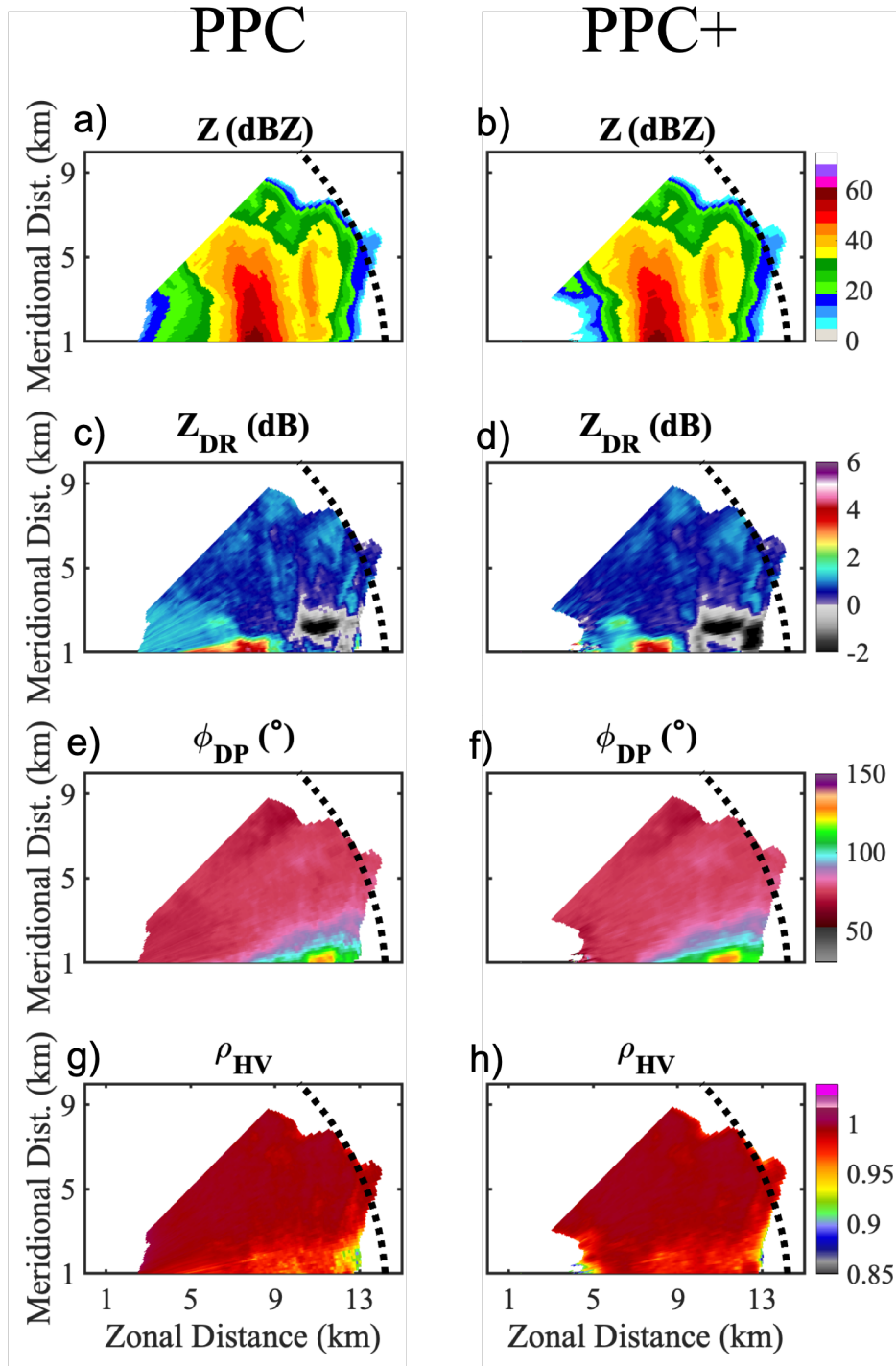


Figure 5.12: Products processed using PPC: a)  $Z$ , c)  $Z_{DR}$ , e)  $\Phi_{DP}$ , g)  $\rho_{HV}$ . Products processed using PPC+: a)  $Z$ , c)  $Z_{DR}$ , e)  $\Phi_{DP}$ , g)  $\rho_{HV}$ . In the PPC+ plots, it is shown that the shoulder effect, observed in the PPC plots (before 5 km), has been greatly reduced.

In this section, legacy PPC and PPC+ are compared using raw uncompressed polarimetric data collected with PX-1000. The dataset analyzed is from an RHI scan collected on July 25, 2022, 20:49:23 UTC. The dataset has precipitation observed approximately between 5 and 15 km. The waveform used on PX-1000 was the improved 95  $\mu\text{s}$  pulse. Therefore, the transmission range is approximately 15 km.

A subset of polarimetric radar measurements are calculated from the selected dataset and presented in Figure 5.12. These include the reflectivity factor ( $Z$ ), differential reflectivity ( $Z_{\text{DR}}$ ), differential phase ( $\Phi_{\text{DP}}$ ), and correlation coefficient ( $\rho_{\text{HV}}$ ).

From Figure 5.12, the echoes observed in the first 5 km of the panels corresponding to PPC (left column) are caused by the shoulder effects. The shoulders are manifested in all estimates and resemble smeared targets. The shoulder effect is especially noticeable on the  $Z_{\text{DR}}$  plot, where rays of high  $Z_{\text{DR}}$  extend in the first 5 km at different elevations. In contrast, PPC+ fully mitigates these shoulders. Therefore, the previously obscured echoes are recovered and observed in the panels corresponding to PPC+ (right column).

For example, when using PPC, in the  $Z$  plot (panel a)), contamination is observed near the edge of the storm located roughly 5 km away from the radar. Moreover, the values create an artifact that aligns with the similar values along range. None of that contamination is visible after using PPC+ (panel b)).

A significant improvement is observed in the polarimetric estimates ( $Z_{\text{DR}}$ ,  $\Phi_{\text{DP}}$ , and  $\rho_{\text{HV}}$ ) obtained when using PPC+. One example is observed in the area located at low elevation (meridional distance  $\leq 3$  km) and roughly 5 km from the radar. Using PPC+ that area has  $Z_{\text{DR}}$  values ranging between 0 and 2 dB and  $\rho_{\text{HV}}$  between 0.9 to 1. However, PPC incorrectly processed it as shoulders of a region (apparently smeared) right next to it (roughly at 7 km) with higher  $Z$ . Therefore, producing rays of constant  $Z_{\text{DR}}$ , and  $\rho_{\text{HV}}$  (changing in elevation) that do not match the recovered ones.

## 5.2 Improvement on the XPC Technique Based on a Calibration Strategy

One of the limitations related to the XPC technique is the bias introduced in the steering location of the  $H$  and  $V$  polarization patterns, termed angular mismatch. This bias is mainly observed when steering the array, and is detrimental to the performance of XPC. In this section, an improved version of the XPC technique is discussed. The improved XPC implements a calibration strategy to mitigate the angular mismatch effect.

The calibration strategy involves multiple calibration steps, which will be discussed in the next section. It does not propose a new calibration technique, but uses the ones discussed in the literature [91–94]. Generally, the calibration techniques proposed in the literature are based on correcting the amplitude and phase excitation on a per-element basis. Therefore, they can be jointly used with XPC as part of the same algorithm.

### 5.2.1 Methodology

The calibration strategy is herein considered part of the improved XPC technique. Calibration is performed in the following stages of the improved XPC algorithm.

- Stage 1: In this stage, the array patterns are measured in  $H$  and  $V$ . If there is an angular mismatch in any polarization, it will be corrected using calibration. Once the angular mismatch is mitigated, the number of canceler elements is calculated.

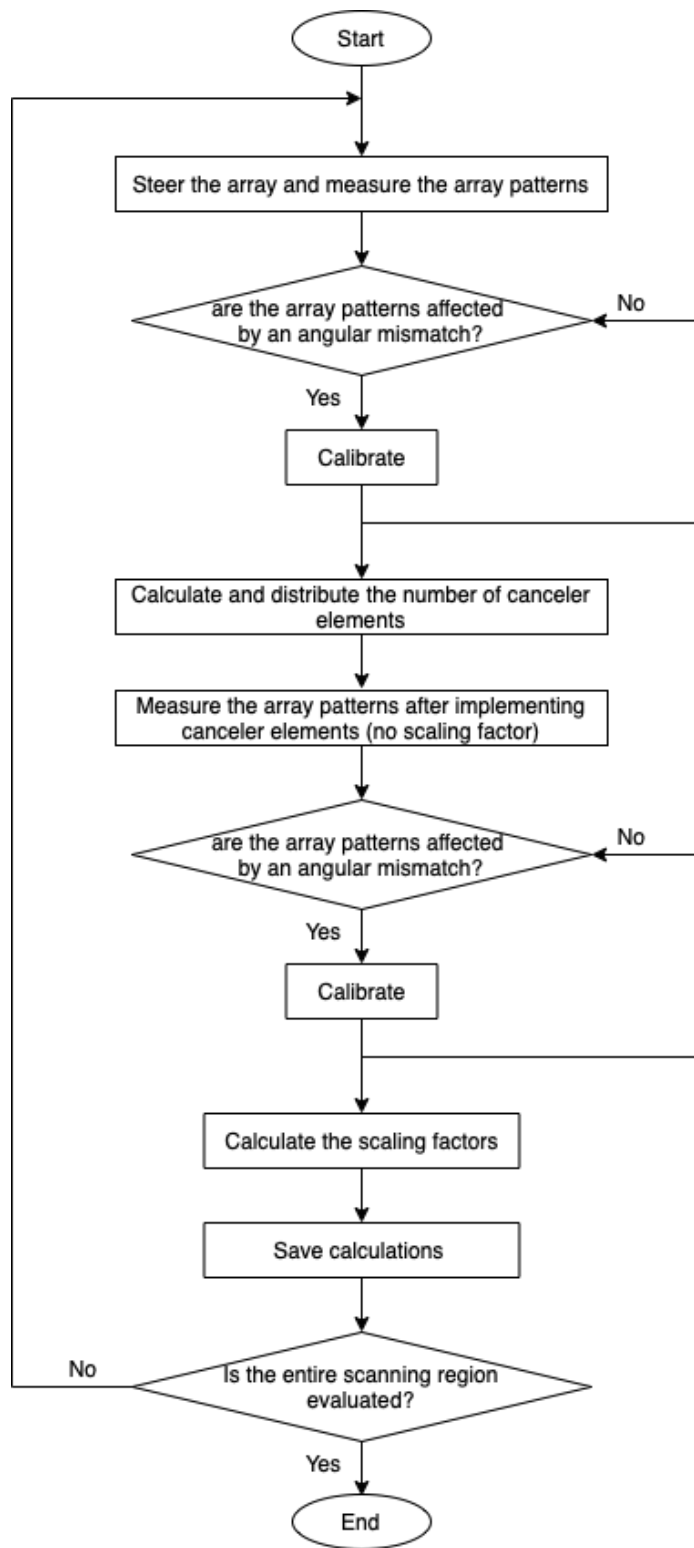


Figure 5.13: Flowchart corresponding to the improved XPC technique.

- Stage 2: In this stage, the canceler elements (no scaling factor) are implemented in the array, and the array patterns are measured. The use of canceler elements might induce an angular mismatch. Then, similar to stage 1, calibration is applied if there is an angular mismatch in the  $H$  or  $V$  patterns. After mitigating the angular mismatch, the scaling factors are calculated as explained in Chapter 3.

The improved XPC algorithm including the calibration strategy is illustrated in the flowchart presented in Figure 5.13.

Similarly, calibration is performed when implementing the calculated canceler elements and scaling factors in an operational PAR system. The system is considered calibrated if there are no observed angular mismatches. Calibration is performed before and after the calculations from XPC are implemented. The phased array radar system is calibrated before to mitigate the angular mismatch intrinsic to it and after to mitigate the mismatch caused by using XPC.

In the following section, The improved XPC technique using the proposed calibration strategies is evaluated using simulations. Additionally, the results from XPC with and without calibration are compared.

## 5.2.2 Results

The improved XPC technique will be implemented in the Horus all-digital phased array radar. In this section, the improved XPC was tested using simulation, designed identically to approach 2 in Section 4.3 and evaluated using the same parameters.

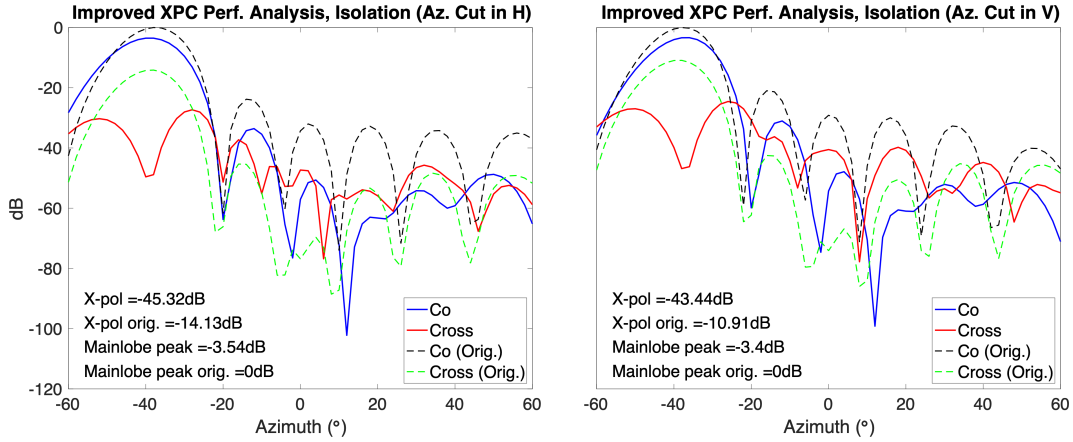


Figure 5.14: Evaluation of the improved XPC. The Array is steered  $-38^\circ$  in azimuth and  $18^\circ$  in elevation. Eleven elements are repurposed as cancelers. The scaling factors on these element are  $a = 0.41 + j52$  and  $b = 0.19 - j0.27$ . The cross-polar isolation is improved from 14.13 dB in  $H$  and 10.91 dB in  $V$ , to 45.32 dB in  $H$  and 43.44 dB  $V$ .

The improved XPC is first tested with the array pointing at  $-38^\circ$  in azimuth and  $18^\circ$  in elevation. Results are presented in Figure 5.14. It can be observed that the copolar peaks coincide with the steering angle. Additionally, the null in the cross-polar pattern produced by the improved XPC coincides with the angular location of the copolar peaks and the steering angle, producing better isolation.

Results in Figure 5.14 are compared to similar ones but processed with XPC as shown in Figure 5.15. It is observed that the improved XPC provides an extra 11.17 dB in isolation in  $V$  and 0.51 dB in  $H$ . The difference in the isolation improvement on  $H$  and  $V$  is related to the angular mismatch in each polarization. Concerning the main lobe peaks, it is observed that the improved XPC has a higher copolar loss. The different copolar losses are related to the number of canceler elements estimated with each method (eight in XPC and eleven in the improved XPC).

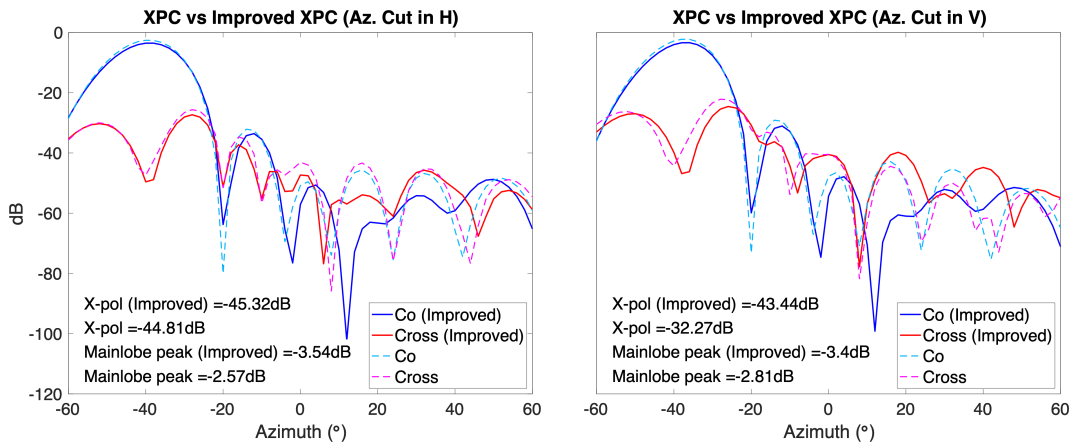


Figure 5.15: XPC and improved XPC results compared when the array is steered  $-38^\circ$  in azimuth and  $18^\circ$  in elevation. The improved XPC provides an extra 11.17 dB in isolation in  $V$  and 0.51 dB in  $H$ . However, the loss in the copolar gain on the improved XPC is higher (0.97 dB in  $H$  and 0.59 dB in  $V$ ).

In the previous example, the performance of the improved XPC at one angular location was evaluated. The following example (see Figure 5.16) evaluates the improved XPC performance based on the derived array patterns over the entire scanning region.

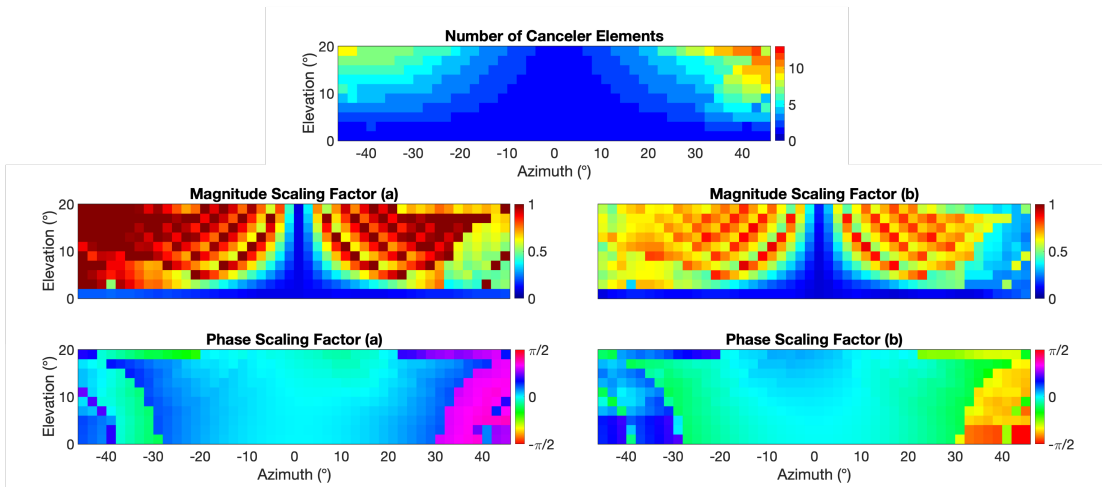


Figure 5.16: The calculated number of canceler elements and scaling factor on each steering position (approach 2), using the improved XPC technique. The number of elements (top) varies between 1 and 13. The magnitude of the scaling factor (middle) oscillates between zero and one. Finally, the phase of the scaling factor (bottom) is approximately zero radians except for the angles where calibration was necessary.



The calculated number of canceler elements and scaling factors as a function of steering angle are presented in Figure 5.16. It is observed that calibration impacts the number of canceler elements and the scaling factor. The impact is especially noticeable when comparing the results to the ones presented in Figure 4.16. Nevertheless, these results will vary depending on the array distribution and the elements used.

The improved XPC performance as a function of steering angle is presented in Figures 5.17 and 5.18. On average, the isolation is improved from 35.03 dB to 61.79 dB in  $H$  and 34.51 dB to 61.33 dB in  $V$ . Therefore, the extra improvement is approximately 23.75 dB in  $H$  and 23.73 dB in  $V$ . Concerning the array pattern purity (derived in Section 4.3), on average, it is improved from 93.85% to 99.69% in  $H$  (5.85% improvement) and 92.48% to 99.48 dB in  $V$  (7% improvement).

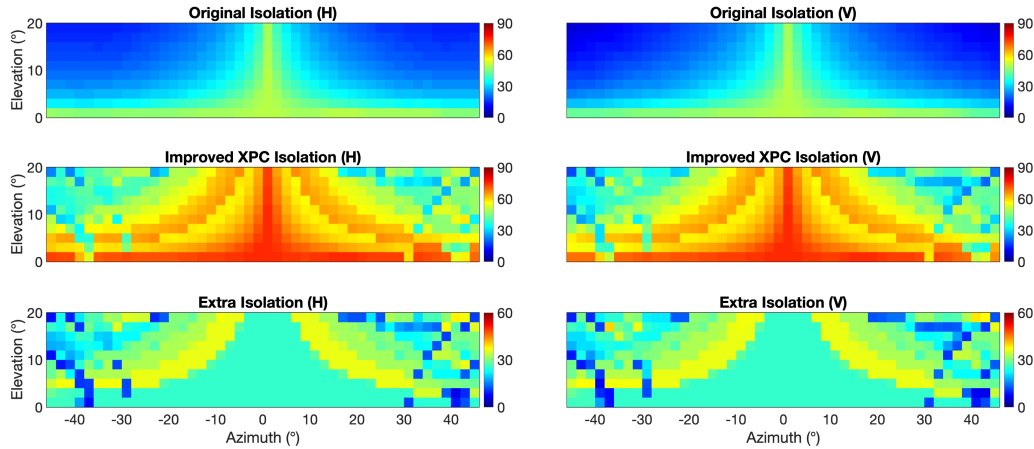


Figure 5.17: Improved XPC performance. The top two panels correspond to the original cross-polar isolation (in dB). In the middle panels, the improved cross-polar isolation is presented (in dB). Finally, in the bottom two panels, the extra cross-polar isolation (compared to the original one) is presented (in dB). The figure is divided into two columns. The left column corresponds to the results for the  $H$  polarization and the right for the  $V$  polarization.

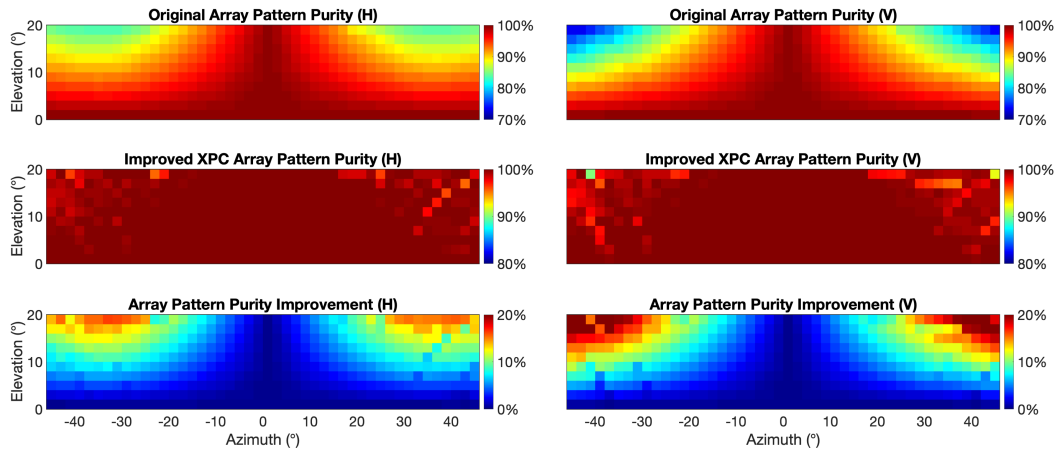


Figure 5.18: Similar to Figure 5.17, but for the array pattern purity, derived in Section 4.3 (in %).

From Figures 5.17 and 5.18, and compared to the previous results, the improved XPC seems to have similar performance as XPC (on average). XPC and its improved version have been implemented simultaneously on the same simulated array, and the results are compared side-by-side to evaluate the apparent lack of improvement (see Figure 5.19). On Figure 5.19, the XPC and improved XPC are compared based on the isolation in the  $H$  polarization. Similar behavior is expected when comparing the isolation in the  $V$  polarization and the array purity.

From Figure 5.19, it is observed that this lack of improvement is a by-product of the averaging. Using calibration in XPC improves the cross-polar isolation in regions where the angular mismatch is observed. For example, when steering from  $-45^\circ$  to  $-32^\circ$  in azimuth and  $0^\circ$  to  $10^\circ$  in elevation, calibration increases the cross-polar isolation as much as 20 dB. Additionally, the values in this region are similar to the ones where no angular mismatch is observable. Nevertheless, calibration is not perfect, and at some steering angles, the improved XPC performs worse than the XPC without it, affecting the overall performance. A future research path can involve the design of an improved calibration technique specifically designed for XPC. This enhanced cali-

bration is expected to improve the isolation, especially in scanning regions where the current method fails.

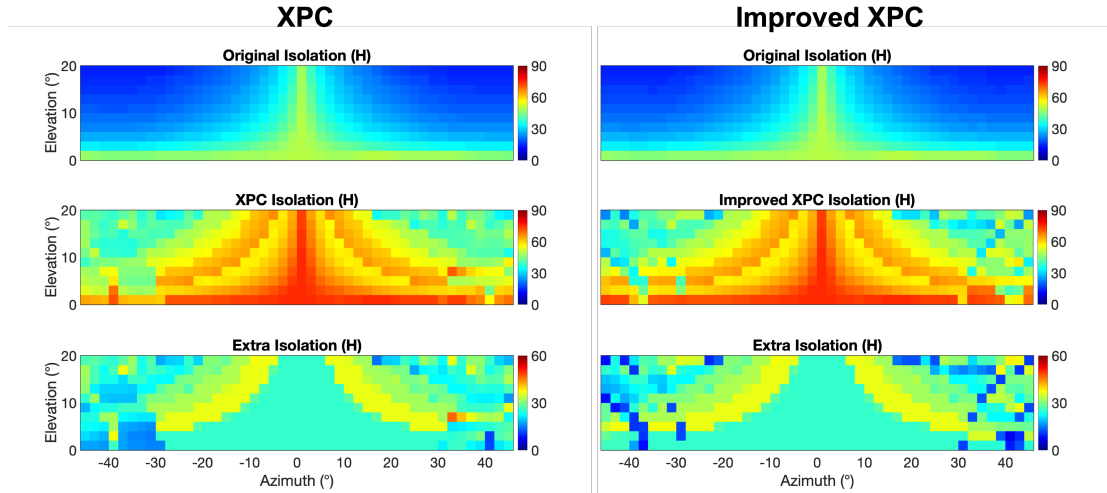


Figure 5.19: XPC (left panels) and improved XPC (right panels) performance based on the cross-polar isolation. The top two panels correspond to the original cross-polar isolation (in dB). In the middle panels, the improved cross-polar isolation, after implementing either XPC or its improved version, is presented (in dB). Finally, in the bottom two panels, it is presented the extra cross-polar isolation (in dB) from either XPC or its improved version (compared to the original one).

Concerning the loss in the copolar gain (see Figure 5.20), it behaves consistently to what was observed in Chapter 4. Therefore, the same conclusions hold. As a rough approximation, the loss can be assumed proportional to the number of canceler elements. Nonetheless, it also increases as the cross-polar contamination gets larger.

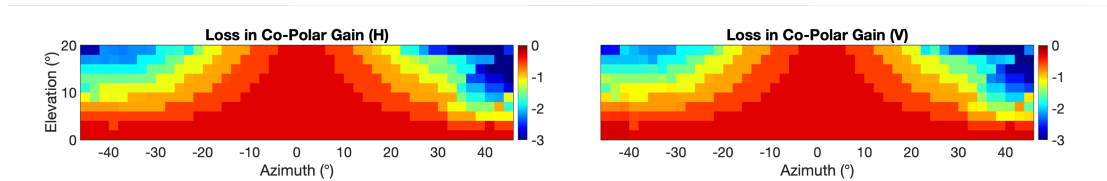


Figure 5.20: Loss in the copolar gain, as a function of steering angle, for the improved XPC. The left panel corresponds to the loss in  $H$  and the right to the one in  $V$ . It is approximately proportional to the number of canceler elements.

From the previous results, it has been shown that the calibration strategy imple-

mented in the improved XPC technique reduces the angular mismatch limitation described in Chapter 4.

### 5.3 Summary

In Chapter 5, two solutions were proposed for the practical implications and challenges related to the work in Chapters 3 and 4. The techniques are called PPC+ and improved XPC.

In the first part of the chapter, PPC+ was presented. PPC+ is an improved version of PPC developed to mitigate the “shoulder” effect observable inside the blind range. The PPC+ is based on PPC but uses a mismatched filter for compression. The mismatched filter is an amplitude-modulated version of the original matched filter. Then, a new calibration factor is calculated to include the effect of using the mismatched filter. PPC+ reduces the sidelobe levels that cause the shoulders, mitigating this issue. However, the solution has some drawbacks. It has lower sensitivity than PPC (nevertheless, it is still higher than fill pulse solutions), and the range resolution is compromised (a by-product of the amplitude modulation).

In the second part of the chapter, the improved XPC technique was presented. The improved XPC is based on the original XPC, but includes a calibration strategy to mitigate the angular mismatch (observed when steered off broadside). Calibration is performed at multiple stages of the improved XPC technique. Additionally, it is performed when the XPC calculations (number of canceler elements and scaling factors) are implemented in an operational phased array radar system. Implementing calibration increases the cross-polar isolation on the steering angles where an angular mismatch is observed. Based on simulations, at some steering angles, the improved XPC can produce as much as 20 dB of extra cross-polar isolation when compared to XPC. However,

the solution has some drawbacks. The calibration implemented in this chapter is based on previous work [91–94], rather than being designed for XPC. Therefore, at some steering angles, the improved XPC performs worse than XPC. The design of a new calibration method specifically tuned to be used on XPC is an interesting future research path to be explored.

In the next and final chapter, a summary of the different techniques discussed in this dissertation will be presented, and conclusions will be drawn from each. This dissertation has proposed solutions to two critical problems in solid-state phased array radars, e.g., blind range and cross-polar contamination. Nevertheless, even after the improvements discussed in this chapter, the proposed techniques have drawbacks to be mitigated. Future research paths to improve beyond the limitations discussed here, and throughout Chapters 3 and 4, will also be discussed in Chapter 6.

## **Chapter 6**

### **Epilogue**

#### **6.1 Discussion and Conclusions**

The PPC is a novel technique to mitigate the blind range observed in radars using pulse compression (see Chapter 3). It is resulted from the use of the long pulse, which produces long echoes. In general, the the leak-through signal from the transmission is much stronger than the return signals of targets. Therefore, the leak-through signal obscures all signals during the transmission cycle. However, targets inside the blind range return signals as long as the transmit pulse, So, there is an uncontaminated portion still available and can be used to correctly estimate the signals from the targets inside the blind region.

The PPC technique is divided into three steps. The first step is to discard all the received signals during the transmit cycle and apply a smooth taper for a continuous transition from zero to one. The second step is to perform the pulse compression using the “matched filter.” The combination of these two steps is equivalent to performing pulse compression using a progressively changing template to partially extract the uncontaminated received signal for compression. The third step is to compensate for the progressively changing template to estimate the obscured echoes correctly.

The PPC technique requires no hardware modification and, thus, can be applied to

many systems as a software update. All the necessary changes are within the receiving portion of the digital signal processor. There are no changes to the transmit portion of the software necessary.

The main advantage of the PPC techniques is an increase in the radar sensitivity inside the (old) blind range (transmission range). Radar sensitivity, as explained before, is proportional to the pulse width  $\tau$ . Unlike fill pulses, the PPC uses the uncontaminated tail portion of the returned pulse. Therefore, the usable pulse width  $\tau_u$  of the (new) uncontaminated received pulse gradually increases as the range  $r$  increases. Eventually, a full pulse is received outside the blind range, i.e., everything remains the same in the visible range.

On the downside, since the PPC technique uses the uncontaminated tail portion of the received signal, there is a loss in range resolution and shift of the compressed main lobe. The loss in resolution can be attributed to the use of the tail portion, which contains only a fraction of the transmitted bandwidth. This effect was numerically quantified and presented in Chapter 3. The shift of the compressed main lobe is simply a shift of the maximum gain when an incomplete echo (with different frequency and amplitude content) is processed with the matched filter.

Another limitation of the PPC technique is its effect on the range sidelobes for the targets inside the blind range. Sidelobes for those targets are not symmetrical, and those toward the radar can be extremely low (and higher away from the radar). Furthermore, for those targets, the sidelobe levels worsen as the target gets closer to the radar. More importantly, the higher sidelobes produce the “shoulder” effect, which effectively elongates the target, smearing the weather signals inside the blind range. Nevertheless, a mitigation strategy has been proposed in this dissertation and is presented in Chapter 5.

The PPC technique has been implemented on the PX-1000 system, and the real-time and archived radar images are available through a web portal

<https://radarhub.arrc.ou.edu>. In the near future, the PPC technique is expected to be implemented on the Horus phased array radar that the ARRC is currently developing.

The XPC is a technique developed to mitigate the cross-polar contamination on polarimetric all-digital phased array radars (see Chapter 4). It is a signal processing solution that takes advantage of the per-element amplitude and phase control (no hardware modifications) of the radar systems. The XPC technique distributes the elements on the array into two categories, the main and the canceler elements. The main elements transmit as intended. The canceler elements, however, transmit the inverse (i.e., the mathematical negative) scaled version of the original waveform in the perpendicular polarization (cross-polarization). After integration, the canceler elements nullify the cross-polarization generated by the main elements. The XPC has been developed for systems under STSR mode but can be applied to systems under ATSR mode.

The XPC techniques can be divided into two steps (see Section 4.1). The first step is to calculate the number of canceler elements. After that, they are distributed in the array. The canceler elements populate the edges of the array (starting at the corners) to minimize the impact on the sidelobes.

The number of canceler elements is calculated from the best solution to mitigate the cross-polar contamination. Nevertheless, the number of canceler elements is rounded to the next higher integer. A scaling factor is designed to minimize the impact on cross-polar mitigation caused by the rounding. The scaling factor is complex, changing in both magnitude and phase, and can be different on each polarization.

As explained, the XPC technique is developed for all-digital PAR systems. Nonetheless, it can be implemented on other PAR systems without hardware modifications as long as they have amplitude and phase control at a sub-array level.

The main advantage of XPC is that the number of canceler elements and scaling factors calculations are not fixed but are tuned depending on the cross-polar contami-



nation value at each steering angle inside the defined scanning region. Therefore, the XPC provides the maximum cross-polar isolation in all those steering angles. Assuming an ideal array (i.e., no fabrication error, diffraction, and ideal elements), XPC can fully mitigate the cross-polar contamination for the entire scanning region of an all-digital phased array radar system.

However, the XPC has some limitations that must be discussed. First, since fewer elements are transmitting as intended (some are repurposed as cancelers), the total gain of the array is lower. The more elements are used as canceler, the more significant the loss in the copolar gain is. A second factor contributing to the gain reduction is the inherent cross-polar isolation of the canceler elements, leaked into the copolarization. Nevertheless, the impact of the second factor is minor in comparison.

The second limitation is mainly due to the difference in the element patterns between  $H$  and  $V$ . Then, when an array is steered off-broadside, the array patterns may point in slightly different directions from each other and the steering angle (termed angular mismatch). The XPC calculations are based on the co- and cross-polar components of the array pattern at the steering location. Therefore, the mismatch affects the performance of XPC and the maximum achievable reduction in the cross-polar contamination. Even worse, XPC modifies the array (dividing it into main and canceler elements), affecting the angular mismatch. A mitigation strategy for the angular mismatch has been proposed in this dissertation and is presented in Chapter 5.

The XPC technique is planned to be implemented on the Horus radar system. Nonetheless, in the meantime, XPC has been successfully tested from simulations.

In Chapter 5, there were discussed improvements for the PPC (PPC+) and XPC (improved XPC). In the case of PPC, it has been proposed to pulse compress the ranges inside the modified transmission range with an amplitude-modulated version of the matched filter. The modulation changes as a function of range. Similarly, the XPC has

been improved by calibrating the arrays at different stages of the algorithm. PPC+ and the improved XPC are an evolution of the previous developments and are compatible with the same radar systems without hardware modifications.

The implementation of PPC+ is similar to PPC with an additional step, i.e., mismatched filters are used inside the transmission range. Outside the transmission range, the matched filter is not modulated.

The mismatched filters are designed by multiplying the matched filter by a range-dependent window. The first part of the window has as many zeroes as the modified received signal (range dependent). The remaining non-zero samples are tapered in amplitude. The aggressiveness of the taper will determine the effectiveness of the shoulder reduction. After compression, it is still necessary to apply a calibration factor. Of course, the calibration factor is calculated differently to include the effect of using a mismatched filter.

The main advantage of the PPC+ is the reduction of the shoulder levels and the shift of main lobe peak. However, using a mismatched filter negatively impacts the radar sensitivity and the range resolution. Both limitations are side effects of using amplitude modulation (tapering) to generate the mismatched filter. A future research opportunity to mitigate these limitations is to design an improved mismatched filter based on phase modulation instead. It is theorized that a phase modulation could produce the same reduced shoulder levels without the downsides of tapering.

The PPC+ technique can be implemented on the PX-1000 as a software update of the existing PPC algorithm. Experimental results processed using data from the PX-1000 have been generated and presented in Section 5.1.4.

On a related note, the implementation of the improved XPC is similar to original XPC. Calibration is included as a component of the technique. First, calibration is performed before the number of canceler elements is calculated. Then calibration is per-

formed after implementing the canceler elements in the array but before calculating the scaling factor. Additionally, calibration is performed before and after implementing the XPC calculations (number of canceler elements and scaling factors) in an operational phased array system. Calibration is not always applied. Calibration is only performed at the steering angles affected by an angular mismatch.

Using calibration combined with XPC mitigates the angular mismatch and improves the cross-polar isolation. However, the current calibration approach has some drawbacks. At some steering angles, the cross-polar isolation obtained from the original XPC can be significantly higher than the improved XPC. One hypothesis is the limitation of the current calibration approach, which was adopted from literature [91–94]. It does not always correct the imperfections caused by the XPC. A potential future research includes designing a calibration algorithm tuned for the XPC, which could enhance the improved XPC technique independent of the steering angle.

## **6.2 Future Work**

The work proposed in this dissertation includes two novel techniques for solid-state PAR systems. That is, a blind range mitigation through the PPC+ and cross-polar isolation improvement through the improved XPC technique. Nevertheless, the techniques are not exempted from limitations (see Sections 3.2.2, 4.2.2, 5.1.3 and 5.2.2). In this section, the author discusses future research opportunities to mitigate those limitations and, in general, to improve PPC+ and XPC.

- As explained in Section 5.1.3, a mismatched filter modulated in amplitude can significantly mitigate the shoulder effect and the main lobe peak migration. However, amplitude modulation negatively impacts the radar sensitivity inside the transmission range and the range resolution of the compressed signal. A potential

future research topic is the design of the matched filter using phase modulation. The phase modulation does not require tapering the mismatched filter. Therefore, the radar sensitivity and range resolution will be identical to the original PPC. A design alternative is to use an optimization approach similar to the one presented by Kurdzo [6] and Kurdzo *et al.* [38].

- It is hypothesized that changing the modulation of the transmitted waveform may also mitigate the shoulder effect and the main lobe peak migration. Then, a second future research path to improve PPC+ is to design a new frequency modulated waveform based on optimization techniques [6, 38]. The optimization process can include the mismatched filter as one of its parameters.
- Finally, as described in this dissertation, the PPC and PPC+ techniques have been tested on radars using reflector antennas (i.e., PX-1000). Nevertheless, they can be implemented on PARs as well. Further experimentation on PPC and PPC+ on PARs is proposed as future work. Additionally, future research includes the implementation of PPC+ on the Horus all-digital PAR system as a software update.
- Concerning the XPC and improved XPC techniques, the scaling factors are calculated from Equations (4.35) and (4.36). However, the equations have multiple solutions of  $a$  and  $b$ . One such solution is presented in Section 4.1.2. It should be emphasized that, in some instances, the solution may produce a scaling factor with a magnitude slightly larger than one, which is then normalized to unity by the algorithm, which has a negative impact on the performance of XPC. A future research path is to optimize the solution of  $a$  and  $b$  that provide the best isolation and bounded to the constraint that  $|a| \leq 1$  and  $|b| \leq 1$ . This research opportunity is not directly related to the limitations defined at the beginning of the section, but it is an important practical improvement of the XPC.

- Additionally, in Chapter 5, it has been shown, from simulations, that the use of calibration to mitigate the angular mismatch improves the performance of the XPC (improved XPC). Nevertheless, at some steering locations, the original XPC produces better results without it (see Section 5.2.2). It is hypothesized that this issue is related to the calibration algorithm implemented. A research opportunity to further improve XPC is to develop a new calibration algorithm specific to the XPC. The new calibration algorithm must analyze and correct the imperfections caused by changing the elements to canceler mode and their impact on the array patterns.
- Finally, in this dissertation, the XPC technique, and its improved version, have been evaluated using simulations from an  $8 \times 8$  array populated with crossed-dipole elements. Nevertheless, in the future, the XPC technique should be evaluated using simulations from larger arrays and different element technologies. More importantly, after the Horus system is completed, the XPC will be implemented on that system, and its performance will be evaluated from experimental data.

## References

- [1] M. I. Skolnik, *Introduction to Radar Systems, Third Edition*. McGraw-Hill Professional, 2001.
- [2] R. J. Doviak and D. Zrníc, *Doppler Radar and Weather Observations*. Dover Publications, Inc., 1993.
- [3] W. H. Heiss, D. L. McGrew, and D. Sirmans, “NEXRAD - Next Generation Weather Radar (WSR-88D),” *Microwave Journal*, vol. 33, p. 79, 1990.
- [4] D. Schwartzman, “Signal Processing Techniques and Concepts of Operations for Polarimetric Rotating Phased Array Radar,” Available at <https://shareok.org/handle/11244/326580>, Ph.D. dissertation, The University of Oklahoma, Norman, OK, USA, 2020.
- [5] N. R. Council, *Weather Radar Technology Beyond NEXRAD*. Washington, DC: The National Academies Press, 2002. DOI: 10.17226/10394.
- [6] J. Kurdzo, “Pulse Compression Waveforms and Applications for Weather Radar,” Available at <https://shareok.org/handle/11244/23250>, Ph.D. dissertation, The University of Oklahoma, Norman, OK, USA, 2015.

- [7] D. S. Zrníc and A. V. Ryzhkov, "Polarimetry for Weather Surveillance Radars," *Bulletin of the American Meteorological Society*, vol. 80, no. 3, pp. 389–406, Mar. 1999. DOI: 10.1175/1520-0477(1999)080<0389:PFWSR>2.0.CO;2.
- [8] P. H. Herzegh and A. R. Jameson, "Observing Precipitation through Dual-Polarization Radar Measurements," *Bulletin of the American Meteorological Society*, vol. 73, no. 9, pp. 1365–1376, 1992. DOI: 10.1175/1520-0477(1992)073<1365:OPTDPR>2.0.CO;2.
- [9] P. M. Stepanian, K. G. Horton, V. M. Melnikov, D. S. Zrníc, and S. A. Gauthreaux Jr, "Dual-Polarization Radar Products for Biological Applications," *Ecosphere*, vol. 7, no. 11, e01539, 2016.
- [10] E. Sarreals, "NEXRAD Products and Operational Capability," in *25th AIAA Aerospace Sciences Meeting*, 1987, p. 627.
- [11] J. H. Golden, "The Prospects and Promise of NEXRAD: 1990's and Beyond," in *Weather Radar Networking*, Springer, 1990, pp. 26–45.
- [12] S. M. Torres, Y. F. Dubel, and D. S. Zrníc, "Design, Implementation, and Demonstration of a Staggered PRT Algorithm for the WSR-88D," *Journal of Atmospheric and Oceanic Technology*, vol. 21, no. 9, pp. 1389–1399, 2004. DOI: 10.1175/1520-0426(2004)021<1389:DIADOA>2.0.CO;2.
- [13] W. D. Zittel, D. Saxion, R. Rhoton, and D. C. Crauder, "P2. 9 Combined WSR-88D Technique To Reduce Range Aliasing Using Phase Coding and Multiple Doppler Scans," 2008.

- [14] L. J. Battan, "Duration of Tornadoes," *Bulletin of the American Meteorological Society*, vol. 40, no. 7, pp. 340–342, 1959. DOI: 10.1175/1520-0477-40.7.340.
- [15] J. N. Chrisman, "Automated Volume Scan Evaluation and Termination (AVSET)," in *34th Conference on Radar Meteorology*, 2009.
- [16] —, "Supplemental Adaptive Intra-Volume Low-Level Scan (SAILS)," *ROC Engineering*, NOAA, 2011.
- [17] E. Brookner, "Phased Array Radars - Past, Present and Future," English, *IET Conference Proceedings*, 104–113(9), Jan. 2002.
- [18] D. E. Forsyth *et al.*, "The National Weather Radar Testbed (Phased-Array)," in *32nd Conference on Radar Meteorology*, 2005, pp. 24–29.
- [19] D. Zrnica *et al.*, "Agile-Beam Phased Array Radar for Weather Observations," *Bulletin of the American Meteorological Society*, vol. 88, no. 11, pp. 1753–1766, 2007.
- [20] A. P. Hopf *et al.*, "CASA Phased Array Radar System Description, Simulation and Products," in *2009 IEEE International Geoscience and Remote Sensing Symposium*, vol. 2, 2009, pp. II-968-II-971. DOI: 10.1109/IGARSS.2009.5418262.
- [21] P. L. Heinselman and S. M. Torres, "High-Temporal-Resolution Capabilities of the National Weather Radar Testbed Phased-Array Radar," *Journal of Applied Meteorology and Climatology*, vol. 50, no. 3, pp. 579–593, 2011.
- [22] B. Isom *et al.*, "The Atmospheric Imaging Radar: Simultaneous Volumetric Observations Using a Phased Array Weather Radar," English, *Journal of Atmo-*



- spheric and Oceanic Technology*, vol. 30, no. 4, pp. 655–675, Apr. 2013. DOI: 10.1175/JTECH-D-12-00063.1.
- [23] S. Torres *et al.*, “8.2 New Weather-Surveillance Capabilities for NSSL’S Phased-Array Radar,” 2013.
- [24] E. Yoshikawa *et al.*, “MMSE Beam Forming on Fast-Scanning Phased Array Weather Radar,” *IEEE Transactions on Geoscience and Remote Sensing*, vol. 51, no. 5, pp. 3077–3088, 2013. DOI: 10.1109/TGRS.2012.2211607.
- [25] J. L. Salazar *et al.*, “An Ultra-Fast Scan C-band Polarimetric Atmospheric Imaging Radar (PAIR),” in *2019 IEEE International Symposium on Phased Array System and Technology (PAST)*, 2019, pp. 1–5. DOI: 10.1109/PAST43306.2019.9021042.
- [26] C. Fulton *et al.*, “Horus: A Testbed for Fully Digital Phased Array Radars,” *Microwave Journal*, vol. 63, no. 1, pp. 20–20, 22, Jan. 2020.
- [27] R. Palmer *et al.*, “A Primer on Phased Array Radar Technology for the Atmospheric Sciences,” *Bulletin of the American Meteorological Society*, 2022. DOI: 10.1175/BAMS-D-21-0172.1.
- [28] R. Mailloux, *Phased Array Antenna Handbook, Third Edition*. 2017.
- [29] D. Schwartzman, S. M. Torres, and T.-Y. Yu, “Distributed Beams: Concept of Operations for Polarimetric Rotating Phased Array Radar,” *IEEE Transactions on Geoscience and Remote Sensing*, vol. 59, no. 11, pp. 9173–9191, 2021. DOI: 10.1109/TGRS.2020.3047090.

- [30] ———, “Integration of the Motion-Compensated Steering and Distributed Beams’ Techniques for Polarimetric Rotating Phased Array Radar,” *IEEE Geoscience and Remote Sensing Letters*, vol. 19, pp. 1–5, 2022. DOI: 10.1109/LGRS.2021.3113564.
- [31] D. Schwartzman, J. D. Díaz Díaz, J. L. Salazar-Cerreño, T.-Y. Yu, R. D. Palmer, and M. S. McCord, “A Hybrid Antenna Pattern Synthesis Method for the Polarimetric Atmospheric Imaging Radar (PAIR),” in *2022 IEEE Radar Conference (RadarConf22)*, 2022, pp. 01–06. DOI: 10.1109/RadarConf2248738.2022.9764359.
- [32] D. Hoft and L. Lavallee, “RF Power Modules for L-Band Solid State Transmitters,” in *1974 Antennas and Propagation Society International Symposium*, vol. 12, 1974, pp. 417–419. DOI: 10.1109/APS.1974.1147241.
- [33] R. D. Palmer, C. J. Fulton, J. Salazar, H. Sigmarsson, and M. Yearly, “The “Horus” Radar—an All-Digital Polarimetric Phased Array Radar for Multi-Mission Surveillance,” in *99th American Meteorological Society Annual Meeting*, AMS, 2019.
- [34] R. Palmer *et al.*, “Horus – A Polarimetric Digital Phased Array Weather Radar Developed at the University of Oklahoma,” in *2022 IEEE International Symposium on Phased Array Systems and Technology*, vol. Accepted, 2022.
- [35] R. J. Keeler and C. A. Hwang, “Pulse Compression for Weather Radar,” in *Proceedings International Radar Conference*, 1995, pp. 529–535. DOI: 10.1109/RADAR.1995.522603.

- [36] A. Mudukutore, V. Chandrasekar, and R. Keeler, "Pulse Compression for Weather Radars," *IEEE Transactions on Geoscience and Remote Sensing*, vol. 36, no. 1, pp. 125–142, 1998. DOI: 10.1109/36.655323.
- [37] E. D. Witte and H. Griffiths, "Improved Ultra-Low Range Sidelobe Pulse Compression Waveform Design," English, *Electronics Letters*, vol. 40, 1448–1450(2), 22 2004.
- [38] J. M. Kurdzo, B. L. Cheong, R. D. Palmer, G. Zhang, and J. B. Meier, "A Pulse Compression Waveform for Improved-Sensitivity Weather Radar Observations," *Journal of Atmospheric and Oceanic Technology*, vol. 31, no. 12, pp. 2713–2731, 2014. DOI: 10.1175/JTECH-D-13-00021.1.
- [39] C. Salazar, B. Cheong, and R. D. Palmer, "Progressive Pulse Compression: A Novel Technique for Blind Range Recovery for Solid-State Radars," *Journal of Atmospheric and Oceanic Technology*, vol. 38, no. 9, pp. 1599–1611, 2021. DOI: 10.1175/JTECH-D-20-0164.1.
- [40] F. O'Hora and J. Bech, "Improving Weather Radar Observations Using Pulse-Compression Techniques," *Meteorological Applications*, vol. 14, pp. 389–401, 2007. DOI: 10.1002/met.38.
- [41] J. George, N. Bharadwaj, and V. Chandrasekar, "Considerations in Pulse Compression Design for Weather Radars," in *IGARSS 2008 - 2008 IEEE International Geoscience and Remote Sensing Symposium*, vol. 5, 2008, pp. V - 109-V –112. DOI: 10.1109/IGARSS.2008.4780039.

- [42] J. George, K. V. Mishra, C. M. Nguyen, and V. Chandrasekar, "Implementation of Blind Zone and Range-Velocity Ambiguity Mitigation for Solid-State Weather Radar," in *2010 IEEE Radar Conference*, 2010, pp. 1434–1438. DOI: 10.1109/RADAR.2010.5494392.
- [43] N. Bharadwaj and V. Chandrasekar, "Wideband Waveform Design Principles for Solid-State Weather Radars," *J. Atmos. Oceanic Technol.*, vol. 29(1), pp. 14–31, 2012. DOI: <https://doi.org/10.1175/JTECH-D-11-00030.1>.
- [44] B. L. Cheong, K. Redmond, R. D. Palmer, Y. Zhang, M. Yeary, and T.-Y. Yu, "PX-1000: A Solid-State Polarimetric X-Band Weather Radar and Time-Frequency Multiplexed Waveform for Blind Range Mitigation," *IEEE Trans. Instrum. Meas.*, vol. 62(11), pp. 3064–3072, 2013. DOI: 0.1109/TIM.2013.2270046.
- [45] C. M. Nguyen and V. Chandrasekar, "Sensitivity Enhancement System for Pulse Compression Weather Radar," *Journal of Atmospheric and Oceanic Technology*, vol. 31, no. 12, pp. 2732–2748, 2014. DOI: 10.1175/JTECH-D-14-00049.1.
- [46] C. Fulton *et al.*, "Dual-Polarization Challenges in Weather Radar Requirements for Multifunction Phased Array Radar," in *2013 IEEE International Symposium on Phased Array Systems and Technology*, 2013, pp. 494–501. DOI: 10.1109/ARRAY.2013.6731878.
- [47] C. Salazar, D. Schwartzman, B. L. Cheong, and R. D. Palmer, "Cross-Polar Canceller (XPC): A Technique to Reduce Cross-Polar Pattern Contamination in Polarimetric Weather Observations," in *2022 IEEE International Symposium on Phased Array Systems and Technology*, vol. Accepted, 2022.

- [48] I. R. Ivić and D. Schwartzman, “A First Look at the ATD Data Corrections,” in *Proc. 39th Int. Conf. Radar Meteorol.*, 2019, pp. 2–6.
- [49] C. Salazar, D. Schwartzman, B. L. Cheong, and R. D. Palmer, “Signal Processing Technique to Increase Cross-Polar Isolation on Fully Digital Phased Array Radars,” in *2022 IEEE Radar Conference (RadarConf22)*, 2022, pp. 1–6. DOI: 10.1109/RadarConf2248738.2022.9764360.
- [50] J. D. Díaz *et al.*, “A Cross-Stacked Radiating Antenna With Enhanced Scanning Performance for Digital Beamforming Multifunction Phased-Array Radars,” *IEEE Transactions on Antennas and Propagation*, vol. 66, no. 10, pp. 5258–5267, 2018. DOI: 10.1109/TAP.2018.2862252.
- [51] M. Sánchez-Barbety, R. W. Jackson, and S. Frasier, “Interleaved Sparse Arrays for Polarization Control of Electronically Steered Phased Arrays for Meteorological Applications,” *IEEE Transactions on Geoscience and Remote Sensing*, vol. 50, no. 4, pp. 1283–1290, 2012. DOI: 10.1109/TGRS.2011.2167016.
- [52] M. Yeary, D. Conway, J. Herd, M. Fosberry, M. Harger, and K. Hondl, “A Method for Improved Cross-pol Isolation Based on the Use of Auxilliary Elements,” in *2013 IEEE International Symposium on Phased Array Systems and Technology*, 2013, pp. 272–275. DOI: 10.1109/ARRAY.2013.6731840.
- [53] D. S. Zrnić, R. J. Doviak, V. M. Melnikov, and I. R. Ivić, “Signal Design to Suppress Coupling in the Polarimetric Phased Array Radar,” *Journal of Atmospheric and Oceanic Technology*, vol. 31, no. 5, pp. 1063–1077, 2014. DOI: 10.1175/JTECH-D-13-00037.1.

- [54] Y. Li, Z. Wang, C. Pang, and X. Wang, "A Low Cross-Polarization Configuration Method for Phased Array Radar Antenna," *Electronics*, vol. 9, no. 3, 2020. DOI: 10.3390/electronics9030396.
- [55] L. Pralon, B. Pompeo, G. Beltrao, H. Cioqueta, B. Cosenza, and J. Moreira, "On a Blind Zone Elimination Method Based on Partial Compression Filter Design Using Random Waveforms for Monostatic Pulsed Radars," in *IET International Conference on Radar Systems (Radar 2012)*, 2012, pp. 1–5. DOI: 10.1049/cp.2012.1653.
- [56] D. Lamper and T. L. Grettenberg, *Pulse compression technique for high duty factor radar*, US Patent 5,036,324, Jul. 1991.
- [57] J. H. McClellan, R. W. Schafer, and M. A. Yoder, *Signal Processing First*. Pearson education Upper Saddle River, NJ, 2003.
- [58] S. K. Mitra and Y. Kuo, *Digital Signal Processing: a Computer-Based Approach*. McGraw-Hill New York, 2006, vol. 2.
- [59] S. M. Torres, "19.2 range and velocity ambiguity mitigation on the wsr-88d: Performance of the sz-2 phase coding algorithm," 2005.
- [60] S. Haykin, *Adaptive Radar Signal Processing*. John Wiley & Sons, 2007.
- [61] R. Palmer *et al.*, "Atmospheric Radar Research Center-ARRC University of Oklahoma, USA," *IEEE Geoscience and Remote Sensing Newsletter*, no. 142, pp. 10–16, 2007.

- [62] S. Torres, R. Passarelli Jr, A. Siggia, and P. Karhunen, “Alternating Dual-Pulse, Dual-Frequency Techniques for Range and Velocity Ambiguity Mitigation on Weather Radars,” *Journal of Atmospheric and Oceanic Technology*, vol. 27, no. 9, pp. 1461–1475, 2010.
- [63] J. Bae, *Adaptive Waveforms for Automatic Target Recognition and Range-Doppler Ambiguity Mitigation in Cognitive Sensor*. The University of Arizona, 2013.
- [64] M. A. Richards, *Fundamentals of Radar Signal Processing, Second Edition, Second Edition*. McGraw-Hill Education, 2014.
- [65] J. R. Probert-Jones, “The radar equation in meteorology,” *Quarterly Journal of the Royal Meteorological Society*, vol. 88, no. 378, pp. 485–495, 1962. DOI: <https://doi.org/10.1002/qj.49708837810>.
- [66] L. J. Battan, “Radar observation of the atmosphere,” *Quarterly Journal of the Royal Meteorological Society*, vol. 99, no. 422, pp. 793–793, 1973. DOI: <https://doi.org/10.1002/qj.49709942229>.
- [67] A. V. Ryzhkov and D. S. Zrnich, *Radar Polarimetry for Weather Observations*. Springer Atmospheric sciences, 2019.
- [68] H. Wang, Z. Shi, and J. He, “Compression with considerable sidelobe suppression effect in weather radar,” *EURASIP Journal on Wireless Communications and Networking*, vol. 2013, no. 1, pp. 1–8, 2013.

- [69] V. Galushko, “On application of taper windows for sidelobe suppression in lfm pulse compression,” in *2020 IEEE Ukrainian Microwave Week (UkrMW)*, IEEE, 2020, pp. 995–1001.
- [70] P. Kollias *et al.*, “Science Applications of Phased Array Radars,” *Bulletin of the American Meteorological Society*, 2022. DOI: 10.1175/BAMS-D-21-0173.1.
- [71] H. J. Visser, *Array and Phased Array Antenna Basics*. John Wiley & Sons, Ltd, 2005. DOI: <https://doi.org/10.1002/0470871199>.
- [72] C. A. Balanis, *Antenna Theory: Analysis and Design*. John Wiley & Sons, 2015, p. 1072.
- [73] A. K. Bhattacharyya, *Phased array antennas: Floquet analysis, synthesis, BFNs and active array systems*. John Wiley & Sons, 2006.
- [74] M. Longbrake, “True Time-Delay Beamsteering for Radar,” in *2012 IEEE National Aerospace and Electronics Conference (NAECON)*, 2012, pp. 246–249. DOI: 10.1109/NAECON.2012.6531062.
- [75] D. Pozar and B. Kaufman, “Design Considerations for Low Sidelobe Microstrip Arrays,” *IEEE Transactions on Antennas and Propagation*, vol. 38, no. 8, pp. 1176–1185, 1990. DOI: 10.1109/8.56953.
- [76] H. Steyskal and J. Herd, “Mutual Coupling Compensation in Small Array Antennas,” *IEEE Transactions on Antennas and Propagation*, vol. 38, no. 12, pp. 1971–1975, 1990. DOI: 10.1109/8.60990.



- [77] J. S. Williams, *Electronic Scanned Array Design*. Institution of Engineering and Technology (The IET), 2020.
- [78] J. L. Salazar, N. Aboserwal, J. D. Díaz, J. A. Ortiz, and C. Fulton, “Edge Diffractions Impact on the Cross Polarization Performance of Active Phased Array Antennas,” in *2016 IEEE International Symposium on Phased Array Systems and Technology (PAST)*, 2016, pp. 1–5. DOI: 10.1109/ARRAY.2016.7832571.
- [79] J. A. Ortiz, N. Aboserwal, and J. L. Salazar, “A New Analytical Model Based on Diffraction Theory for Predicting Cross-polar Patterns of Antenna Elements in a Finite Phased Array,” in *2019 IEEE International Symposium on Phased Array System & Technology (PAST)*, 2019, pp. 1–4. DOI: 10.1109/PAST43306.2019.9020757.
- [80] J. A. Ortiz, “Impact of Edge Diffraction in Dual-Polarized Phased Array Antennas,” Available at <https://shareok.org/handle/11244/325369>, Ph.D. dissertation, The University of Oklahoma, Norman, OK, USA, 2020.
- [81] V. N. Bringi and V. Chandrasekar, *Polarimetric Doppler Weather Radar: Principles and Applications*. Cambridge University Press, 2001. DOI: 10.1017/CBO9780511541094.
- [82] D. Zrnić, R. Doviak, G. Zhang, and A. Ryzhkov, “Bias in Differential Reflectivity due to Cross Coupling Through the Radiation Patterns of Polarimetric Weather Radars,” *Journal of Atmospheric and Oceanic Technology*, vol. 27, no. 10, pp. 1624–1637, 2010. DOI: 10.1175/2010JTECHA1350.1.

- [83] I. R. Ivić, “An Approach to Simulate the Effects of Antenna Patterns on Polarimetric Variable Estimates,” *Journal of Atmospheric and Oceanic Technology*, vol. 34, no. 9, pp. 1907–1934, 2017. DOI: 10.1175/JTECH-D-17-0015.1.
- [84] C. Salazar, R. D. Palmer, and B. L. Cheong, “Methods and Apparatus for Blind Range Recovery on Pulse Compression Radars,” US Patent 11,313,959, Apr. 2022.
- [85] N. Levanon and E. Mozeson, *Radar Signals*, 1st Edition. John Wiley and Sons Inc., 2004.
- [86] F. Junyent, V. Chandrasekar, D. McLaughlin, E. Insanic, and N. Bharadwaj, “The CASA Integrated Project 1 Networked Radar System,” *J. Atmos. Oceanic Technol.*, vol. 27(1), pp. 61–78, 2010. DOI: <https://doi.org/10.1175/2009JTECHA1296.1>.
- [87] A. Ryzhkov *et al.*, “Quasi-vertical profiles—A new way to look at polarimetric radar data,” *Journal of Atmospheric and Oceanic Technology*, vol. 33, no. 3, pp. 551–562, 2016.
- [88] D. Schwartzman and S. Torres, “Design of Practical Pulse Compression Waveforms for Polarimetric Phased Array Radar,” in *Proc. 39th Int. Conf. Radar Meteorol.*, 2019, pp. 1–9.
- [89] J. Kaimal and L. Kristensen, “Time Series Tapering for Short Data Samples,” *Boundary-layer meteorology*, vol. 57, no. 1, pp. 187–194, 1991.

- [90] P. Bloomfield, *Fourier Analysis of Time Series: an Introduction*. John Wiley & Sons, 2004.
- [91] C. Fulton and W. J. Chappell, “Calibration of a Digital Phased Array for Polarimetric Radar,” in *2010 IEEE MTT-S International Microwave Symposium*, IEEE, 2010, pp. 161–164.
- [92] R. Lebrón, J. D. Díaz, and J. L. Salazar-Cerreno, “A Procedure to Characterize and Predict Active Phased Array Antenna Radiation Patterns from Planar Near-Field Measurements,” in *2018 AMTA Proceedings*, IEEE, 2018, pp. 1–4.
- [93] R. Lebron Garcia, “Techniques and Instrumentation for Phased Array Calibration,” 2020.
- [94] D. Schvartzman, J. Diaz-Diaz, R. Palmer, C. F. D. Zrnić, and P. K. J. Salazar-Cerreno, “A Polarimetric Antenna-Calibration Method for the Horus Radar based on E-Field Back Projection,” in *2022 IEEE International Symposium on Phased Array Systems and Technology*, 2022.

## Appendix A

### Acronyms

**ARRC** Advanced Radar Research Center

**ATSR** Alternate transmission and simultaneous reception of *H/V* polarization

**HFSS** High-frequency structure simulations

**LFM** Linear Frequency modulation

**LPC** Legacy pulse compression

**MPA** Microstrip patch antenna

**MPAR** Multi-function phased array radar

**NEXRAD** Next Generation Weather Radar

**NLFM** Non-linear Frequency modulation

**NOAA** National Oceanic and Atmospheric Administration

**NWS** National Weather Service

**OFM** Optimized frequency modulation

**OU** The University of Oklahoma

**PAR** Phased array radar

**PC** Pulse compression

**PPC** Progressive pulse compression

**PPC+** Improved progressive pulse compression

**PPI** Plan position indicator

**PRT** Pulse repetition time

**QVP** Quasi-vertical profiles

**RHI** Range height indicator

**STSR** Simultaneous transmission and simultaneous reception of  $H/V$  polarization

**TFM** Time-frequency multiplexed waveform

**VCP** Volume coverage pattern

**WSR-88D** Weather Surveillance Radar - 88 Doppler

**XPC** Cross-polar canceler

## Index

- Angular mismatch, 17, 88–91, 98, 99,  
101, 102, 106, 125, 127, 128,  
131, 133, 138, 140, 142
- Beam steering, 7, 12, 15, 29, 32,  
34–36, 39, 89, 125  
Steering angle, 34, 35, 37–43, 77,  
78, 87, 88, 93–95, 98, 99, 101,  
102, 104, 125, 128–132, 138,  
140, 142
- Blind range, 6–10, 12, 14–17, 28, 51,  
53, 55, 57–61, 63–65, 67–70,  
72, 106–108, 135, 136, 140  
Transmission range, 108, 110, 111,  
113–116, 119, 121, 122, 124  
Visible range, 9, 10, 12, 14, 60, 68,  
69, 72, 106, 108, 136
- Copolar  
Bias, 7  
Gain, 84, 87, 92, 95, 98, 101, 103,  
104, 128, 129, 132, 138  
Pattern, 47, 76, 88, 97, 128
- Cross-Polar Canceler (XPC)  
Canceler element, 16, 75–79, 81,  
84, 85, 87, 88, 91–96, 98, 99,  
101, 102, 104, 125, 127–130,  
132, 138–140, 142  
Canceler element location, 16, 84,  
85  
Scaling factor, 13, 16, 76–79, 84,  
85, 87, 88, 91–96, 98, 99, 101,  
102, 127–130, 137, 140, 141
- Cross-polar contamination, 7, 8, 12–16,  
46, 75–77, 79, 87, 92, 95–97,  
101, 104, 132, 137, 138
- Cross-polar isolation, 12–14, 16, 45,  
79, 87, 90–96, 99, 100, 102,  
104, 138
- Diffraction, 44, 45, 77, 88, 93, 101, 138

Grating lobes, 39–43

Horus, 16, 75, 92, 127, 137, 138, 141, 142

Improved Cross-Polar Canceler (XPC) technique  
 Calibration, 17, 106, 125, 127, 129–132, 139, 140, 142

Improved Progressive Pulse Compression (PPC+)  
 Mismatched Filter, 17, 106, 111–114, 116, 119–122, 139–141  
 Calibration factor, 114, 139  
 Phase modulation, 121, 139, 141  
 Roll-off factor, 112, 115, 117, 120, 121  
 Tapering, 111, 112, 114, 115, 119, 121, 135, 139, 141

Main lobe peak migration, 58, 63, 69, 111, 116–118, 120, 121, 136, 139–141

Mutual coupling, 32

NEXRAD, 1–3

Optimization, 85, 141

Polarimetry, 3, 10, 14, 16–18, 45, 71, 75, 76, 85, 87, 88, 97, 124, 125, 128, 137  
 ATSR, 48, 49, 87, 107, 108, 137  
 STSR, 7, 13, 47, 75–77, 87, 96, 137

Progressive Pulse Compression (PPC)  
 Calibration, 16, 52, 53, 57, 58, 69  
 Leak-through elimination, 52, 53, 55–58, 64, 68  
 Partial decoding, 11, 12, 51–56, 62

Pulse compression, 6, 8, 11, 14–16, 18, 25–28, 51, 53, 55, 60, 62, 66–68, 115, 135  
 Ambiguity function, 9, 60, 62, 63, 66, 116–118  
 Cross-correlation, 9, 64, 65  
 Matched filter, 16, 18, 26, 56, 64, 65, 68, 111, 113, 119, 138, 139, 141

PX-1000, 10, 15–17, 59, 61, 66, 67, 69, 106, 107, 109, 116, 121, 124, 136, 139, 141

Radar range equation, 14, 15, 19, 39  
 Point targets, 19, 21

Volume scattering, 22, 24, 25

Radar sensitivity, 6, 8–12, 14, 15, 18,  
25–27, 51, 58–62, 70, 72, 73,  
106, 112, 114–116, 119, 136,  
139–141

Radar systems

    All-digital phased array radars, 5,  
    8, 14–17, 75, 92, 127, 137, 138

    Phased array radars, 5, 7, 12,  
    14–16, 18, 29, 31, 32, 34, 35,  
    39, 44, 88, 93, 127, 137, 140,  
    141

    Reflector antenna on a rotating  
    pedestal, 2, 7, 29, 46, 141

Radiation pattern

    Array pattern, 14, 15, 24, 29–34,  
    36–39, 76, 80, 87–90, 96–100,  
    102, 104, 106, 125, 127–131,  
    138, 142

    Array factor, 15, 32, 46, 77, 78

    Element pattern, 30, 44, 45, 79, 88,  
    92–94, 138

    Range resolution, 6, 25–27, 58, 62–64,  
    68, 69, 72, 120, 121, 136,  
    139–141

    Shoulder effect, 17, 65, 69, 109–112,  
    116–118, 120–124, 136,  
    139–141

    Sidelobe level, 17, 27, 34, 55, 65, 66,  
    69, 85, 112, 118, 136, 137

    Waveform

        Modulation, 27, 28, 51, 60–64,  
        66–69, 107, 115–117,  
        120–122, 141

    Weather radars, 1, 3, 5, 10, 14, 15, 18,  
    22, 24, 25

    WSR-88D, 1, 2, 4, 5